

Structural Analysis of an Essential Core Component of the Nuclear Pore Complex

vorgelegt von
Diplom-Ingenieurin
Vivien Nagy

von der Fakultät III – Prozesswissenschaften
der Technischen Universität Berlin
zur Erlangung des akademischen Grades

Doktorin der Ingenieurwissenschaften
- Dr.-Ing. -

Genehmigte Dissertation

Promotionsausschuss:

| | |
|---------------|--------------------------------|
| Vorsitzender: | Prof. Dipl.-Ing. Dr. Ulf Stahl |
| Gutachter: | Prof. Dr. Roland Lauster |
| Gutachter: | Prof. Dr. André Hoelz |
| Gutachter: | Prof. Dr. Leif-Alexander Garbe |

Tag der wissenschaftlichen Aussprache: 21.05.2010

Berlin, 2010

D 83

The studies for this dissertation have been carried out in the Laboratory of Cell Biology at The Rockefeller University under the supervision of Prof. Dr. Günter Blobel.

Acknowledgements

I am deeply indebted to the many people who have come across my path towards a PhD and who influenced me to grow as a scientist.

Foremost, I would like to thank my thesis advisor Dr. Günter Blobel for giving me the opportunity to perform my graduate studies in his laboratory at The Rockefeller University. I am deeply indebted to him for his scientific guidance and continuing support. My experience working with him was extremely inspiring, always stimulating and truly educational.

I would also like to thank Dr. André Hoelz for teaching me so many aspects of structural biology and X-ray crystallography in particular as well as serving as a co-advisor for this thesis. His support has been instrumental to the completion of this thesis work. He pushed me to go forward and guided me past the many obstacles I came across on the rocky way towards the structure.

I want to thank Prof. Dr. Roland Lauster for serving as my thesis advisor at the Technische Universität Berlin in Germany and his constant support throughout the years.

I would like to express my gratitude to Drs. Erik Debler, Martin Kampmann and Kuo-Chiang Hsia for being great coworkers and their contributions to the successful completion of this challenging study. Their support at all times was very much appreciated.

Special thanks go to Drs. Erik Debler and Ivo Melčák for their suggestions on and proofreading of my thesis.

I would like to thank Thomas Noriega and Andrew Davenport for their excellent technical help during the course of the last years.

All other specialists at the various synchrotrons beamlines and facilities, I would like to thank for sharing their expertise and ideas throughout this study.

Acknowledgements

I would like to thank Dr. Pete Stavropoulos for giving me the opportunity to participate in one of his many successful projects, which was not related to this thesis work.

I would also like to thank all the other past and present members of the Blobel laboratory for their support in various forms that I received during my time in the lab.

Martin and Johanna: I would like to thank you for your friendship and support in all aspects of science and life. You helped me through the difficult times of this project convincing me not to give up despite all the uncertainties and obstacles.

A special thanks goes to Ivo for being a friend.

I am thankful for the support of my family and friends who encouraged and believed in me.

I am especially grateful for the endless encouragement and support of Till, whom I couldn't have achieved this without.

Abstract

In eukaryotic cells, the nuclear envelope segregates the nucleoplasm from the cytoplasm. To allow communication between these compartments, huge proteinaceous macromolecular assemblies termed nuclear pore complexes (NPCs), are embedded into perforations of the nuclear envelope and selectively mediate nucleocytoplasmic transport. Multiple copies of approximately 30 different proteins known as nucleoporins are organized in subcomplexes and assemble the NPC with a molecular weight of around 60 MDa in yeast. While the NPC's general composition is well characterized, its molecular architecture, as well as the functional and mechanistic details of nucleocytoplasmic transport through the NPC are still enigmatic. However, several crystal structures have provided valuable insight into the NPC architecture and its dynamic nature. The structure of the Nup84 complex, an essential subcomplex of the NPC that consists of seven proteins, has been especially well characterized by X-ray crystallography in combination with electron microscopy. In an effort to advance our understanding of the architecture of the Nup84 complex and the NPC, the crystal structure of the hetero-trimeric Sec13•Nup145C•Nup84 NTD complex, the centerpiece of the heptameric Nup84 complex, was determined. Overall, the trimeric complex forms an elongated Z-shaped assembly. Nup84 NTD binding to the Sec13•Nup145C nucleoporin pair is achieved by the head-to-head interaction of two kink regions of the U-shaped α -helical solenoid domains of Nup145C and Nup84 NTD. The docking of the hetero-trimer and crystal structures of other Nup84 complex components into EM envelopes now provides a nearly complete atomic picture of the Nup84 complex. Furthermore, this structure, together with a previously determined structure of hSec13•Nup145C, suggests promiscuous binding of Nup145C. Biochemical and biophysical analyses of the Sec13•Nup145C•Nup84 NTD complex and its components suggest that these proteins are capable of engaging in different assembly states. In the future, the observed assembly states need to be placed into a functional context to resolve the dynamic four-dimensional structure of the NPC in an interdisciplinary approach.

Table of Contents

| | |
|--|-----------|
| ACKNOWLEDGEMENTS | 3 |
| ABSTRACT | 5 |
| TABLE OF CONTENTS | 6 |
| I. INTRODUCTION | 9 |
| 1. COMPARTMENTALIZATION OF THE EUKARYOTIC CELL REQUIRES TRANSPORT SYSTEMS | 9 |
| 2. THE NUCLEAR PORE COMPLEX | 11 |
| 2.1. NUCLEOCYTOPLASMIC TRANSPORT | 12 |
| 2.2. STRUCTURAL PROPERTIES OF THE NUCLEAR PORE COMPLEX | 15 |
| 2.3. COMPOSITION OF THE NUCLEAR PORE COMPLEX | 16 |
| 2.4. STRUCTURAL STUDIES OF THE NUCLEAR PORE COMPLEX BY X-RAY CRYSTALLOGRAPHY | 18 |
| 3. THE NUP84 COMPLEX | 21 |
| 3.1. COMPOSITION AND FUNCTION OF THE NUP84 COMPLEX | 21 |
| 3.2. THE NUP84 COMPLEX – A MEMBRANE-COATING COMPLEX | 22 |
| 3.3. STRUCTURE OF THE NUP84 COMPLEX | 23 |
| 3.4. A MODEL FOR THE MEMBRANE-COATING CYLINDER OF THE NUCLEAR PORE COMPLEX | 26 |
| 3.5. FURTHER MODELS FOR THE ARRANGEMENT OF NUP84 COMPLEXES IN THE NPC | 32 |
| 4. AIM OF THIS THESIS | 36 |
| II. RESULTS | 37 |
| 1. DOMAIN STRUCTURES OF SEC13, NUP145C, AND NUP84 | 37 |
| 2. PROTEIN PURIFICATION | 42 |
| 2.1. PURIFICATION OF NUP84 NTD | 42 |
| 2.2. PROTEIN PURIFICATION OF THE SEC13•NUP145C COMPLEX | 46 |
| 2.3. FORMATION AND PURIFICATION OF THE SEC13•NUP145C•NUP84 NTD COMPLEX | 48 |
| 3. CRYSTALLIZATION | 51 |
| 3.1. CRYSTALLIZATION OF NUP84 NTD | 51 |

Table of Content

| | | |
|-------------|--|-----------|
| 3.2. | CRYSTALLIZATION OF THE SEC13•NUP145C•NUP84 NTD COMPLEX | 52 |
| 4. | STRUCTURE DETERMINATION | 56 |
| 4.1. | DATA COLLECTION AND PROCESSING | 56 |
| 4.2. | MOLECULAR REPLACEMENT | 57 |
| 4.3. | PHASING WITH MIRAS | 58 |
| 4.4. | MODEL BUILDING AND REFINEMENT | 62 |
| 5. | CRYSTAL STRUCTURE OF THE SEC13•NUP145C•NUP84 NTD COMPLEX | 64 |
| 5.1. | ARCHITECTURAL OVERVIEW | 64 |
| 5.2. | THE NUP84 NTD α -HELICAL DOMAIN | 65 |
| 5.3. | SURFACE PROPERTIES OF THE NUP84 NTD | 66 |
| 5.4. | THE NUP145C•NUP84 NTD INTERFACE | 68 |
| 6. | DOCKING OF THE CRYSTAL STRUCTURE INTO A THREE-DIMENSIONAL ELECTRON MICROSCOPY RECONSTRUCTION OF THE NUP84 COMPLEX | 70 |
| 7. | STRUCTURAL COMPARISON OF THE SEC13•NUP145C•NUP84 NTD COMPLEX TO THE HSEC13•NUP145C COMPLEX | 73 |
| 7.1. | HETERO- AND HOMO-DIMERIZATION OF NUP145C | 74 |
| 7.2. | CONFORMATIONAL CHANGES | 76 |
| 8. | BIOCHEMICAL CHARACTERIZATION OF THE SEC13•NUP145C•NUP84 NTD COMPLEX | 78 |
| III. | DISCUSSION | 81 |
| 1. | STRUCTURE DETERMINATION OF THE SEC13•NUP145C•NUP84 NTD COMPLEX | 81 |
| 2. | STRUCTURAL ANALYSIS OF THE SEC13•NUP145C•NUP84 NTD COMPLEX | 82 |
| 3. | DOCKING OF CRYSTAL STRUCTURES INTO LOW-RESOLUTION EM-RECONSTRUCTIONS – A PARADIGM FOR THE STRUCTURAL INVESTIGATION OF THE NPC | 84 |
| 4. | FLEXIBILITY OF NUCLEOPORINS, NUCLEOPORIN SUBCOMPLEXES, AND THE NPC | 87 |
| 5. | THE SEC13•NUP145C•NUP84 COMPLEX IN THE CONTEXT OF THE VARIOUS NPC MODELS | 90 |
| 6. | IMPLICATIONS FOR PROMISCUOUS BINDING OF NUP145C | 93 |
| 7. | HOMOTYPIC INTERACTIONS | 95 |

| | |
|---|------------|
| <u>IV. CONCLUSION AND FURTHER DIRECTIONS</u> | 97 |
| <u>V. MATERIAL AND METHODS</u> | 99 |
| 1. PROTEIN SEQUENCE ANALYSES | 99 |
| 2. MOLECULAR CLONING | 99 |
| 3. PROTEIN EXPRESSION | 100 |
| 4. PROTEIN PURIFICATION | 100 |
| 5. BIOCHEMICAL ANALYSES OF THE SEC13•NUP145C•NUP84 NTD COMPLEX | 104 |
| 5.1. ANALYTICAL SIZE EXCLUSION CHROMATOGRAPHY | 104 |
| 5.2. ISOTHERMAL TITRATION CALORIMETRY | 104 |
| 5.3. ANALYTICAL ULTRACENTRIFUGATION | 104 |
| 5.4. MULTI-ANGLE LIGHT SCATTERING | 105 |
| 6. PROTEIN CRYSTALLIZATION | 105 |
| 7. STRUCTURE DETERMINATION AND REFINEMENT | 106 |
| 8. DOCKING OF CRYSTAL STRUCTURES INTO THE EM STRUCTURE | 107 |
| <u>ZUSAMMENFASSUNG</u> | 108 |
| <u>LIST OF ABBREVIATIONS</u> | 109 |
| <u>LIST OF FIGURES</u> | 112 |
| <u>LIST OF TABLES</u> | 114 |
| <u>BIBLIOGRAPHY</u> | 115 |

I. Introduction

1. Compartmentalization of the Eukaryotic Cell Requires Transport Systems

The cell is the basic functional and structural unit of all life. In every cell, the instructions for the maintenance and reproduction of life are contained in the genetic information, which is encoded by DNA molecules. Apart from this basic mutuality, cells can be classified into two kinds – prokaryotic and eukaryotic cells. Prokaryotes are single cell organisms whose genetic information is not contained within a specific subcellular organelle, instead it is located in the cytoplasm, the only compartment of the prokaryotic cell. The simple prokaryotic cells are considered evolutionary precursors of the more complex eukaryotic cells that build up all multicellular organisms, but that also exist as single-cell organisms. The evolution of the eukaryotic cell has entailed the formation of intricate intracellular membrane systems that enable the cell to concurrently carry out a diverse set of processes in various chemical milieus. It was hypothesized that intracellular membrane systems may have evolved from either the invagination of the plasma membrane (Blobel, 1980) or from the engulfment of one cell by another cell (Sagan, 1967).

As a result of this compartmentalization, sophisticated transport systems have co-evolved which mediate and regulate macromolecular transport between different subcellular locations. In transmembrane transport, membrane-embedded protein translocators directly transport proteins and other molecules from the cytosol across an intracellular membrane. In vesicular transport, cargo is ferried between membrane-bound organelles via membrane-enclosed intermediates, such as spherical vesicles, which are stabilized by protein coats that are reminiscent of cages. A third major transport system refers to the selective macromolecular transport across the double membrane of the nuclear envelope.

Among the several eukaryotic cell compartments, the nucleus harbors the majority of the genetic information that is encoded in the DNA and keeps it protected. The nucleus is surrounded by the nuclear envelope. Formed by two closely juxtaposed membranes, termed the inner nuclear membrane (INM) and the outer nuclear membrane (ONM), the nuclear envelope serves as a boundary between the nucleus and the cytoplasm. The development of the nucleus resulted in the spatial separation of two cellular processes essential for all life – transcription of the genetic information into mRNA within the nucleus and translation of mRNA into proteins in the cytoplasm. This physical separation of these two cellular processes permits a high degree of control and regulation for gene expression and is a basis for cellular differentiation in multicellular organisms. A prerequisite for the regulated flow of genetic information from DNA via RNA to protein at various stages of the cell's life is a selective transport system that connects the nucleoplasm and the cytoplasm. Nuclear pore complexes exclusively mediate the selective macromolecular transport in and out of the nucleus.

2. The Nuclear Pore Complex

In 1954 at The Rockefeller University, Michael L. Watson discovered circular pores in the nuclear envelope by electron microscopy of thin cell sections (Watson, 1954). A proteinaceous macromolecular complex is embedded into these circular openings – the nuclear pore complex (NPC). With a molecular weight of around 60 MDa in yeast and even around 120 MDa in higher eukaryotes, the NPC is one of the largest macromolecular assemblies of the eukaryotic cell. There are approximately 200 NPCs in yeast nuclei and generally around 2000 NPCs in higher eukaryotic cells, although some cell's nuclei contain

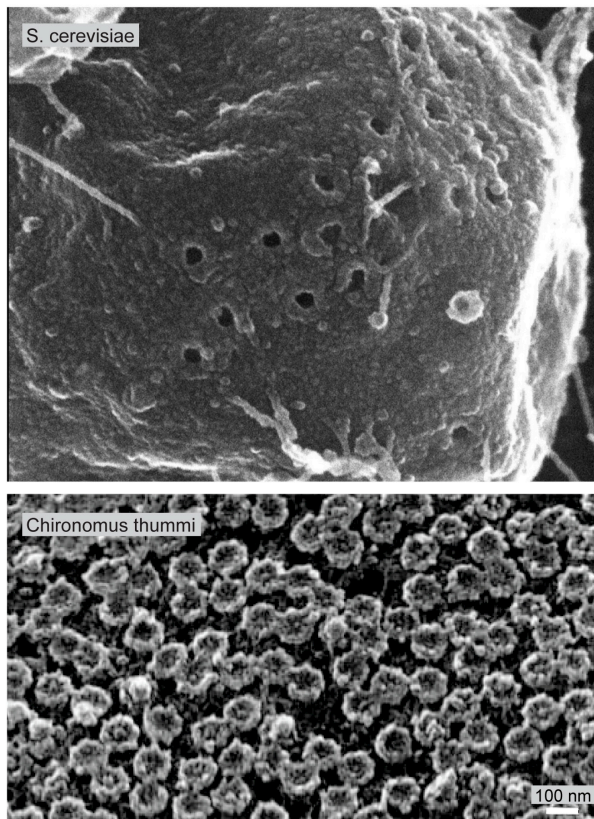


Figure 1: Nuclei with Nuclear Pore Complexes

Scanning electron microscopy images of a *S. cerevisiae* nucleus in the top panel (Murray and Kiseleva, 2008) and a *Chironomus thummi* nucleus in the bottom panel (Kiseleva et al., 1998).

even up to several millions NPCs (Figure 1) (Kiseleva et al., 1998). The overall structure and function of the NPC, however are well conserved in all eukaryotes.

Although the NPC has been described to be involved in important cellular functions, such as chromatin organization, regulation of transcription, and DNA repair (Blobel, 1985; Galy et al., 2000; Khadaroo et al., 2009; Nagai et al., 2008; Towbin et al., 2009), its major function is the nucleocytoplasmic transport.

2.1. Nucleocytoplasmic Transport

Diffusion experiments with labeled dextrans and gold particles revealed that particles up to 5 nm in diameter can passively diffuse through the NPC. For molecules larger than 40 kDa the NPC serves as a diffusion barrier and “gatekeeper” (Figure 2A) (Feldherr, 1962; Paine et al., 1975; Peters, 1984).

The active import and export of larger macromolecules is facilitated by signal sequences within the cargo protein sequence. Nuclear localization sequences (NLS) target proteins for nuclear import whereas nuclear export sequences (NES) govern nuclear export. The signal sequences are recognized by soluble transport factors, which have been collectively termed karyopherins. In the classic case, the NLS is recognized by an adapter karyopherin- α (kap- α), which in turn is recognized by karyopherin- β (kap- β). Upon binding of their cargo, karyopherins interact with NPC components to facilitate the transport through the NPC (Figure 2B). The small GTPase Ran controls the directionality of transport. The guanine nucleotide exchange factor of Ran, Ran-GEF, is localized in the nucleus, while the GTPase-activating protein RanGAP is localized in the cytoplasm. Therefore a gradient of the Ran•GTP/Ran•GDP ratio is maintained with high levels of Ran•GTP in the nucleus and high levels of Ran•GDP in the cytoplasm. Ran•GTP compared to Ran•GDP has a much higher affinity for import karyopherins (Floer and Blobel, 1996) and, hence, destabilizes the import complexes by association with the kap- β (Moroianu et al., 1996). As a consequence, the cargo molecule is released and enriched in the nucleus. At the

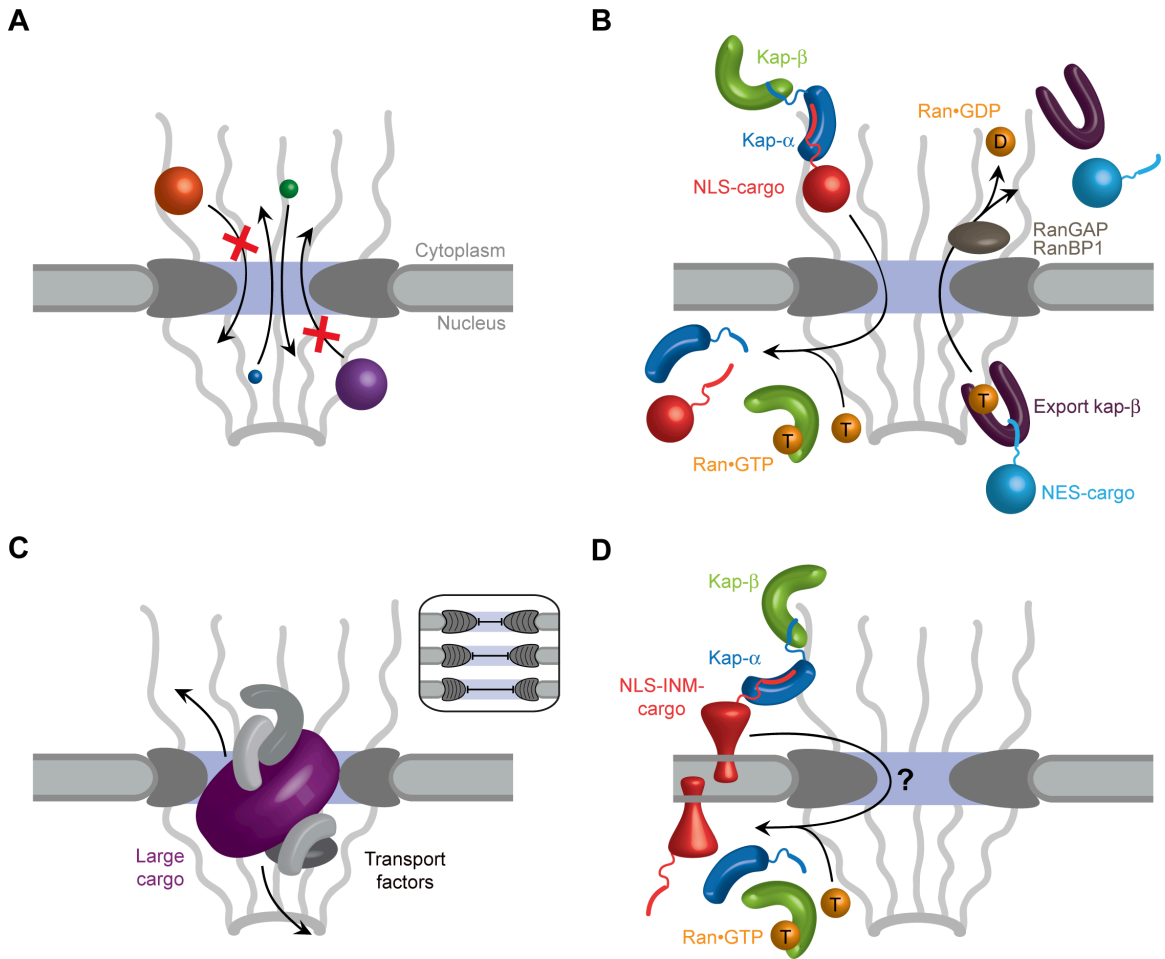


Figure 2: Transport functions of the NPC

A) Molecules smaller than ~40 kDa freely diffuse through the NPC. B) Active import and export of cargoes are facilitated by nuclear localization and nuclear export sequences (NLS and NES, respectively) that are recognized by transport factors, termed karyopherins (kaps). The NLS of import cargoes is recognized either directly by an import karyopherin- β (kap- β) or via an adapter karyopherin (kap- α). Ran•GTP binding inside the nucleus dissociates the import complex (left). By contrast, the assembly of an NES-cargo kap- β export complex requires Ran•GTP binding. In the cytosol, the export complex is dissociated by GTP hydrolysis stimulated by the Ran GTPase-activating protein (RanGAP) or Ran binding protein 1 (RanBP1). C) The transport of large cargoes requires the dilation of the central channel of the NPC (inset). D) Inner nuclear membrane (INM) proteins are co-translationally integrated into the endoplasmic reticulum membrane, which is continuous with the ONM, and then imported to the INM. Similar to panel B, the transport of INM proteins is also dependent on the Ran-cycle and karyopherins that likely travel through the central channel, while the cargo protein is anchored in the membrane and somehow pulled through. Substantial structural changes within the NPC would be necessary to facilitate this transport event.

same time, Ran•GTP also stabilizes the formation of the export complexes composed of Ran•GTP, an export karyopherin- β , and a cargo molecule in the nucleus. Upon export this complex is dissociated by GTP hydrolysis stimulated by RanGAP on the cytoplasmic face of the nucleus (Figure 2B). The Ran cycle is closed by the transport of the resulting Ran•GDP back into the nucleus by the nuclear transport factor NTF2 (Nehrbass and Blobel, 1996; Ribbeck et al., 1998) where RanGEF catalyzes the nucleotide exchange generating Ran•GTP (Chook and Blobel, 2001; Cook et al., 2007).

The NPC does not only facilitate the transport of single molecules but also that of large macromolecular assemblies. The 40S and 60S ribosomal subunits are assembled in the nucleus and exported into the cytoplasm where they unite to functional ribosomes. Together with large messenger ribonucleoprotein particles (mRNP), they are by far the largest macromolecular cargos that are translocated through the NPC. To allow the passage of these large assemblies, the central channel of the NPC may have to dilate substantially (Figure 2C) (Akey, 1990; Kiseleva et al., 1998; Pante and Kann, 2002).

While nucleocytoplasmic transport of soluble macromolecules was already well understood, the question of how INM proteins cross the nuclear envelope and reach their final destination was under debate for a long time. The INM contains a unique set of integral membrane proteins that bind to chromatin and the nuclear lamina inside the nucleus (Burke and Stewart, 2006; Vlcek and Foisner, 2007). Inside the lumen of the nuclear envelope, the INM proteins establish connections with the cytoskeleton via interactions with ONM proteins. After co-translational insertion into the ER membrane, INM proteins are specifically targeted to the nuclear side of the nuclear envelope. Recently, experiments in karyopherin deficient cells and in cells with a disrupted Ran-cycle showed that the import of these membrane proteins is – similar to the import of soluble proteins – dependent on karyopherins and the Ran-cycle (King et al., 2006). However, the proteins are likely to remain anchored in the membrane during this transport process, while the attached karyopherin travel through the central

channel of the NPC (Figure 2D). Hence, substantial structural rearrangements of the NPC's scaffold would be required to facilitate the import of INM proteins.

2.2. Structural Properties of the Nuclear Pore Complex

Entire membrane-embedded and detergent-extracted NPCs of many organisms have been studied by electron microscopy. These studies revealed the overall dimensions and symmetric properties of the NPC (Beck et al., 2004; Gall, 1967; Hinshaw et al., 1992; Kiseleva et al., 2004; Yang et al., 1998).

The total molecular mass was estimated to be around 60 MDa in yeast and up to 120 MDa in higher eukaryotes. In general, the NPC shows an eight-fold rotational symmetry around the nucleo-cytoplasmic axis. In some cases a nine- or ten-fold rotational symmetry has been observed (Hinshaw and Milligan, 2003). The central core of the NPC shows a two-fold rotational symmetry around the mid-plane of the nuclear envelope. Furthermore, it has been observed that the symmetric core of the NPC is asymmetrically decorated with eight filaments on the cytoplasmic side and eight filaments that protrude from the nuclear side, where the ends form a distal ring (Jarnik and Aebi, 1991). These structures are termed cytoplasmic filaments and nuclear basket.

In yeast cells, the symmetric core of the NPC is around 100 nm wide and 30 nm high. In other eukaryotes, the NPC has larger dimensions with a diameter and a height of up to 150 nm and 80 nm, respectively (Yang et al., 1998). Similarly, the nuclear basket structure in yeast appears to be smaller compared to *Xenopus* nuclei (Fahrenkrog et al., 1998). The NPC's central channel was observed to have dimensions of up to 40 nm, but appears to be only transiently dilated to this diameter during transport. (Akey, 1990; Kiseleva et al., 1998; Pante and Kann, 2002; Yang et al., 1998). Further structural flexibility of the NPC has been observed in many studies and has been suggested to play a crucial role for the functionality of the NPC (Akey, 1995; Akey and Radermacher, 1993; Beck et al., 2007).

2.3. Composition of the Nuclear Pore Complex

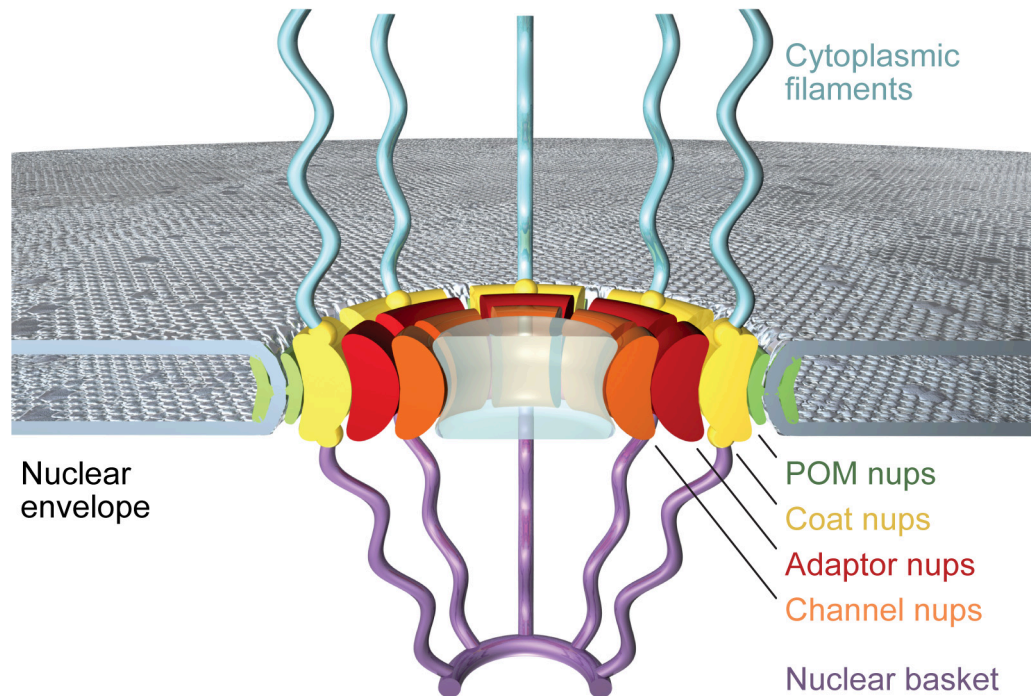
Initially, it was assumed that more than 100 different proteins are necessary to compose one NPC. Surprisingly, only around 30 different proteins were found in subcellular fractions highly enriched in NPCs (Rout et al., 2000). These proteins are termed nucleoporins or nups. Due to the high degree of internal symmetry of the NPC, each nucleoporin occurs in multiple copies, and, thus, the fully assembled NPC contains hundreds of proteins. In yeast, immuno-gold labeling of genetically tagged nucleoporins has revealed their approximate location in the NPC (Rout et al., 2000). Most of the nucleoporins can be assigned to the symmetric core of the NPC and are symmetrically located at the nucleoplasmic and cytoplasmic side of the NPC. The nucleoporins Nup82, Nup159, Nup116, Nup100, Nup145N, and Nup42 are located predominantly on the cytoplasmic face of the NPC (Hurwitz et al., 1998; Kraemer et al., 1995; Rout et al., 2000). Nup1, Nup2, and Nup60 are likely to form the nuclear basket structure due to their localization on the nucleoplasmic side (Rout et al., 2000).

A model for the NPC was proposed that categorizes the nucleoporins of the symmetric core into 4 concentric cylinders around the central channel. However, the cylinders are envisioned to have porous walls and would allow for interdigitation and invasion of nucleoporins of neighboring cylinders (Figure 3) (Hsia et al., 2007). In the following, the four cylinders are described:

- 1) Three nucleoporins are integral membrane proteins specifically located to the pore membrane domain (POM), the region of the nuclear envelope where the outer and the inner nuclear membrane fuse. Integrated into this specific membrane domain are the proteins Ndc1, POM34, and POM152, which presumably anchor the soluble nucleoporins to the nuclear envelope (Chial et al., 1998; Rout et al., 2000; Wozniak et al., 1994).

- 2) Nup120, Seh1, Nup85, Sec13, Nup145C, Nup84, and Nup133 are located in close proximity to the pore membrane domain. These proteins form the heptameric Nup84 subcomplex that may serve as a membrane coating module

to stabilize the sharp membrane curvature of the pore membrane domain (Devos et al., 2004; Rout et al., 2000).



| POM nups | Coat Nups | Adaptor Nups | Channel Nups | Filaments | Basket |
|----------|-----------|--------------|--------------|-----------|--------|
| Pom152 | Seh1 | Nic96 | Nsp1 | Nup82 | Nup60 |
| Pom34 | Nup85 | Nup192 | Nup49 | Nup159 | Nup2 |
| Ndc1 | Nup120 | Nup188 | Nup57 | Nup116 | Nup1 |
| | Sec13 | Nup157 | | Nup100 | |
| | Nup145C | Nup170 | | Nup145N | |
| | Nup84 | Nup53 | | Nup42 | |
| | Nup133 | Nup59 | | | |

Figure 3: Schematic model and composition of the yeast NPC

The NPC is embedded into the nuclear envelope. Cytoplasmic filaments and the nuclear basket structure are asymmetrically attached on the cytoplasmic and the nucleoplasmic sides of the NPC. The symmetric core can be envisioned to include four concentric cylinders composed of integral pore membrane proteins (POMs), coat nups, adapter nups, and channel nups. Natively unfolded FG-repeats of a number of nups make up the transport barrier in the central channel and are indicated by a transparent plug.

3) A third group of proteins (Nup53, Nup59, Nic96, Nup157, Nup170, Nup188, and Nup192) are thought to be sandwiched between the membrane-coating

proteins and the innermost channel nups and, therefore, may cushion dynamic changes of the pore diameter.

4) The innermost channel nups Nsp1, Nup49, and Nup57 contain phenylalanine-glycine motifs, so-called FG-repeats. FG-repeat domains are predicted to be natively unstructured regions that contain no secondary structure elements. They extend into the central, cargo translocation channel of the NPC where they contribute to the diffusion barrier for large macromolecules and serve as docking sites for the soluble transport factors. Hence, FG-repeats provide the basis for selective transport through the NPC. However, it is not well understood how the interaction of karyopherins to FG-repeats leads to the translocation through the NPC and, therefore, their mechanism of action is heavily debated. The FG repeat domains could be highly mobile and dynamic, forming a “polymer brush” that occludes the central channel, thereby preventing large molecules to diffuse through the “virtual gate” of the NPC (Rout et al., 2003; Rout et al., 2000). Another attempt to explain the molecular mechanism for the selective transport barrier provides the “selective phase” model (Frey and Gorlich, 2007; Ribbeck and Gorlich, 2002). Here, the FG-repeats would interact with each other and form a hydrophobic meshwork, a “hydrogel”. The competing binding of karyopherins to the FG-repeats would allow the transport through the central channel. With the “dual gate” model, Rexach and coworkers propose a combination of both models, in which selectivity is achieved by an entropic barrier in the periphery and a central hydrophobic barrier (Patel et al., 2007).

2.4. Structural Studies of the Nuclear Pore Complex by X-ray Crystallography

Electron microscopy studies together with biochemical and genetic approaches to study the NPC have given valuable insight into the structural and functional properties of the NPC. In addition, a crude topology map could be derived from these data. The details of the exact location and stoichiometry of all nucleoporins, the interactions between them, as well as the mechanisms for the functions and dynamics of the NPC, remain to be deciphered. However, the large

interfaces between nucleoporins, the observed functional redundancy, and the robust architecture of the NPC make it very difficult to decipher the molecular principles that underlie the NPC's function by genetic or biochemical methods. The structure of the NPC at atomic resolution would substantially contribute to the understanding of the molecular mechanisms that enable the NPC to facilitate nucleocytoplasmic transport and would provide a detailed roadmap for further biochemical and *in vivo* studies.

The high complexity combined with the large dimensions of the NPC makes the determination of its entire structure at high resolution by X-ray crystallography an ambitious goal. In comparison, the largest macromolecular crystal structure determined to date is the 70S Ribosome, which is about 30 times smaller and a relatively rigid assembly. In contrast, the NPC is a highly flexible and dynamic assembly and many nucleoporins have natively unfolded regions – two key facts that substantially complicate the structure determination with current X-ray crystallography technology. The flexible nature of the NPC, which represents a major crystallization obstacle, prevents the determination of the NPC in a single structure at this point. Furthermore, it is not practicable to isolate large amounts of homogeneous NPCs from cells due to the small copy number per cell as well as the contamination with a large amount of NPC-associated transport factors in complex with cargo molecules as well as other unspecifically bound proteins. Moreover, the NPC has not been assembled *in vitro* from purified components yet, which would allow crystallization attempts of a homogeneous assembly. Therefore, to tackle the atomic structure of the NPC, an interdisciplinary “piece-by-piece” strategy must be employed. According to this approach, high-resolution crystal structures of individual nucleoporins and of nucleoporin complexes would be obtained. These structures will then be fitted into the envelopes of three-dimensional EM reconstructions of larger nucleoporin assemblies and ultimately, into the EM structure of the entire NPC.

Over the last five years, the structural characterization of nucleoporins has dramatically expanded. Today, many high-resolution crystal structures of individual nucleoporins and hetero-dimeric nucleoporin complexes have been

determined. These structures have given tremendous insight in the molecular architecture of the NPC (Berke et al., 2004; Boehmer et al., 2008; Brohawn et al., 2008; Debler et al., 2008; Handa et al., 2006; Hodel et al., 2002; Hsia et al., 2007; Jeudy and Schwartz, 2007; Leksa et al., 2009; Melčák et al., 2007; Napetschnig et al., 2007; Napetschnig et al., 2009; Partridge and Schwartz, 2009; Reverter and Lima, 2005; Schrader et al., 2008a; Schrader et al., 2008b; Seo et al., 2009; Sun and Guo, 2008; Vetter et al., 1999; von Moeller et al., 2009; Weirich et al., 2004; Whittle and Schwartz, 2009). Furthermore, some of these structures revealed the molecular basis of key steps in the mRNA export pathway (Napetschnig et al., 2009; Schrader et al., 2008a; Schrader et al., 2008b) and the potential underlying principles that govern the dilation of the central channel (Melčák et al., 2007).

The ultimate aim is to put these crystal structures in the context of the NPC by fitting them into EM structures of the entire NPC. The highest-resolution EM structure of the NPC was determined at 60 Å (Beck et al., 2007). However, EM structures of this resolution do not allow for the docking of crystal structures unambiguously. In general, EM structures at resolutions of ~15 Å or better are required to fit crystal structures with high confidence. To overcome this problem, EM studies of smaller building blocks of the NPC that result in higher resolutions are very valuable.

Another fundamental problem at this point is the unknown exact stoichiometry of nucleoporins in the NPC. The stoichiometry has been roughly determined with pull-down experiments of genetically tagged proteins from yeast cells followed by semi-quantitative western blotting analysis. This approach yielded copy numbers of the nucleoporins with relatively high standard deviations (Rout et al., 2000). It is obvious, that it is extremely important to know the exact stoichiometry in order to be able to place the correct number of each crystal structure into a structure of the entire NPC of lower resolution.

3. The Nup84 Complex

At the beginning of mitosis in higher eukaryotic cells, dramatic structural changes of the nuclear envelope architecture occur that ultimately entail the complete disintegration of the nuclear envelope, a phenomenon called nuclear envelope breakdown (NEBD). Concurrently the NPC disassembles into distinct single nucleoporins and subcomplexes from which the NPC reassembles at the end of open mitosis (Bodoor et al., 1999; Vasu and Forbes, 2001). By contrast, yeast cells do not undergo open mitosis. However, the NPCs can be dissected biochemically into similar subcomplexes found in mitotic cell extracts of higher eukaryotic cells. So far, the best characterized NPC subcomplex in yeast cells is the Nup84 complex.

3.1. Composition and Function of the Nup84 Complex

The Nup84 complex is a heptameric protein complex composed of Nup120, Nup85, Seh1, Nup145C, Sec13, Nup84, and Nup133. Nup84 was initially identified in a genetic screen. A pull-down experiment with tagged Nup84 identified that Nup84 forms a hexameric complex with Nup120, Nup85, Sec13, Seh1, and an unknown protein. (Siniossoglou et al., 1996). Subsequently, the unknown protein was discovered to be Nup145C, the C-terminal part of Nup145 (Teixeira et al., 1997). Interestingly, by autoproteolysis of Nup145, two subunits of the NPC with different functions and locations are generated, Nup145N and Nup145C. Subsequently, Nup133 was then identified as a seventh member of the complex isolated under modified conditions (Allen et al., 2001; Lutzmann et al., 2002; Siniossoglou et al., 2000).

Mutations, deletions, or depletions of single Nup84 complex members have severe defects in mRNA export, the distribution of NPCs in the nuclear envelope, and the recruitment of other nucleoporins during NPC formation (Boehmer et al., 2003; Siniossoglou et al., 2000; Siniossoglou et al., 1996; Teixeira et al., 1997). Whereas mutations of most nucleoporins have either transport defects or

structural defects, mutations of the Nup84 complex members show both defects. Furthermore, composed by seven out of 30 nucleoporins and a molecular mass of around 600 kDa per single Nup84 complex, the functional and structural important Nup84 complex represents an essential core component of the NPC.

The Nup84 complex has an evolutionarily conserved equivalent in higher eukaryotes, the Nup107-Nup160 complex. The vertebrate nonameric complex is composed of Nup133, Nup85, Sec13, Seh1, Nup107 (yNup84), Nup96 (Nup145C), Nup160 (yNup120) (Belgareh et al., 2001) and two additional proteins, Nup37 and Nup43, which were subsequently identified (Loiodice et al., 2004). The complex is biochemically stable and can be isolated from mitotic cells. Functionally, the Nup107-Nup160 complex is important for NPC biogenesis, nucleocytoplasmic transport, and cell division (Belgareh et al., 2001; Harel et al., 2003; Vasu et al., 2001).

3.2. The Nup84 Complex – A Membrane-Coating Complex

Several similarities have been observed between the Nup84 complex and the membrane-coating COPI, COPII, and clathrin complexes, which play critical roles in cargo trafficking between different compartments of the endocytic and secretory pathways (Kirchhausen, 2000). These complexes share the same fold composition with two principle folds, α -solenoids and β -propellers. Furthermore, the arrangement of an N-terminal β -propeller followed by an α -solenoid seems unique to the protein complexes named above (Devos et al., 2004). Strikingly, Sec13, which has originally been discovered as a secretion factor and later found to be a component of the COPII complex (Kaiser and Schekman, 1990; Salama et al., 1993), is also a component of the Nup84 complex (Siniosoglou et al., 1996). Based on these similarities, it was hypothesized that the membrane-coating complexes and the Nup84 complex have evolved from a common precursor, the protocoatomer (Devos et al., 2004). In accordance with the hypothesis that intracellular membrane systems have evolved from invaginated plasma membranes (Blobel, 1980), this protocoatomer was proposed to stabilize

the generated sharp membrane curvatures. During evolution the protocoatmer diverged into today's membrane-coating complexes. As a consequence, the Nup84 complex was proposed to serve as a membrane-coating complex in the NPC. Coherently, the Nup84 complex was localized in the NPC close to the nuclear pore membrane (Rout et al., 2000). Furthermore, Nup133 contains a predicted membrane curvature-sensing motif that has been shown to interact with small liposomes (Drin et al., 2007).

3.3. Structure of the Nup84 complex

The Nup84 complex can be biochemically reconstituted from its recombinantly expressed and purified components. Both the reconstituted and the isolated Nup84 complexes have been structurally characterized by two-dimensional negative-stain electron microscopy, which revealed an overall Y-shaped structure

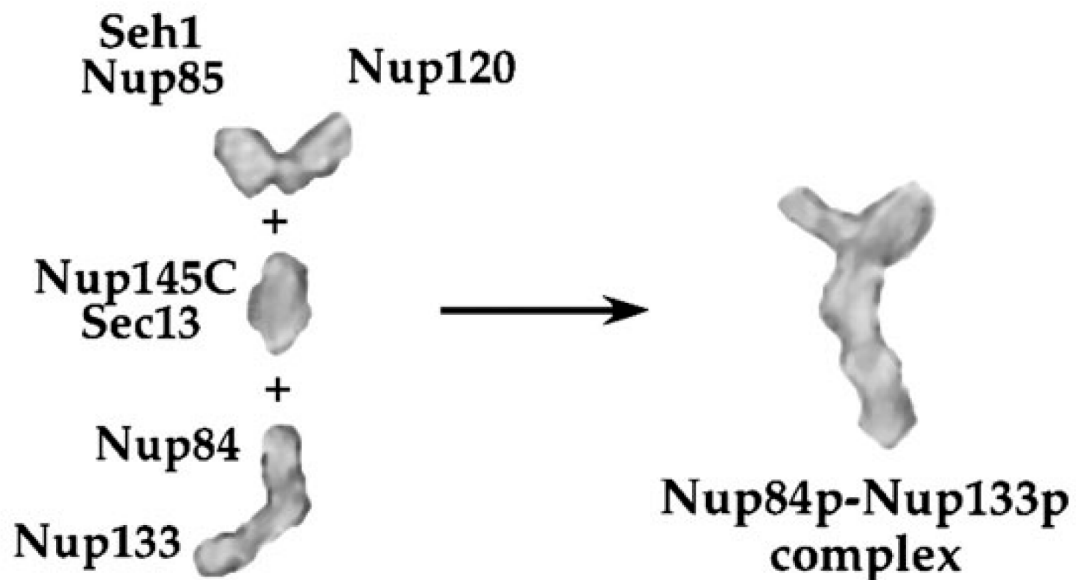


Figure 4: A structural model for the Nup84 complex

The subunits of the Nup84 complex were analyzed by single particle EM before and after *in vitro* reconstitution. A structural model was derived from this puzzle-like approach (Lutzmann et al., 2002).

(Lutzmann et al., 2002; Siniossoglou et al., 2000). In addition, the shape of smaller modules of the Nup84 complex was determined and based on a puzzle-like approach combined with biochemical interaction studies, their approximate location within the Y-shaped complex was proposed. Nup120, Nup85, and Seh1 form the two upper arms of the Y-shape, Nup145C and Sec13 form the centerpiece where Nup84 followed by Nup133 is attached at the base of the 400

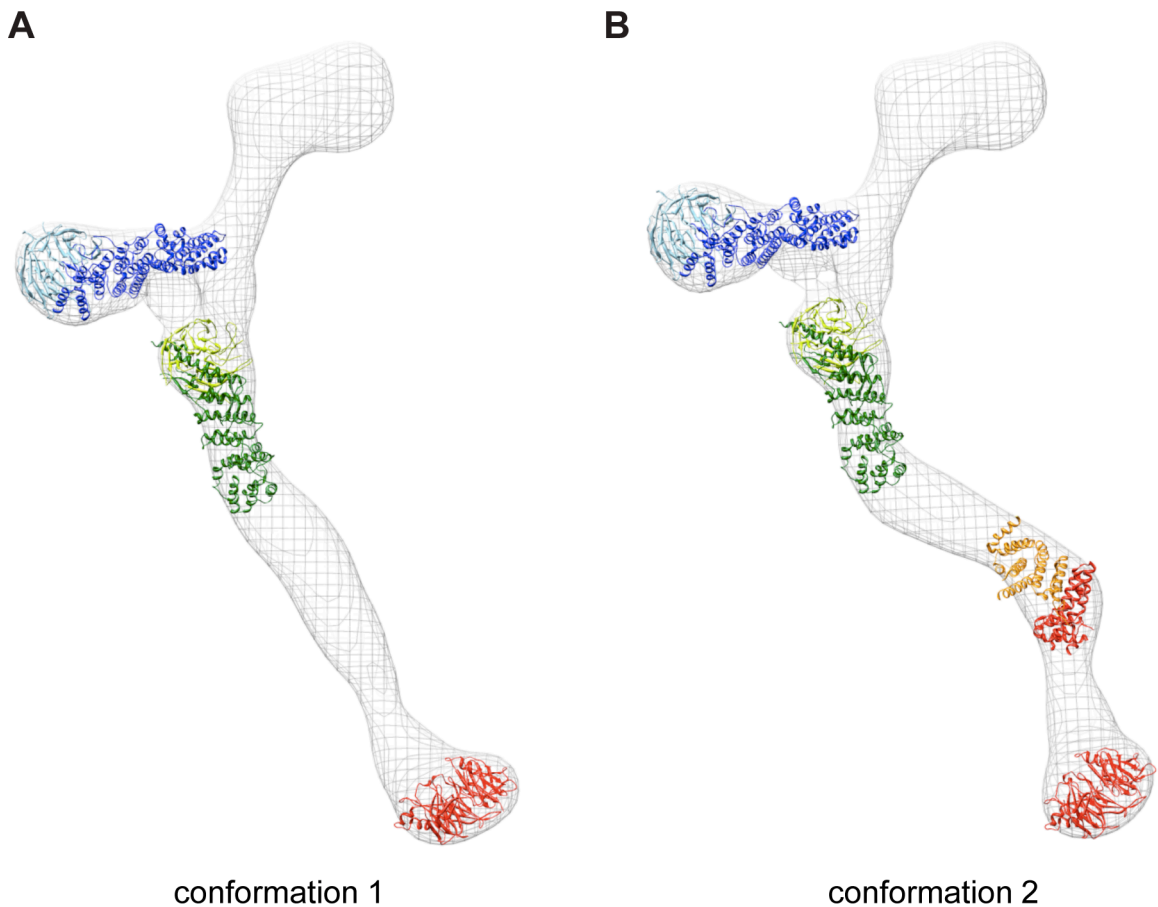


Figure 5: Three-dimensional EM-reconstruction of the Nup84 complex

The three-dimensional structure was determined by single-particle EM of negatively stained samples followed by random conical-tilt reconstruction. The yeast Seh1•Nup85 crystal structure (light blue and dark blue, respectively), the chimeric structure of hSec13•Nup145C (light green and dark green, respectively), and the human Nup133 NTD (red) were fitted into both observed conformations of the Nup84 complex. The structure of the human Nup107 CTD•Nup133 CTD (orange and red, respectively) fitted only the hinged conformation of the Nup84 complex. Note that Nup107 is the human equivalent of Nup84 (Kampmann and Blobel, 2009).

Å-long structure (Figure 4) (Lutzmann et al., 2002).

To gain further knowledge about the architecture of the Nup84 complex, it has become a target for X-ray crystallography. Several high-resolution crystal structures of Nup84 complex subunits have been determined by this technique to date: the human Nup133 N-terminal domain (NTD) (Berke et al., 2004), the human Nup107 CTD•Nup133 CTD nucleoporin complex (Nup107 is the human homolog of Nup84) (Boehmer et al., 2008), the hSec13•Nup145C complex (Hsia et al., 2007), the yeast Seh1•Nup85 complex (Brohawn et al., 2008; Debler et al., 2008), and the yeast Nup120 NTD (Leksa et al., 2009; Seo et al., 2009).

In addition to these crystallographic studies, a three-dimensional EM reconstruction of the entire heptameric building block was obtained to a resolution of around 35 Å by three-dimensional negative-stain EM reconstruction (Kampmann and Blobel, 2009). Interestingly, the Nup84 complex was observed in two distinct conformations that show flexibility in two specific hinge regions in the long stem of the heptameric complex. The crystal structures that were available at that time were used for fitting into the EM structure. The crystal structures of hNup133 NTD, hSec13•Nup145C, and Seh1•Nup85, could be approximately docked into the EM structure of both conformations. The kinked human Nup107 CTD•Nup133 CTD structure could only be fitted into one of the conformations following one of the hinge regions (Figure 5). Despite the relatively low resolution of only 35 Å, docking of the crystal structures was possible, because the localization within the Nup84 complex was determined by the previous two-dimensional EM and biochemical characterization (Lutzmann et al., 2002), as well as genetic GFP-tagging of the Nup133 and Seh1 components (Kampmann and Blobel, 2009). Thus, the structural characterization of the Nup84 complex constitutes a paradigm for the piece-by-piece approach to ultimately determine the structure of the entire NPC architecture.

3.4. A Model for the Membrane-Coating Cylinder of the Nuclear Pore Complex

Two crystal structures of Nup84 complex components have been especially educational, because they gave a first idea of how the Nup84 complex could form higher-order structures in the NPC. One of these two crystal structures refers to the dimeric nucleoporin complex of yeast Nup145C in complex with human Sec13 (hSec13) (Hsia et al., 2007). The structure of this chimeric hSec13•Nup145C hetero-dimer revealed a 285 Å-long, slightly bent rod composed of a hetero-octamer. Further, the structure shows how Sec13 folds into a 6-bladed β -propeller and Nup145C into a U-shaped α -solenoid. Interestingly, the 6-bladed β -propeller is completed to a 7-bladed propeller by a domain invasion motif (DIM) provided by the N-terminal domain of Nup145C. A hetero-tetramer is formed by the homo-dimerization of Nup145C, in which the kinked regions of two U-shaped α -helical solenoids interact with each other. Two hetero-tetramers ultimately form the hetero-octamer observed in the crystal structure by homo-dimerization of two hSec13 β -propellers (Figure 6). The oligomerization behavior in solution was analyzed with the result that the hSec13•Nup145C as well as the yeast Sec13•Nup145C complex exists in a concentration-dependent equilibrium between a hetero-dimer and a hetero-tetramer with additional minor amounts of a hetero-octamer as observed in the crystal structure of hSec13•Nup145C (Hsia et al., 2007). Small amounts of a hetero-dodecamer were detected for the hSec13•Nup145C but not for the yeast Sec13•Nup145C complex (Hsia et al., 2007). Furthermore, the hetero-octamer formation was observed under two different crystal packings. Therefore, the oligomerization of the Sec13•Nup145C hetero-dimer is not limited to packing within the crystal and could be relevant for the formation of a higher-order structure of the entire Nup84 complex within the NPC.

Thereupon, a model for the membrane-coating cylinder of the NPC was proposed (Figure 7). In this model, the elongated Sec13•Nup145 structure would form vertical poles within the NPC. The bent rod could follow the membrane

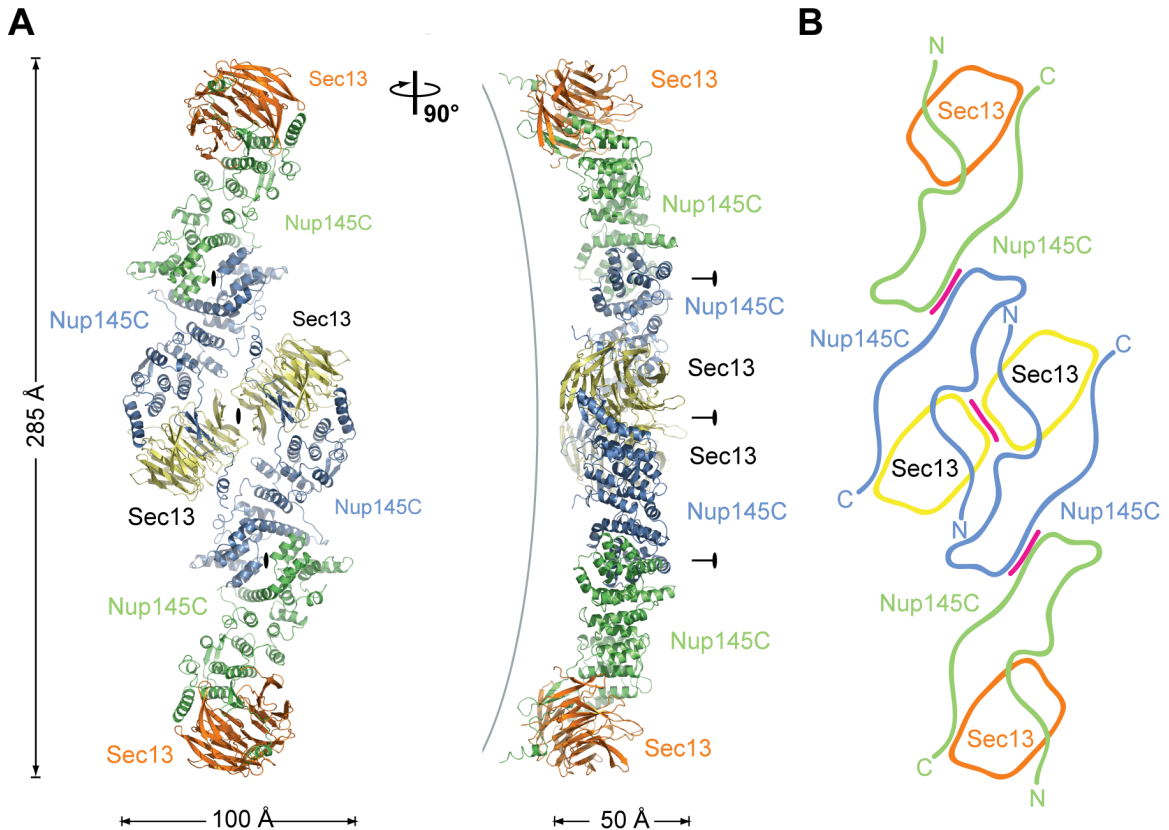


Figure 6: Crystal structure of the hSec13•Nup145C complex

A) The chimeric hSec13•Nup145C hetero-octamer with hSec13 in orange and yellow and Nup145C in green and blue. On the right, a 90° rotated view is presented. The overall dimensions, the curvature of the hetero-octamer and the two-fold symmetries are indicated. B) A schematic representation of the hetero-octamer in the same color code as in panel A. The domain invasion motif is indicated by invading lines and the homo-dimerization regions by pink lines (Hsia et al., 2007).

curvature of the pore membrane domain. Due to the internal two-fold symmetries between the hetero-dimers, four Nup84 complexes would be stacked in an anti-parallel manner. In accordance with the eight-fold rotational symmetry of the NPC, eight Nup84 complexes would arrange in a head-to-tail fashion to form a ring, of which four would form a concentric cylinder within the NPC. Strikingly, this model with a height of almost 300 Å and a diameter of around 1000 Å fits the overall dimensions and symmetric properties of the yeast NPC and could coat the entire pore membrane domain of the nuclear envelope.

Introduction

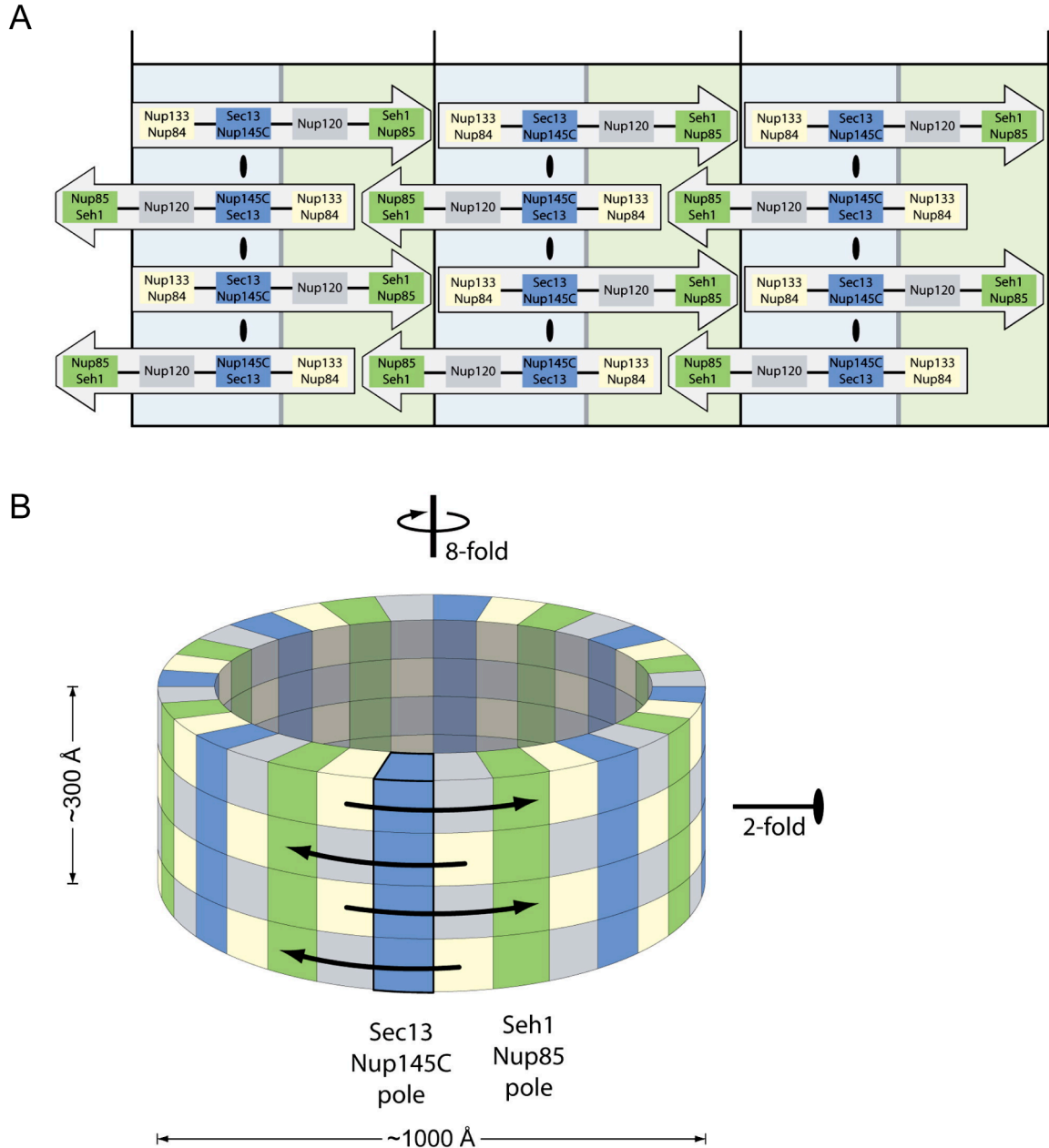


Figure 7: Model for the coating cylinder of the NPC

A) The hSec13•Nup145C hetero-octamer (blue) links four Nup84 complexes (represented as an arrow) in an anti-parallel fashion and eight Nup84 complexes form one out of four rings, which are stacked with opposite directions. The two-fold symmetries in the hetero-octamer and the approximate location of the other subunits of the Nup84 complex are indicated. B) A three-dimensional representation of the proposed model that indicates the symmetric properties and the overall dimensions (Hsia et al., 2007).

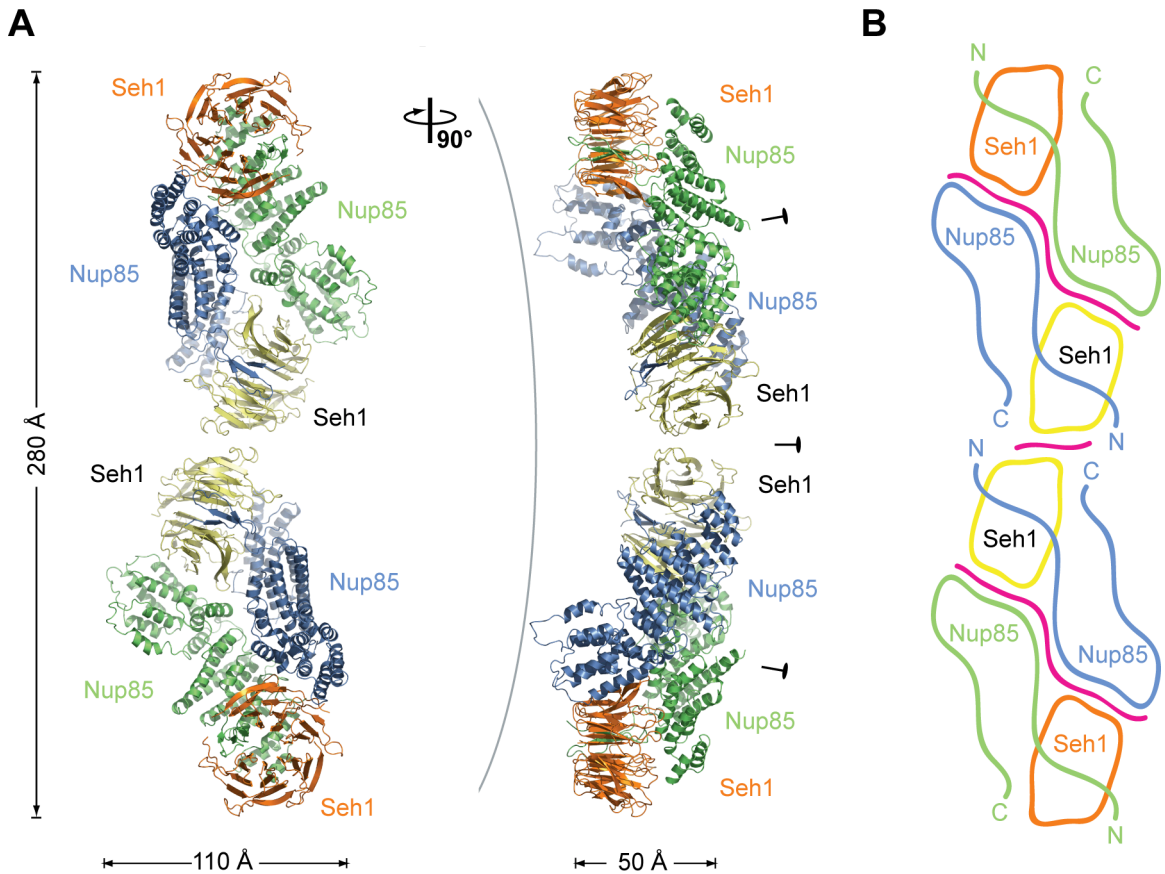


Figure 8: Crystal structure of the Seh1•Nup85 complex

The Seh1•Nup85 hetero-octamer with Seh1 in orange and yellow and Nup85 in green and blue. On the right, a 90° rotated view is presented. The overall dimensions, the curvature of the hetero-octamer and the two-fold symmetries are indicated. B) A schematic representation of the hetero-octamer in the same color code as in panel A. The domain invasion motif is indicated by invading lines and the homo-dimerization regions by pink lines (Debler et al., 2008).

Based on the sequence similarity as well as similar secondary structure and fold predictions of Sec13 with Seh1 and Nup145C with Nup85, the Seh1•Nup85 complex was proposed to form a second vertical pole in the membrane-coating cylinder (Hsia et al., 2007). Indeed, the crystal structure of the Seh1•Nup85 complex closely resembles the structure of the Sec13•Nup145C complex (Figure 8) (Debler et al., 2008). The N-terminal domain invasion motif of Nup85 completes the open 6-bladed β -propeller of Seh1 and the C-terminal part of the Nup85 fragment folds into a U-shaped α -helical solenoid. Furthermore, the

crystal structures of three different crystal forms captured a bent hetero-octameric rod, 280 Å in length, which is close to the observed height of the NPC and closely matches the dimensions of the Sec13•Nup145C hetero-octamer. The biochemical analysis of the Seh1•Nup85 complex demonstrated the formation of

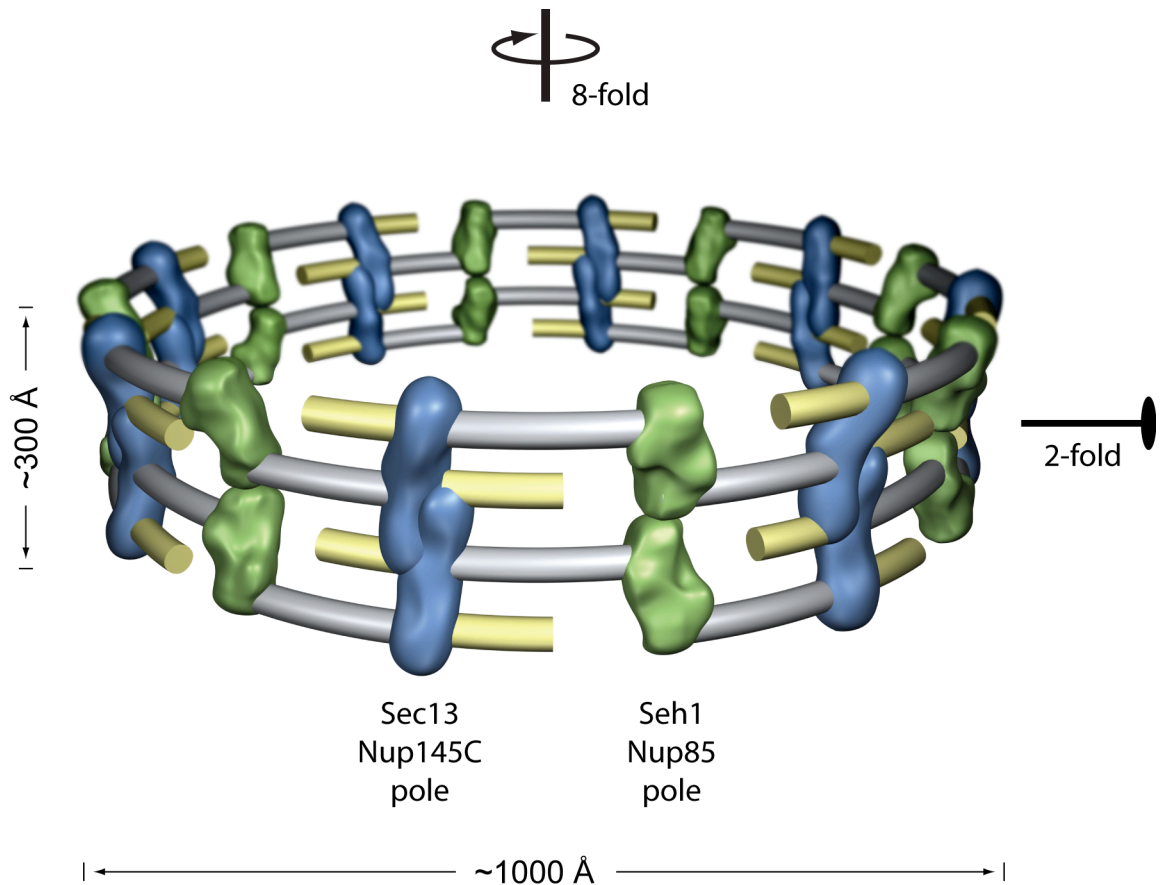


Figure 9: Refined model for the coating cylinder of the NPC

The hSec13•Nup145C and Seh1•Nup85 hetero-octamers form 16 alternating rods that connect 32 Nup84 complexes to a higher-order structure in the form of a porous “fence-like” cylinder (Debler et al., 2008; Hsia et al., 2007).

an oligomer in form of a hetero-tetramer in solution. Overall, the structure of the Seh1•Nup85 complex supports the proposed model for the structure of the membrane-coating cylinder of the NPC and gave valuable new insights that proved the predications of the originally propose (Figure 9).

Another key prediction of the original model is the head-to-tail arrangement of the Nup84 complex in the form of a closed ring. This proposal in the described model, is further supported by experimental data, obtained *in vitro* and *in vivo*, that demonstrate an interaction of the N-terminal domain of Nup133 with Nup120, two proteins located at opposite ends of the Nup84 complex (Seo et al., 2009)

Interestingly, at the same time, the structure of the yeast Sec13 in complex with yeast Sec31 was determined (Fath et al., 2007). The Sec13•Sec31 hetero-dimer is a component of the COPII complex, a membrane-coating complex of vesicles trafficking from the endoplasmic reticulum to the Golgi apparatus. The COPII complex is composed of five proteins: the membrane associated Sar1•GTP, Sec23 and Sec24 forming the inner shell of the coat, and Sec13 and Sec31 forming the outer shell of the coat (Figure 10A). In the crystal structure, Sec13 also folds into a 6-bladed β -propeller that is completed to a 7-bladed β -propeller in a similar fashion as observed in the hSec13•Nup145C and Seh1•Nup85 structures. In this case, the domain invasion motif provided by Sec31 as well as the Sec13 β -propeller are situated between the N-terminal β -propeller and the C-terminal α -helical solenoid of Sec31. Overall, the Sec31 α -helical solenoid folds into a U-shaped α -helical solenoid, similarly to Nup145C and Nup85, but it is more extended. The crystal structure further revealed that two U-shaped Sec31 solenoids homo-dimerize via their kink regions in analogy to the Nup145C and Nup85 homo-dimerizations (Figure 10B). While no oligomerization of the yeast Sec13•Sec31 complex could be detected in solution, the highly conserved human Sec13•Sec31 complex assembles into higher-order structures *in vitro*. In fact, the formation of spherical cages of variable size was observed by electron microscopy (Stagg et al., 2006; Stagg et al., 2007; Stagg et al., 2008). The crystal structure of the yeast Sec13•Sec31 complex could be fitted into the higher-order EM structure of the human Sec13•Sec31 complex (Figure 10C). Based on the docking of the yeast crystal structure, into the three-dimensional EM structure of the human Sec13•Sec31 shell, the yeast Sec13•Sec31 hetero-

tetramer was proposed to form hetero-octameric units by homo-dimerization of the Sec31 β -propellers to assemble the outer shell of the COPII complex (Fath et al., 2007).

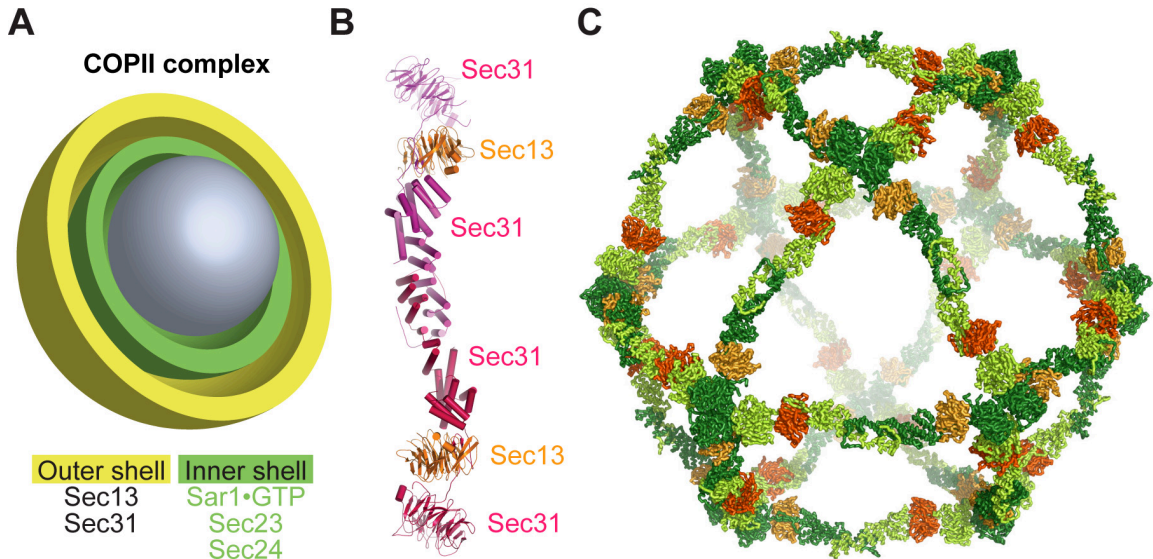


Figure 10: Structure of the outer shell of the COPII complex

A) Schematic representation of a COPII coated vesicle. B) The structure of the yeast Sec13•Sec31 complex shows Sec13 in orange and Sec31 in pink. Note the N-terminal β -propeller of Sec31 followed by the domain invasion motif and the U-shaped solenoid. C) Three-dimensional model of the outer shell of the COPII complex derived from crystal structure fitting of yeast Sec13•Sec31 into a higher-order EM structure of human Sec13•Sec31. Sec13 is colored in orange and red, Sec31 in dark and light green (Fath et al., 2007).

The strong structural similarities between the Sec13•Sec31 crystal structure and the hSec13•Nup145 and Seh1•Nup85 structures, as well as the evolutionary relation of the COPII and Nup84 complexes, strengthens the hypothesis that the observed homo-dimerization of Nup84 complex subunits are important for the formation of higher-order structures of the entire Nup84 complex within the NPC.

3.5. Further Models for the Arrangement of Nup84 Complexes in the NPC

Two additional models have been proposed for a higher-order structure of the Nup84 complex within the NPC. The *lattice model* (Brohawn et al., 2008) is

based on the homology between nucleoporins of the Nup84 complex and Sec31 of the COPII complex as well as a structural similarity with clathrin and COPII complexes. Structural information together with structure predictions revealed high structural similarities between Nup84, Nup85, and Nup145C of the Nup84 complex, Nic96 (another yeast nucleoporin), and Sec31 of the COPII complex. The term Ancestral Coatomer Element 1 (ACE1) was introduced for a tripartite structural element of crown, trunk, and tail common to these proteins. The Nup84

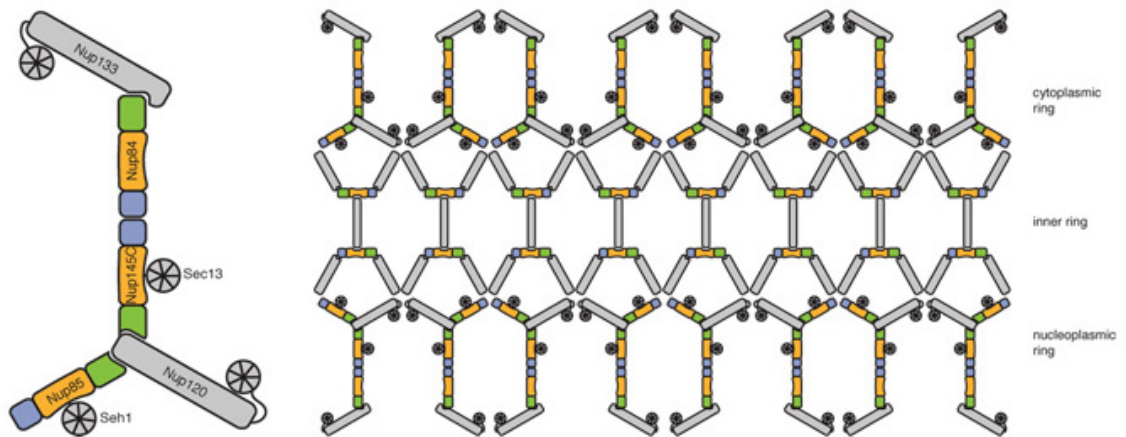


Figure 11: Lattice model for the Nup84 complex

The crown (blue), trunk (orange), and tail (green) subdomains forming the ACE1 of Nup85, Nup145C, and Nup84 α -helical solenoids are indicated in the schematic representation of one Nup84 complex on the left. The proposed higher-order structure is shown on the right. 16 copies of the Nup84 complex are arranged along the nucleocytoplasmic axis forming two peripheral rings connected by the Nic96 complex. Non-ACE1 proteins are illustrated in gray (Brohawn et al., 2008).

complex without Nup84 and Nup133 has similarity to the clathrin triskelion that forms the polygonal cage around a vesicle. The Nup84 complex together with the Nic96 complex are proposed to form a lattice-like coat with edges and vertices similar to clathrin and COP complexes. According to this model, eight Nup84 complexes are arranged along the nucleocytoplasmic axis of the NPC forming one ring each at the nucleoplasmic and cytoplasmic face of the NPC, with

Nup133 facing into the periphery. The Nic96 complex was proposed to connect the nuclear and the cytoplasmic ring of Nup84 complexes (Figure 11).

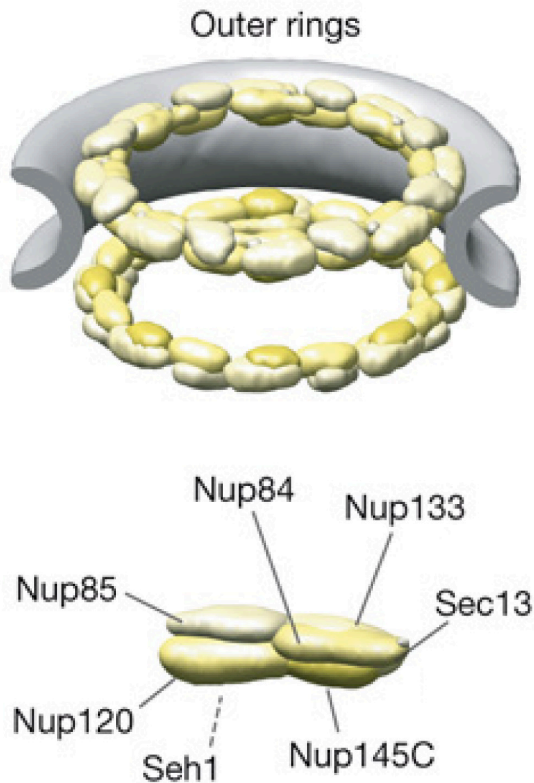


Figure 12: Computational model for the Nup84 complex within the NPC

A computational model of the entire NPC illustrates how eight Nup84 complexes are arranged to form an outer ring on both sides of the NPCs. In the bottom panel a magnification of one Nup84 complex is depicted. The subunits of the Nup84 complex are labeled (Alber et al., 2007b).

Rout, Chait and Sali proposed a “computational model” of the entire NPC that was derived from a broad set of biochemical, biophysical, and proteomics data together with a fixed stoichiometry (Alber et al., 2007a; Alber et al., 2007b). In this model, 16 copies of Nup84 complexes form two peripheral rings referred to as outer rings. Two linking inner rings are composed of Nup157, Nup170, Nup188, and Nup192. This core scaffold is sandwiched in between of a membrane ring and FG-repeat containing proteins. The proposed structure of the Nup84 complex is different from the observed EM structure. Therefore, it is not possible

to say what orientation the Nup84 complex adopts with respect to the NPC. It is, however, proposed to form two peripheral rings.

4. Aim of this Thesis

In an attempt to determine the high-resolution structure of the NPC, a piece-by-piece approach has been employed that yielded atomic-resolution structures of single nucleoporins and smaller subcomplexes of the NPC. The structure of the heptameric Nup84 complex has been especially well characterized by an interdisciplinary approach employing X-ray crystallography combined with EM. The aim of this thesis is the structural analysis of the yeast Sec13•Nup145C•Nup84 complex, the centerpiece of the Nup84 complex, by X-ray crystallography. The structure will represent a key module for fitting into a previously obtained three-dimensional EM reconstruction of the entire Nup84 complex. Furthermore, it will be extremely valuable to test and evaluate the proposed NPC models. As the largest building block of the NPC that has been crystallographically analyzed so far, this structure would substantially contribute to our understanding about molecular principles as well as mechanistic details of NPC components on the atomic level.

II. Results

1. Domain Structures of Sec13, Nup145C, and Nup84

The *S. cerevisiae* Sec13 is composed of 297 residues with 6 WD40 repeats that fold into a β -propeller (Figure 13) (Fath et al., 2007; Saxena et al., 1996). Sequence conservation analysis of Sec13 revealed high sequence identity and similarities among all eukaryotes (Figure 14) (Hsia et al., 2007). Interestingly, the major part of the Sec13 sequence is either identical or similar to that of Seh1 – another subunit of the Nup84 complex (Figure 14) (Hsia et al., 2007; Siniosoglou et al., 1996).

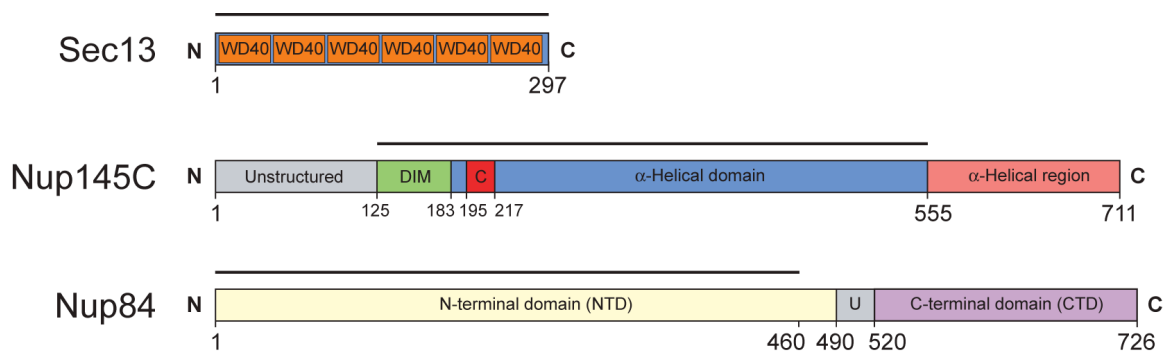


Figure 13: Domain structures of Sec13, Nup145C, and Nup84.

For Sec13, the six WD40 repeats (orange) are indicated. For Nup145C, the unstructured N-terminal region (gray), the domain invasion motif (DIM) (green), the α B- α C connector (C) (red), the α -helical domain (blue), and the C-terminal α -helical region (pink) are indicated. For Nup84, the N-terminal domain (NTD) and C-terminal domain (CTD) are indicated. These domains are separated by an unstructured linker (U). The residue numbering is shown below and the bars above the domain structures mark the fragments of the three proteins used for crystallization.

According to secondary structure predictions of *S. cerevisiae*, Nup145C can be divided into an N-terminal domain of 125 residues lacking any apparent structural elements followed by a C-terminal region that had been predicted to fold into an α -helical solenoid domain. The previously determined crystal structure of

Results

Nup145C (residues 125-555) in complex with human Sec13 (Hsia et al., 2007) revealed further structural motifs within this region: the domain invasion motif

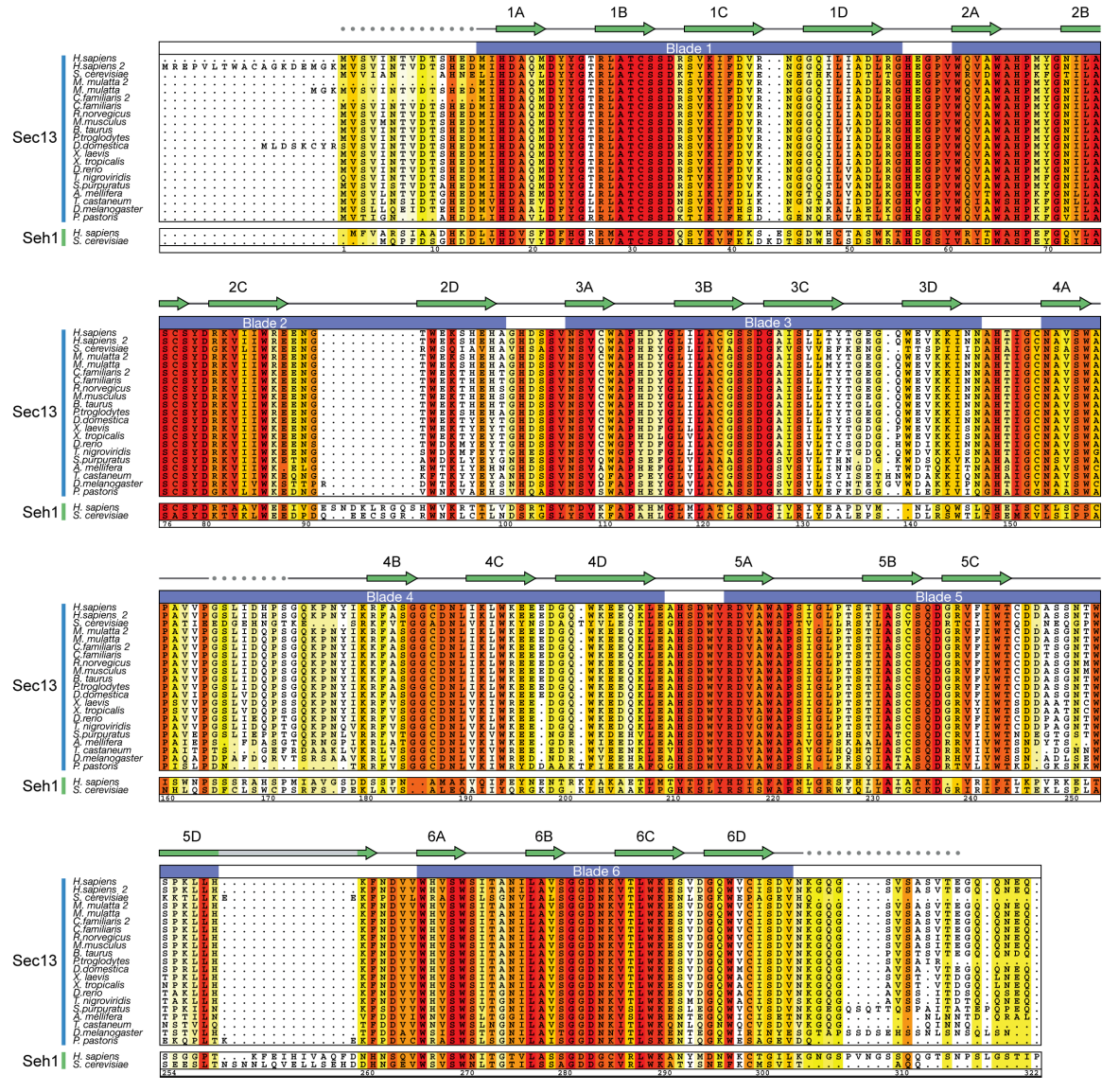


Figure 14: Multispecies sequence alignment of Sec13

The numbering below the alignment is relative to *H. sapiens* Sec13. The overall sequence conservation at each position is shaded in a color gradient from yellow (40 % similarity) to dark red (100 % identity), residues in white are not conserved. The secondary structure of the human Sec13 is indicated above the sequence as green arrows (β -strands), gray lines (coil regions), and gray dots (disordered residues). Seh1 has a longer C-terminal tail than Sec13 and a unique insertion in the 5D-6A inter-blade connector, which is not conserved in Sec13. For clarity, these residues have been omitted from the alignment. This figure is a slightly modified version of a figure published by (Hsia et al., 2007).

Results

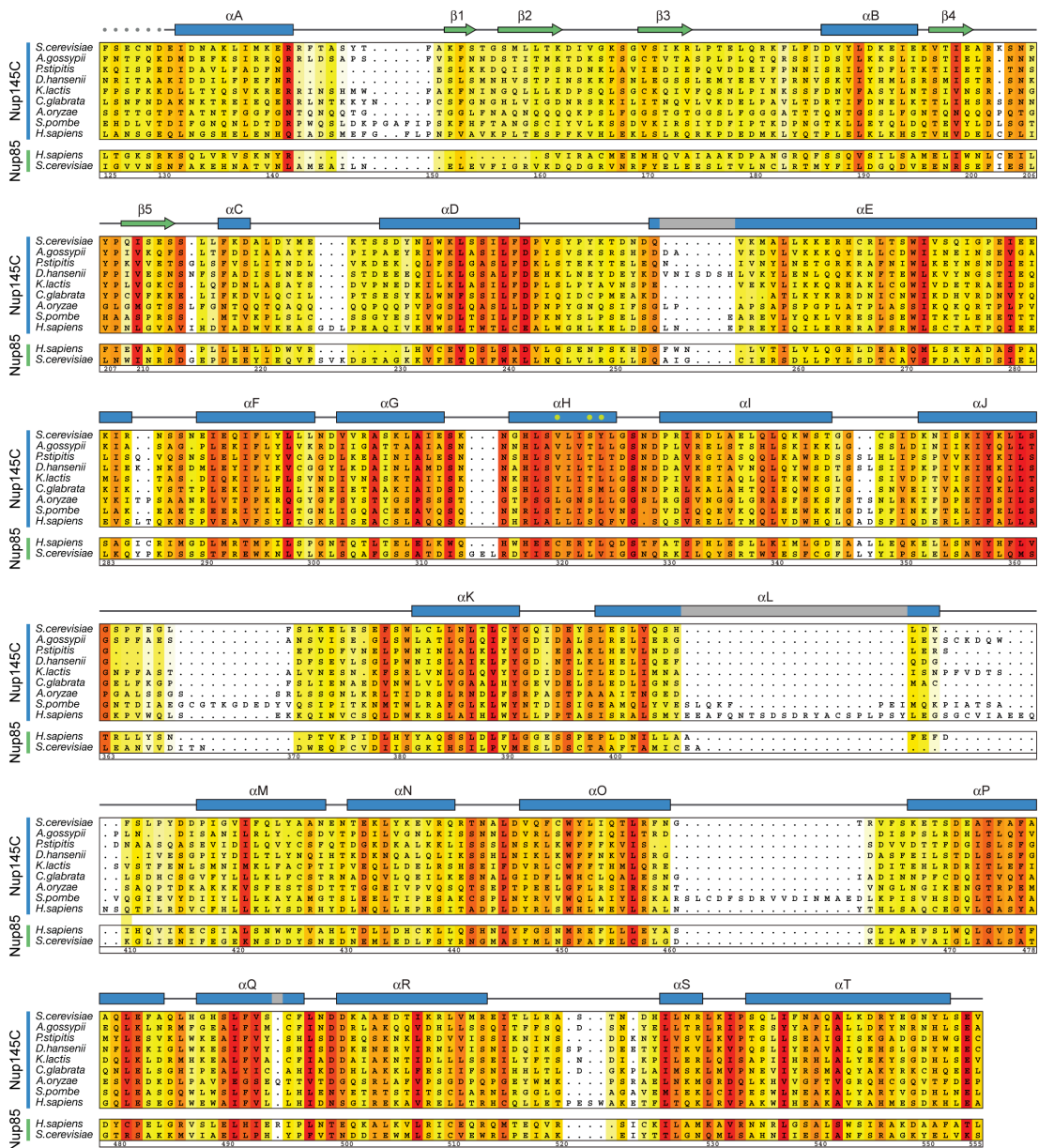


Figure 15: Multispecies sequence alignment of Nup145C

The numbering below the alignment is relative to *S. cerevisiae* Nup145C. The overall sequence conservation at each position is shaded in a color gradient from yellow (60 % similarity) to red (100 % identity), residues in white are not conserved. The secondary structure is indicated above the sequence as blue boxes (α -helices), green arrows (β -strands), gray lines (coil regions), and gray dots (disordered residues). The positions of the three residues (Val-320, Ser-323 and Tyr-324 located in helix α H) that abolish complex formation with Nup84 when mutated to Glu, Glu, and Ala, respectively are indicated by green dots (section II.5.4.) (Brohawn et al., 2008). The *H. sapiens* Nup145C homolog is termed Nup96. Note also the similar sequence of Nup85. This figure is a slightly modified version of a figure published by (Hsia et al., 2007).

Results

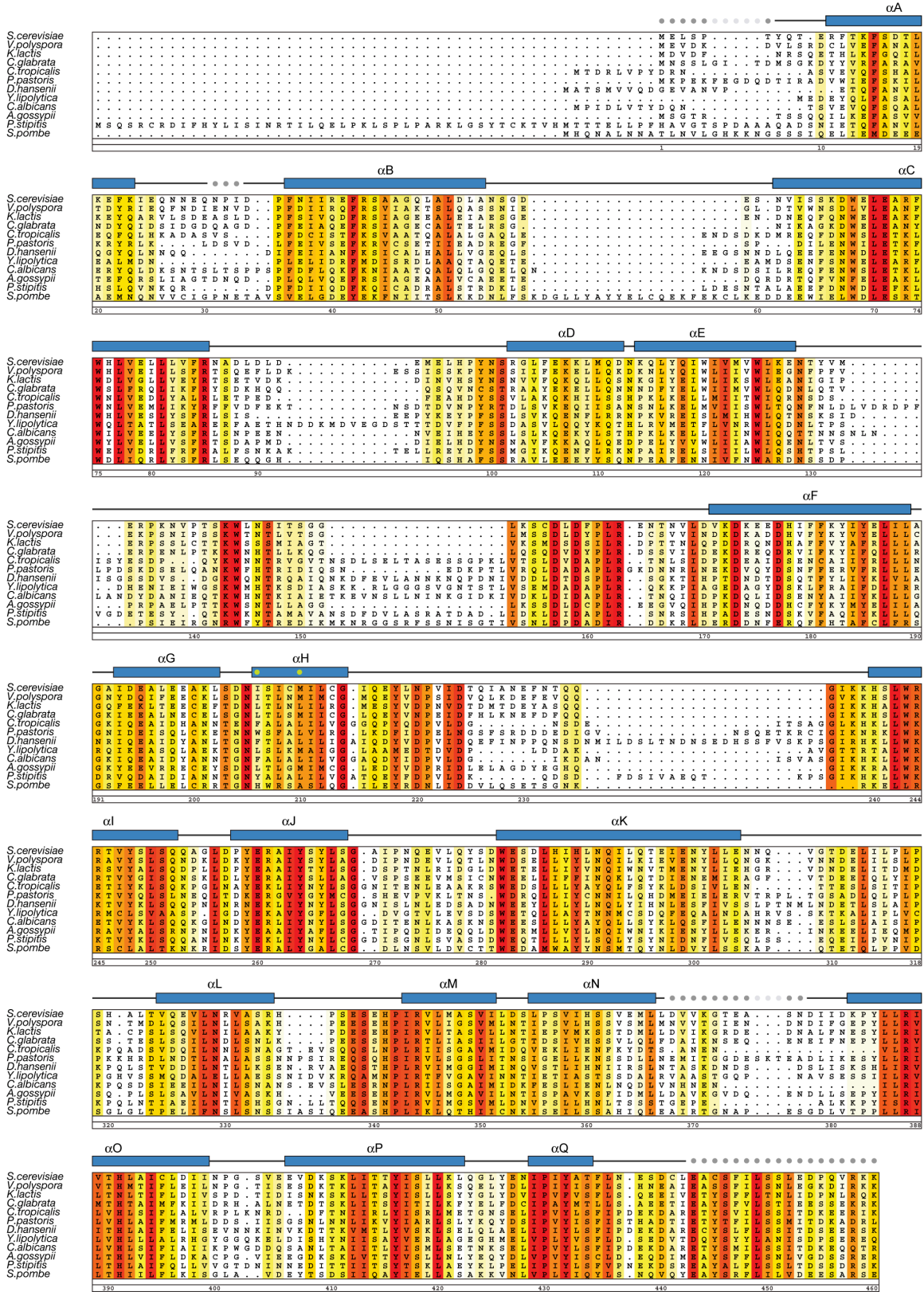


Figure 16: Multispecies sequence alignment of Nup84

Results

Multispecies sequence alignment of Nup84 homologs. The numbering below the alignment is relative to *S. cerevisiae* Nup84. The overall sequence conservation at each position is shaded in a color gradient from yellow (60 % similarity) to red (100 % identity) residues in white are not conserved. The secondary structure is indicated above the sequence as blue boxes (α -helices), gray lines (coil regions), and gray dots (disordered residues). The positions of the two residues (Ile-206 and Met-210, located in helix α H) that abolish complex formation with Nup145C when mutated to Asp are indicated by green dots (section II.5.4.) (Brohawn et al., 2008).

(DIM), the distinct α B- α C connector, and the remaining α -helical domain that folds into a solenoid (Figure 13). The sequence of Nup145C is well conserved throughout many eukaryotic species and large parts are identical or similar to the sequence of Nup85, which is also a subunit of the Nup84 complex (Figure 15) (Hsia et al., 2007).

To investigate the domain organization of *S. cerevisiae* Nup84, sequence conservation analysis and secondary structure predictions were performed. Nup84 is comprised of 726 residues and predicted to be an all- α -helical protein that can be divided into two domains, separated by an unstructured linker of around 30 residues (Figure 13). Accordingly, a series of expression constructs for the N-terminal domain (NTD) was designed and, a stable fragment was identified which is composed of residues 1–460 – the major part of Nup84. In the remainder of the thesis, this fragment will be referred to as Nup84 NTD. The sequence of Nup84 is conserved among many yeast and fungi species (Figure 16).

2. Protein Purification

One of the challenges in protein X-ray crystallography is the production of the protein of interest. In particular, large quantities in the mg range and a high purity of more than 95 % of protein in a folded state are general requirements for successful crystallization.

Nup84 NTD could be solubly expressed with an N-terminal proteolytically cleavable hexa-histidine tag in BL21-CodonPlus (DE3)-RIL cells. Nup145C by itself is not soluble in BL21-CodonPlus (DE3)-RIL cells, but could be solubly co-expressed with its binding partner Sec13. The following sections describe the final multi-step purification procedures that routinely produced crystallization-grade proteins. A detailed flow chart of the purification protocol can be found in the Material and Methods section of this thesis (Figure 42).

2.1. Purification of Nup84 NTD

For the purification of the 55.5 kDa Nup84 NTD, the cell lysate was loaded onto a column filled with a Ni-NTA resin. Most proteins in the cell lysate did not bind to the Ni-NTA resin and were found in the unbound fraction, whereas Nup84 NTD elutes in a sharp peak fraction using increasing imidazole concentrations. This affinity chromatography step resulted in a high enrichment of Nup84 NTD. A clear shift to a lower molecular weight observed in SDS-PAGE after a digest with PreScission protease suggested that the N-terminal hexa-histidine tag could be proteolytically cleaved completely (Figure 17A and B). The resulting Nup84 NTD has a molecular mass of 53.4 kDa.

A second affinity chromatography step was performed to separate a possible uncleaved fraction of Nup84 NTD that could still contain the N-terminal hexa-histidine tag. Expectedly, Nup84 NTD eluted in the flow through fraction without binding to the column resin. The fraction that bound to the Ni-NTA resin contained mainly impurities demonstrating the efficiency of the proteolytic cleavage (Figure 17C and D).

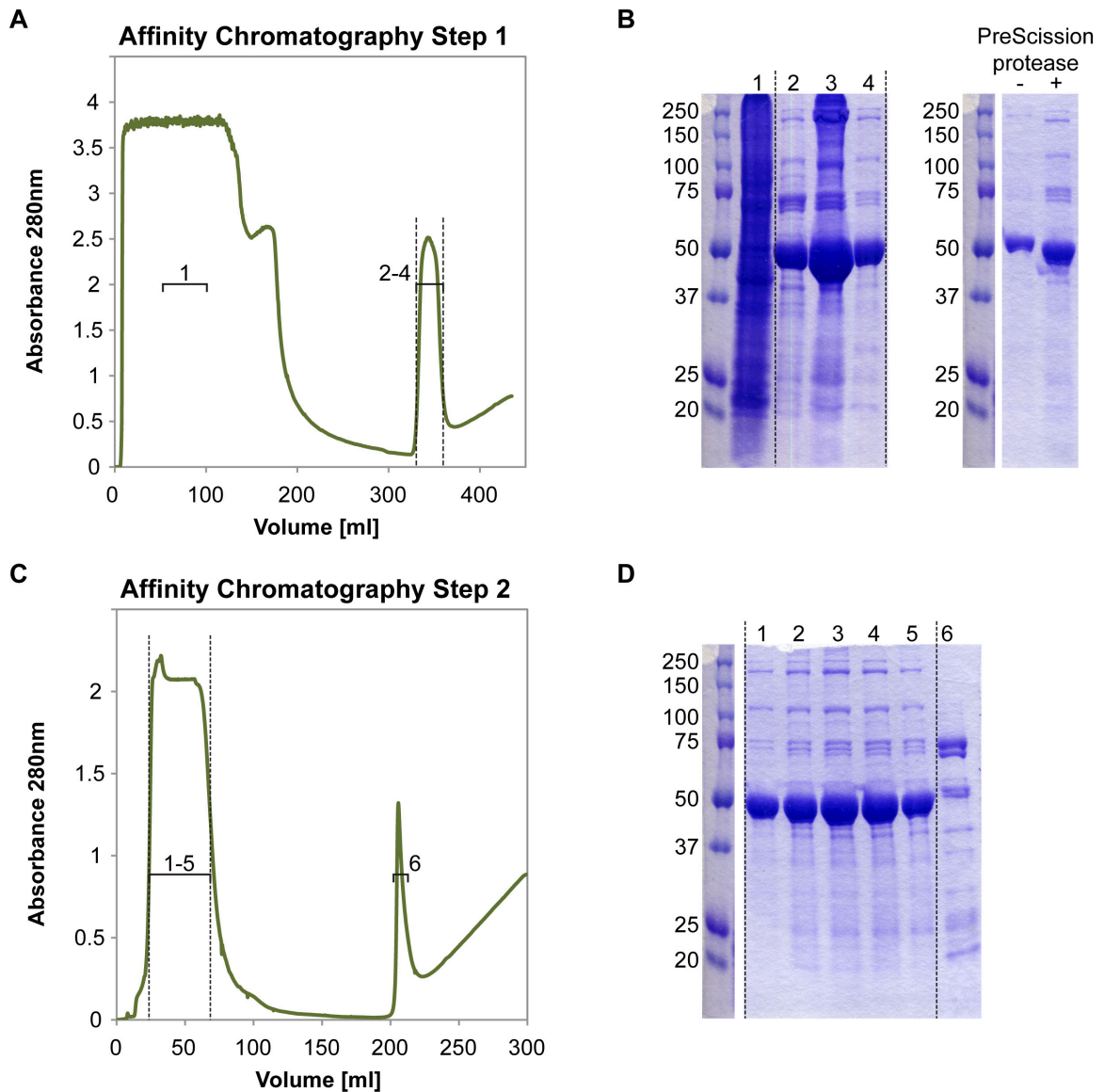


Figure 17: Purification of Nup84 NTD part I

A) Chromatogram of the first affinity chromatography step of Nup84 NTD. B) SDS-PAGE analysis of selected fractions indicated in panel A (on the left) and of samples before and after digest with PreScission protease (on the right). The marker bands are labeled with their molecular weight in kDa. C) Chromatogram of the second affinity chromatography step. D) SDS-PAGE analysis of selected fractions indicated in panel C. Chromatograms show the UV absorbance at 280 nm plotted against the volume. Fractions analyzed by SDS-PAGE are indicated with brackets in the chromatograms and pooled fractions are indicated with dashed lines in the chromatograms and the SDS-PAGE images.

A further enrichment of Nup84 NTD could be achieved by an anion exchange chromatography step. Nup84 NTD could be clearly separated from fractions

containing higher amounts of impurities by elution with gradually increasing NaCl concentrations (Figure 18A and B).

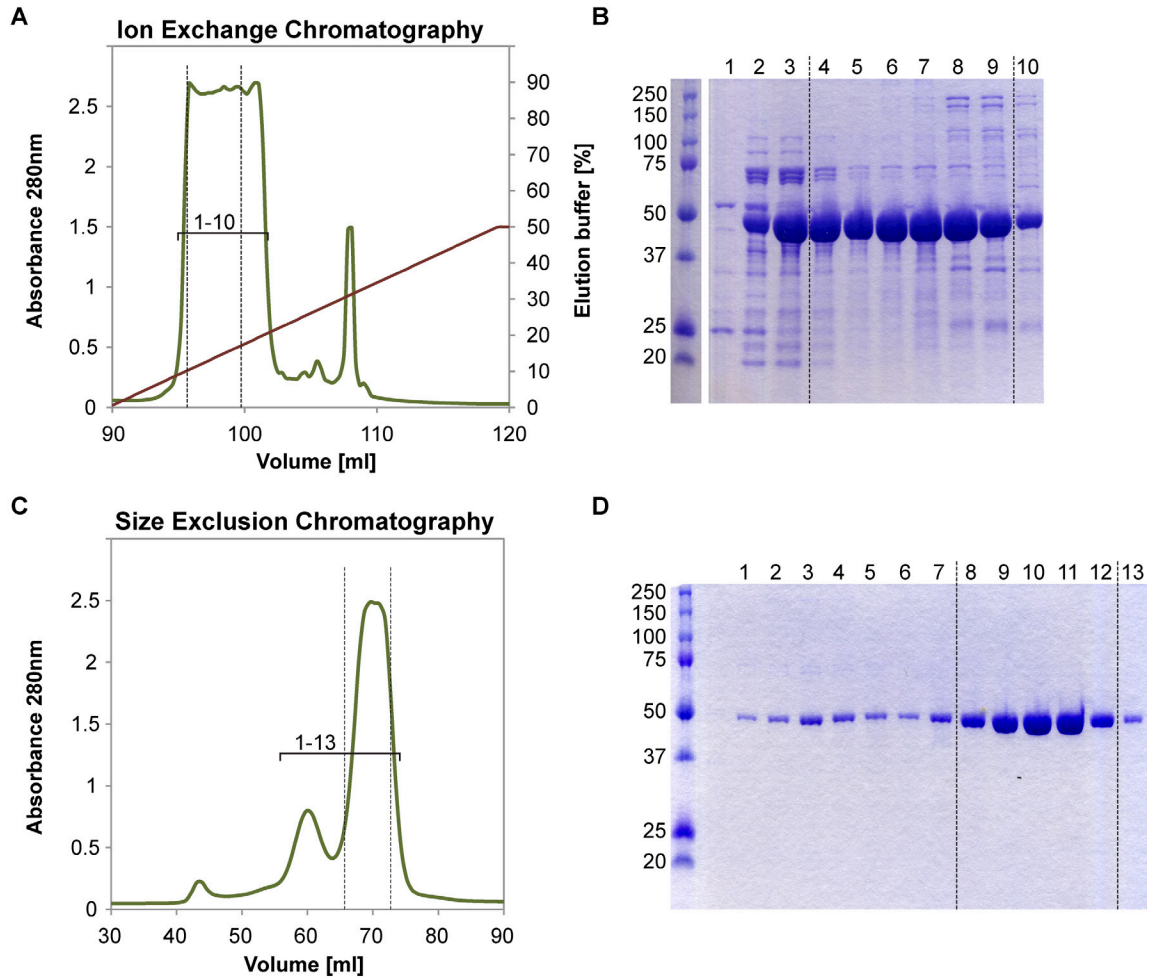


Figure 18: Purification of Nup84 NTD part II

A) Chromatogram of an anion exchange chromatography step (green) with the concentration gradient of the elution buffer (red). B) SDS-PAGE analysis of selected fractions indicated in panel A. The marker bands are labeled with their molecular weights in kDa. C) Chromatogram of a size exclusion chromatography step. D) SDS-PAGE analysis of selected fractions indicated in panel C. Chromatograms show the UV absorbance at 280 nm plotted against the volume. Fractions analyzed by SDS-PAGE are indicated with brackets in the chromatograms and pooled fractions are indicated with dashed lines in the chromatograms and the SDS-PAGE images.

A final size exclusion chromatography step could separate Nup84 NTD from essentially all remaining impurities visible by SDS-PAGE. Interestingly, next to

Results

the main peak, a smaller population of apparent higher molecular weight was detected. This peak fraction also contained pure Nup84 NTD and hints towards an oligomeric species of Nup84 NTD. (Figure 18C and D). Only the main peak fractions were pooled and used for crystallization.

This purification procedure for Nup84 NTD resulted in a product of high purity with a yield of up to 10 mg per 1l of bacterial cell culture.

2.2. Protein Purification of the Sec13•Nup145C Complex

Sec13 and Nup145C were co-expressed and subsequently co-purified by an affinity chromatography step. The N-terminal hexa-histidine tagged Nup145C (51.3 kDa) and the untagged Sec13 (33.0 kDa) bound to the Ni-NTA resin. Together the two proteins eluted from the column in a sharp peak with gradually increasing imidazole concentrations. The unbound fraction mainly contained impurities and excess of Sec13 (Figure 19A and B).

Further enrichment of the Sec13•Nup145C complex could be achieved by an anion exchange chromatography step. With gradually increasing NaCl concentrations, the Sec13•Nup145C complex eluted earlier than most impurities and could therefore be separated by restrictive pooling of relatively clean fractions (Figure 19B and C).

Final purification of the Sec13•Nup145C complex was achieved with a size exclusion chromatography step. Only minor impurities were visible after SDS-PAGE (Figure 19D and E).

This purification procedure for the Sec13•Nup145C complex resulted in a product of satisfying purity with a yield of up to 15 mg per 1l of cultured cells.

Results

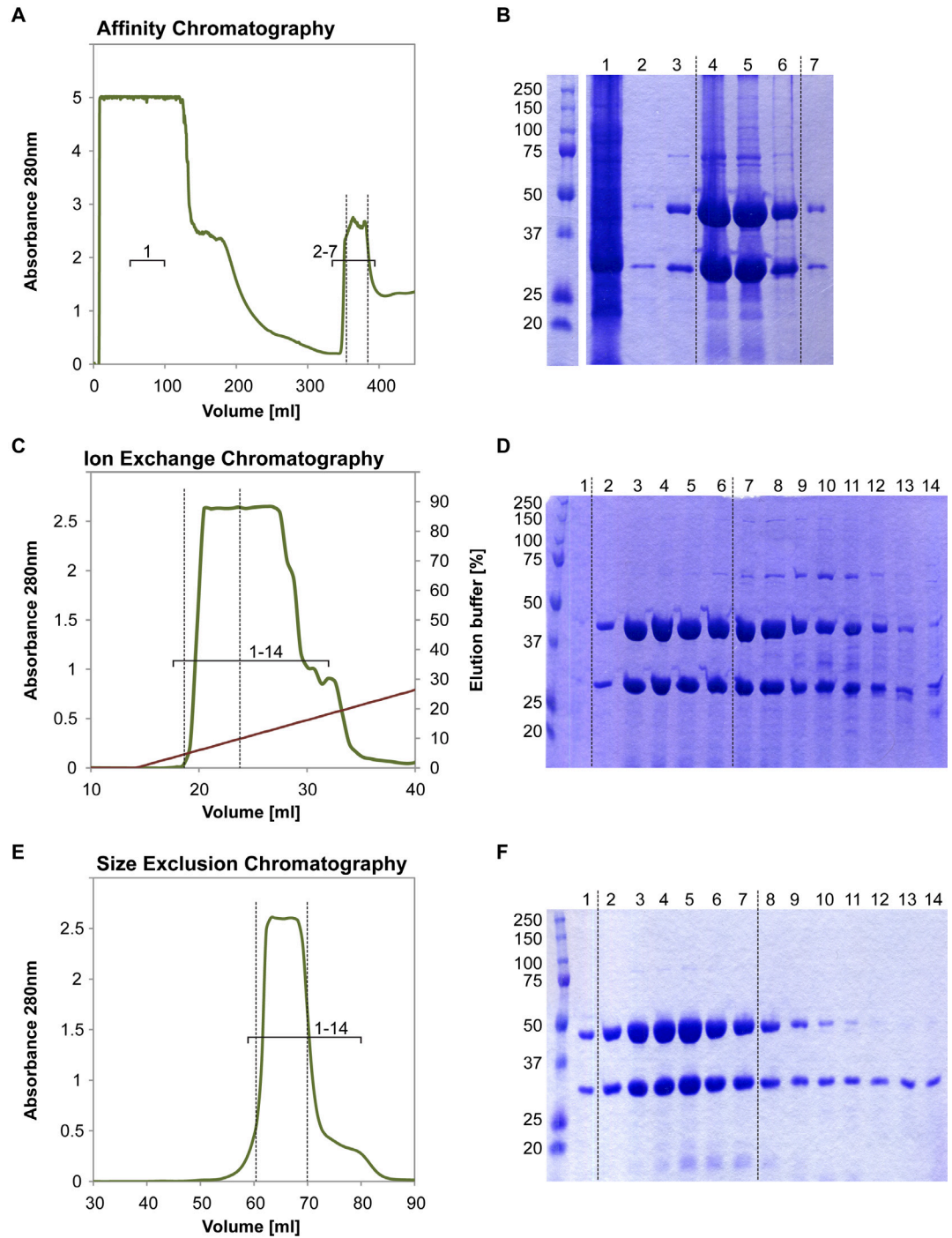


Figure 19: Purification of the Sec13•Nup145C complex

A) Chromatogram of an affinity chromatography step. C) Chromatogram of an anion exchange chromatography step (green) with the concentration gradient of the elution buffer (red). E) Chromatogram of a size exclusion chromatography step. B), D), and F) SDS-PAGE analysis of selected fractions indicated in panels A, C, and E, respectively. Chromatograms show the UV absorbance at 280 nm plotted against the volume.

Fractions analyzed by SDS-PAGE are indicated with brackets in the chromatograms and pooled fractions are indicated with dashed lines in the chromatograms and the SDS-PAGE images. The marker bands are labeled with their molecular weights in kDa.

2.3. Formation and Purification of the Sec13•Nup145C•Nup84 NTD Complex

The trimeric complex Sec13•Nup145C•Nup84 NTD was formed by mixing equimolar amounts (150 μ M) of the Sec13•Nup145C complex and Nup84 NTD. The complex formation was monitored by analytical size exclusion chromatography. Nup84 NTD with a molecular mass of 53.4 kDa elutes at a volume of 13.6 ml from the column and the Sec13•Nup145C complex (84.3 kDa) at volume of 13.3 ml. Upon incubation of the single components the peak shifts dramatically to a lower volume of 11.8 ml in accordance with the higher molecular mass of the trimeric Sec13•Nup145C•Nup84 NTD complex of 137.7 kDa (Figure 20A). The affinity of the two components of the trimeric complex seemed very high as almost all protein mass was converted into the trimeric complex. Only a minor peak at a higher volume and lower molecular mass was detected, which can very likely be attributed to the excess of one of the complex components. In accordance with this observation, the dissociation constant of the Sec13•Nup145C•Nup84 NTD complex amounts to approximately 7 nM as determined by isothermal titration calorimetry (Figure 21). The binding enthalpy of $\Delta H = -32.5$ kcal/mol and the entropy of $T\Delta S -21.4$ kcal/mol were determined by data fitting to a single-site model.

In a preparative scale, the trimeric Sec13•Nup145C•Nup84 NTD complex could be successfully separated from smaller amounts of its single components in excess (Figure 20B and C). The resulting product was of great purity and could be obtained in required quantities for crystallization experiments.

Results

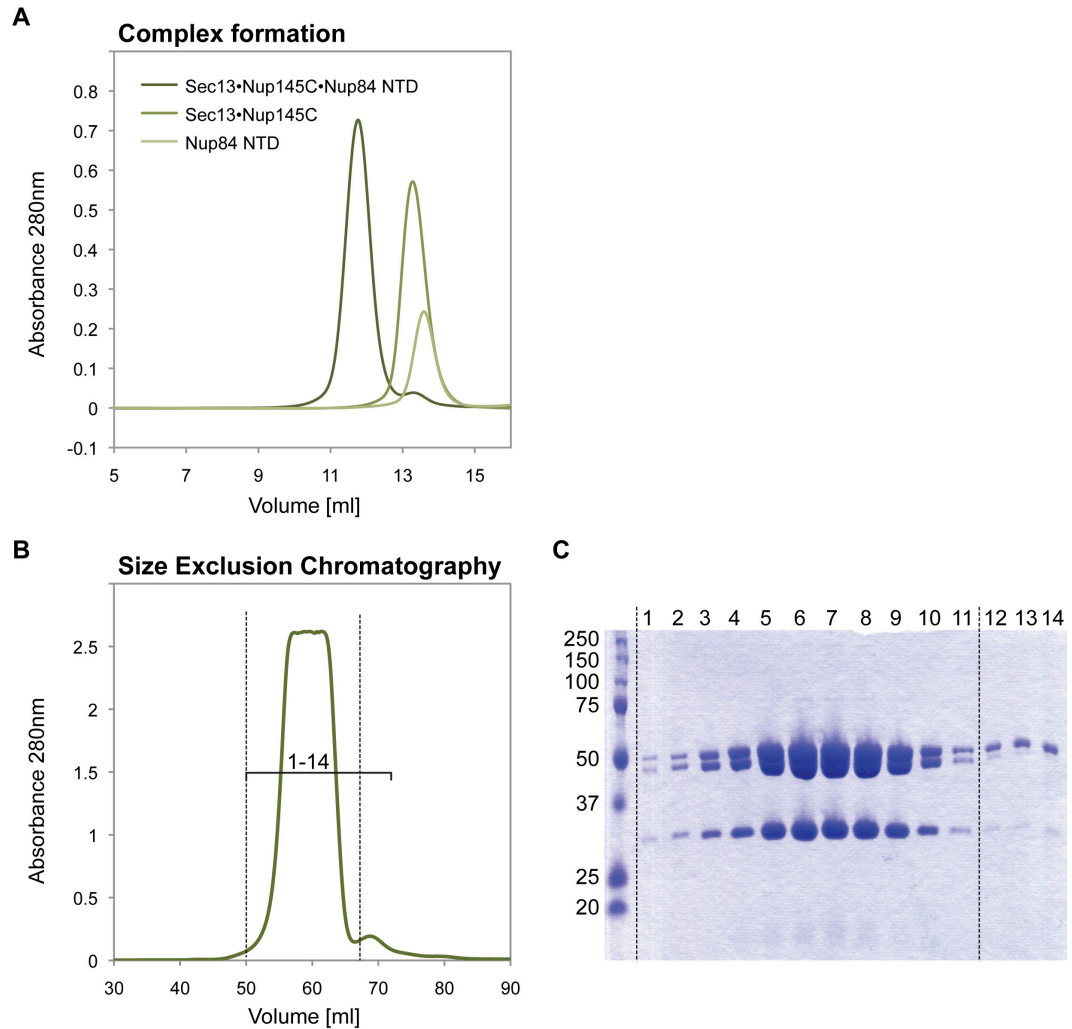


Figure 20: Complex formation of Sec13•Nup145C•Nup84 NTD

A) Analytical size exclusion chromatography of Nup84 NTD and Sec13•Nup145C I isolation and after incubation of the three proteins. B) Chromatogram of a preparative size exclusion chromatography step after incubation of Nup84 NTD with Sec13•Nup145C. C) SDS-PAGE analysis of selected fractions indicated in panel B. Chromatograms show the UV absorbance at 280 nm plotted against the volume. Fractions analyzed by SDS-PAGE are indicated with brackets in the panel B and pooled fractions are indicated with dashed lines in the panels B and C. The marker bands are labeled with their molecular weights in kDa.

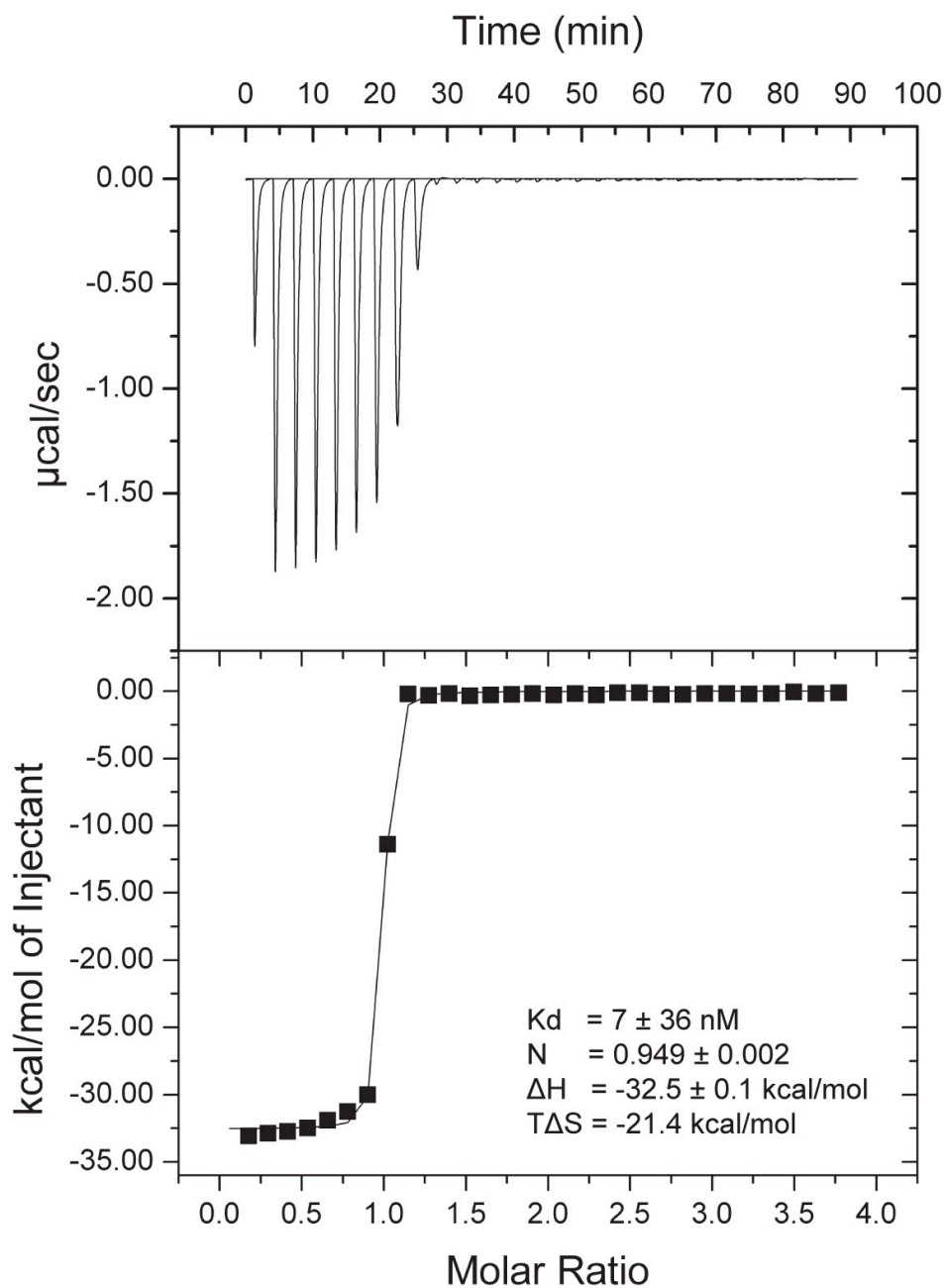


Figure 21: Isothermal titration calorimetry analysis of the trimeric Sec13•Nup145C•Nup84 NTD complex

The Nup84 NTD was titrated against the Sec13•Nup145C complex. The dissociation constant (K_d), the number of binding sites (N), the binding enthalpy (ΔH), and the entropy ($T\Delta S$) were derived by curve fitting using a single-site model.

3. Crystallization

During the crystallization of the Sec13•Nup145C complex (Hsia et al., 2007) as well as the Seh1•Nup85 complex (Debler et al., 2008), the oligomerization of the nucleoporin hetero-dimers led to the formation of hetero-octamers. Therefore, the trimeric complex of Sec13•Nup145C•Nup84 NTD is likely to also form oligomers during crystallization, which would tremendously increase the protein content of the asymmetric unit of the crystals. The asymmetric unit of a crystal is the smallest unit that contains all structural information. Various possible combinations of crystallographic symmetry operations applied to the asymmetric unit generate the unit cell of a crystal. A crystal is created by translation of the unit cell in three dimensions. In general one can say that the structure determination becomes more complicated with larger contents of the asymmetric unit. To obtain further structural information of the trimeric complex and in a result ease the structure determination, I aimed to crystallize and determine the structure of Nup84 NTD in isolation. This structure as well as the previously determined structures of hSec13•Nup145C and *S. cerevisiae* Sec13 (Fath et al., 2007; Hsia et al., 2007) would provide excellent search models for the structure determination of the whole trimeric complex by molecular replacement.

3.1. Crystallization of Nup84 NTD

Initial crystal showers of Nup84 NTD grew in 200 mM KCl and 20 % w/v PEG 3350 (Figure 22). Multiple rounds of screening and optimization by grid screens around the original crystallization condition at different temperatures and protein concentration with various additives and buffers did unfortunately not result in crystals with X-ray diffracting properties. Even further screening of a series of shorter and longer expression constructs did not give rise to diffracting crystals. In total several thousand conditions were tested for crystallization.



Figure 22: Crystals of Nup84 NTD

Feather-like protein crystals of Nup84 NTD after optimization.

3.2. Crystallization of the Sec13•Nup145C•Nup84 NTD Complex

Initial crystals of the trimeric Sec13•Nup145C•Nup84 NTD appeared in 1 out of more than 1000 screening conditions. The original crystallization condition contained 100 mM MES pH 6.5 and 12 % w/v PEG 20 000 (Figure 23). The crystals had an elongated shape and looked like clusters of multiple smaller long crystals that formed fiber-like structures.

Extensive optimization around the original conditions of the crystallization solution, protein concentrations, and crystallization temperature resulted in beautiful crystals with sharp edges and no visible surface defects. Optimized crystals grew at 20.5 °C with a reservoir solution of 100 mM MES pH 5.6, 1.5 % – 3.5 % w/v PEG 20 000, and 1 % – 6 % of methanol or glycerol.

The crystals typically appeared within a few days and reached their maximum size of up to (200 x 200 x 600) μm after approximately one to three weeks (Figure 24A). SDS-PAGE analysis of dissolved crystals revealed that the crystals contained 3 proteins and subsequent mass spectrometry confirmed that

complete fragments of full-length Sec13, Nup145C residues 125-555 and the full Nup84 NTD had crystallized (Figure 24D). The crystals diffracted to a resolution of 3.2 Å (Figure 25).

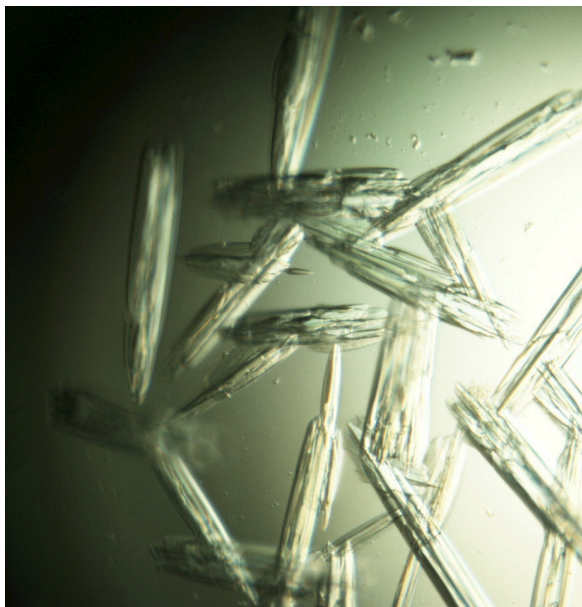


Figure 23: Initial crystals of the Sec13•Nup145C•Nup84 NTD complex

Long fiber-like crystal clusters of the Sec13•Nup145C•Nup84 NTD complex appeared in a crystallization screen.

Crystals of seleno-L-methionine labeled protein could be obtained and diffracted to a resolution of 4 Å.

Native crystals could successfully be derivatized with heavy metal compounds by soaking with saturated solutions of the heavy metal derivatives (Figure 24B and C). These crystals diffracted to lower resolution than native crystals as summarized in Table 1.

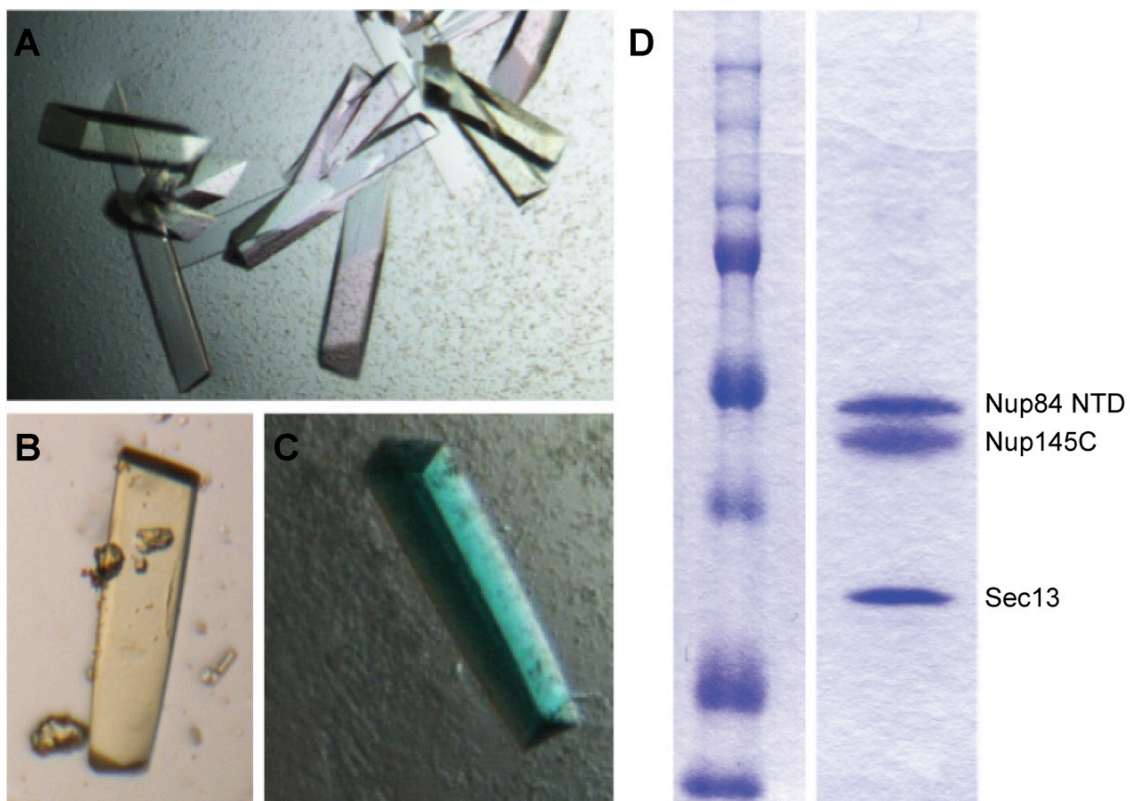


Figure 24: Optimization of crystal growth

A) Optimized native crystals and crystals soaked with (B) heavy metal derivatives Potassium Osmate (K_2OsO_4) and (C) Tantalum Bromide ($[Ta_6Br_{12}]^{2+}$). D) Dissolved native crystals analyzed by SDS-PAGE.

Results

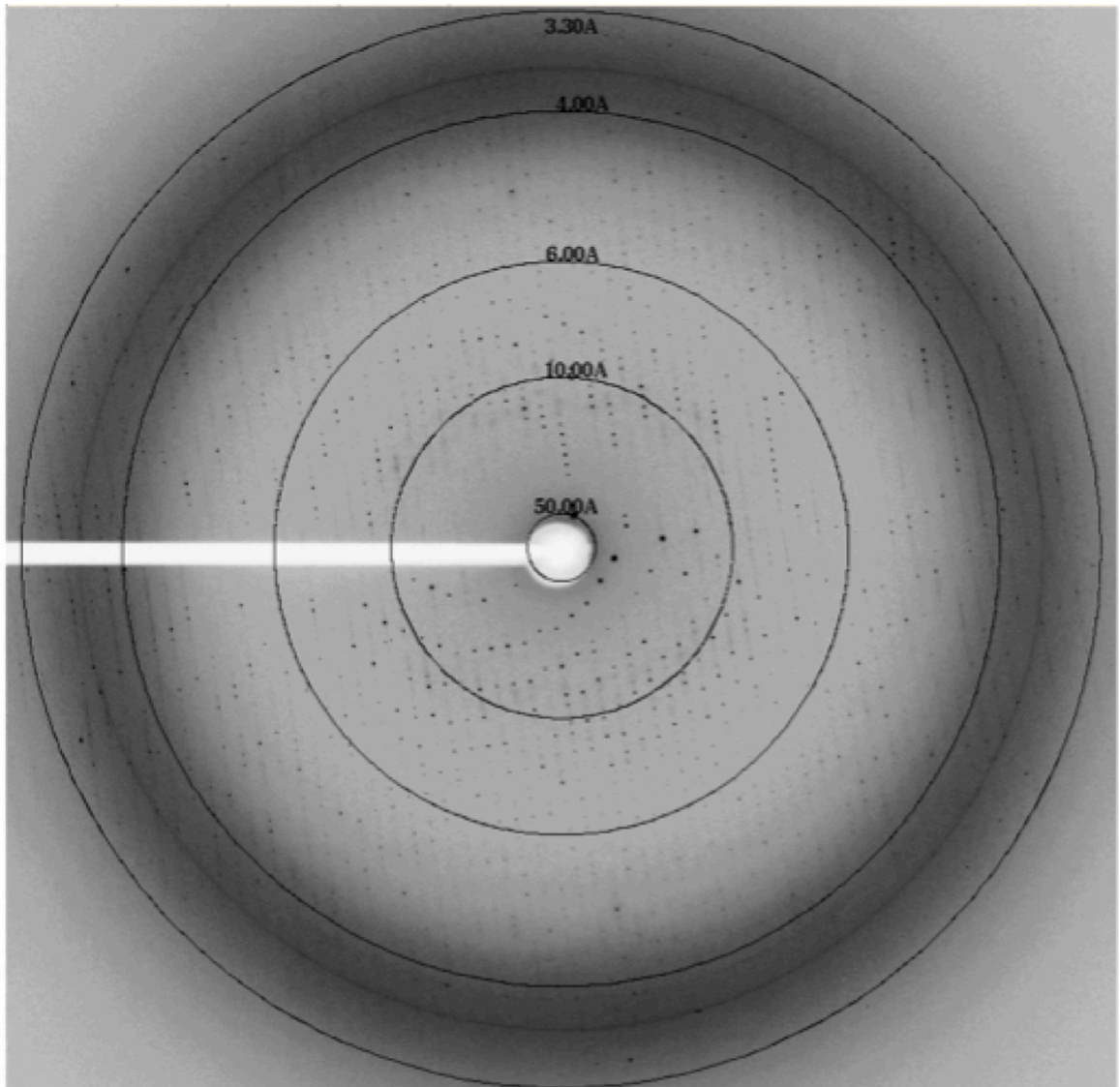


Figure 25: Diffraction pattern of native crystals

The diffraction pattern of a native crystal to a resolution of 3.3 Å. The resolution limits are indicated by circles.

4. Structure Determination

4.1. Data Collection and Processing

Diffraction experiments were performed at various beamlines at two different synchrotron light sources. The best results were obtained at the GM-CA/CAT beamlines at the Advanced Photon Source (APS). The diffraction patterns were analyzed to determine the space group and unit cell dimensions of the analyzed crystals. Native crystals of the ~140-kDa *S. cerevisiae* Sec13•Nup145C•Nup84 NTD hetero-trimer appeared in the orthorhombic space group $P2_12_12_1$ with unit cell dimensions of $a = 101 \text{ \AA}$, $b = 194 \text{ \AA}$, $c = 328 \text{ \AA}$; $\alpha = \beta = \gamma = 90^\circ$. Potassium osmate-derivatized and seleno-L-methionine-labeled protein crystals were almost isomorphous compared to native protein crystals with changes of the unit cell dimensions of less than 1 %. Axis dimensions of the unit cell of tantalum bromide-derivatized crystals were altered to more than 2 % for axes b and c compared to those of native data sets. Most screened crystals were not isomorphous and therefore, could not be used for phasing. Further data collection statistics are summarized in Table 1.

The Matthews coefficient allows estimating the number of molecules in the asymmetric unit of a crystal. It is a ratio of the volume of the unit cell and the product of the molecular mass, the number of asymmetric units and the number of macromolecules within the asymmetric unit. From an empirically observed range for the Matthews coefficient, the probable number of molecules in the asymmetric unit can be derived. For crystals of the Sec13•Nup145C•Nup84 NTD complex, probabilities of 0.05, 0.30, 0.53, and 0.11 for 3, 4, 5, and 6 copies of the trimeric complex per asymmetric unit, respectively, were suggested (Kantardjieff and Rupp, 2003; Matthews, 1968). This would correlate to molecular masses of ~415 kDa to 830 kDa per asymmetric units and solvent contents of 68 % down to 37 %.

Table 1: Data collection and refinement statistics

| | Crystal 1 Native | Crystal 2 [Ta ₆ Br ₁₂] ²⁺ | Crystal 3 K ₂ OsO ₄ | Crystal 4 SeMet |
|--|---|--|---|---|
| Data collection | | | | |
| Synchrotron | APS ^a | APS | APS | APS |
| Beamline | GM/CA-CAT | GM/CA-CAT | GM/CA-CAT | GM/CA-CAT |
| | 23ID-D | 23ID-D | 23ID-D | 23ID-B |
| Space group | P2 ₁ 2 ₁ 2 ₁ | P2 ₁ 2 ₁ 2 ₁ | P2 ₁ 2 ₁ 2 ₁ | P2 ₁ 2 ₁ 2 ₁ |
| Cell dimensions | | | | |
| <i>a</i> , <i>b</i> , <i>c</i> (Å) | <i>a</i> =101.4, <i>b</i> =194.1, <i>c</i> =327.8 | <i>a</i> =101.4, <i>b</i> =192.0, <i>c</i> =321.6 | <i>a</i> =101.4, <i>b</i> =193.4, <i>c</i> =324.7 | <i>a</i> =101.4, <i>b</i> =193.4, <i>c</i> =324.6 |
| α , β , γ (°) | α = β = γ =90 | α = β = γ =90 | α = β = γ =90 | α = β = γ =90 |
| | | <i>Ta peak</i> | <i>Os Peak</i> | <i>Se Peak</i> |
| Wavelength (Å) | 1.14006 | 1.25477 | 1.14016 | 0.97951 |
| Resolution (Å) ^b | 50.0-3.2 | 50.0-5.3 | 50.0-6.0 | 50.0-4.0 |
| | (3.31-3.20) | (5.49-5.30) | (6.21-6.00) | (4.14-4.00) |
| <i>R</i> _{sym} (%) ^b | 11.5 (52.5) | 11.7 (52.0) | 10.4 (41.0) | 10.3 (47.5) |
| $\langle I / \sigma I \rangle$ ^b | 16.1 (2.0) | 14.3 (2.7) | 15.9 (1.9) | 14.7 (2.3) |
| Completeness (%) ^b | 96.5 (75.9) | 99.8 (98.7) | 95.9 (72.1) | 96.8 (99.8) |
| Redundancy ^b | 7.5 (4.9) | 6.9 (5.0) | 6.9 (4.2) | 6.6 (4.6) |
| Refinement | | | | |
| Resolution (Å) | 50.0-3.2 | | | |
| No. reflections | 97,899 | | | |
| Test set | 9,887 (9.2 %) | | | |
| <i>R</i> _{cryst} / <i>R</i> _{free} (%) | 23.4 / 27.3 | | | |
| No. atoms | 27,039 | | | |
| R.m.s deviations | | | | |
| Bond angles (°) | 1.5 | | | |
| Bond lengths (Å) | 0.010 | | | |
| Ramachandran statistics ^c | | | | |
| Most favored (%) | 79.2 | | | |
| Additionally allowed (%) | 19.4 | | | |
| Generously allowed (%) | 1.4 | | | |
| Disallowed (%) | 0.0 | | | |

^aAPS, Advanced Photon Source, Argonne National Laboratory

^bHighest-resolution shell is shown in parentheses.

^cAs determined by Procheck

4.2. Molecular Replacement

It is a challenge to solve the atomic structure of macromolecular complexes by de-novo phasing - especially, if the content of the asymmetric unit is more than 400 kDa, as it has been estimated for the Sec13•Nup145C•Nup84 NTD complex

(II.4.1). However, in the case of the Sec13•Nup145C•Nup84 NTD complex, structural information has been available that may have eased the structure determination of the whole trimeric complex. More precisely, the crystal structures of hSec13•Np145C (PDB ID code 3BG1) (Hsia et al., 2007) and of the *S. cerevisiae* Sec13 (PDB ID code 2PM7) (Fath et al., 2007) were utilized as search models in an effort to solve the Sec13•Nup145C•Nup84 NTD complex structure by molecular replacement. Unfortunately, these attempts to solve the structure of the trimeric complex were fruitless.

4.3. Phasing with MIRAS

From diffraction experiments with protein crystals the amplitude of structure factors can be determined while the phase information of the structure factors is lost during the experiment. However, the phase information is crucial for the determination of a crystal structure. Multiple isomorphous replacement with anomalous signal (MIRAS) is a powerful method for de-novo phasing of macromolecular assemblies. Heavy metal derivatives are electron-rich compounds and create measurable changes in the diffraction intensities of crystals of derivatized proteins. These changes in diffraction intensities allow the determination of the phases of the structure factors.

The $[\text{Ta}_6\text{Br}_{12}]^{2+}$ cluster has been employed for phasing of crystal structures with high asymmetric unit content. The 856 electrons of one $[\text{Ta}_6\text{Br}_{12}]^{2+}$ cluster strongly contribute to the scattering power of the crystal (Knäblein et al., 1997). Many crystal structures have been phased and solved with $[\text{Ta}_6\text{Br}_{12}]^{2+}$ cluster-derivatized crystals (Hoelz et al., 2003; Murakami et al., 2002; Stavropoulos et al., 2006).

With a SAD (single anomalous dispersion) measurement of a $[\text{Ta}_6\text{Br}_{12}]^{2+}$ cluster derivative-soaked crystal, it was possible to locate the $[\text{Ta}_6\text{Br}_{12}]^{2+}$ cluster sites. The anomalous signal of the $[\text{Ta}_6\text{Br}_{12}]^{2+}$ cluster derivative was sufficient to determine initial approximate phases. These phases were used to locate and validate the heavy atom sites of potassium osmate (K_2OsO_4)-derivatized and

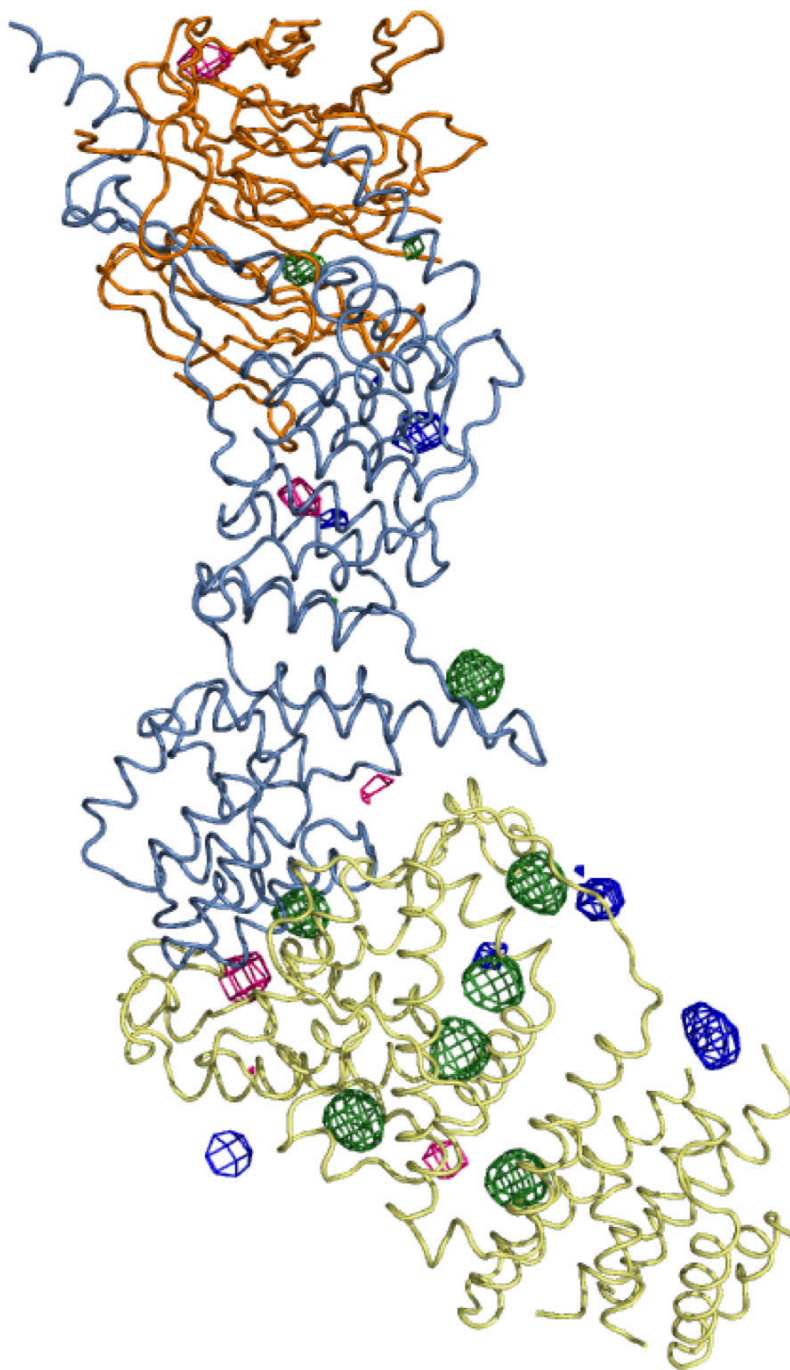


Figure 26: Anomalous difference Fourier maps

Illustrated are the selenium (green), osmium (pink), and $[\text{Ta}_6\text{Br}_{12}]^{2+}$ cluster (blue) sites, calculated from x-ray diffraction data of the different datasets. For clarity, only one of the four Sec13•Nup145C•Nup84 NTD complexes in the asymmetric unit is shown. Sec13, Nup145C, and Nup84 NTD are displayed in orange, blue, and yellow coil representation, respectively.

seleno-L-methionine-labeled protein crystals (Figure 26). Combined phasing using the isomorphous K_2OsO_4 and SeMet SAD and native datasets was carried out, followed by density modification with solvent flattening and histogram matching. These phases allowed the definition of the non-crystallographic symmetry (NCS) operators and the generation of NCS averaged maps. This procedure yielded an interpretable electron density map of high quality (Figure 27).

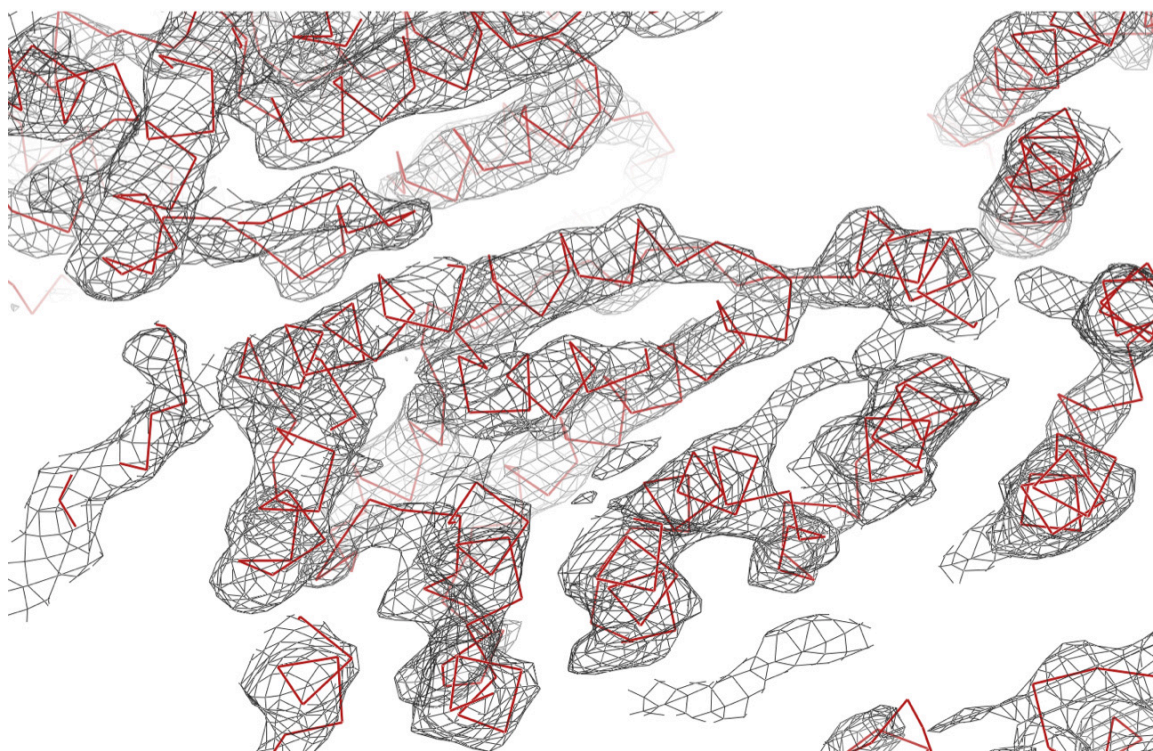


Figure 27: Experimental electron density map

The experimental electron density map of 3.2 Å resolution was calculated by multiple isomorphous replacement with anomalous signal (MIRAS). The map was contoured at 2.0 σ . The backbone of the final model is visible in red.

The crystallographic analysis of the trimeric Sec13•Nup145C•Nup84 NTD crystals revealed that the asymmetric unit harbored 3 copies of the Sec13•Nup145C•Nup84 NTD hetero-trimer. Even though on the low end of the estimated 3 to 6 copies based on the Matthews coefficient (II.4.1), the asymmetric unit of the crystals contained a protein mass of almost 420 kDa. The

Results

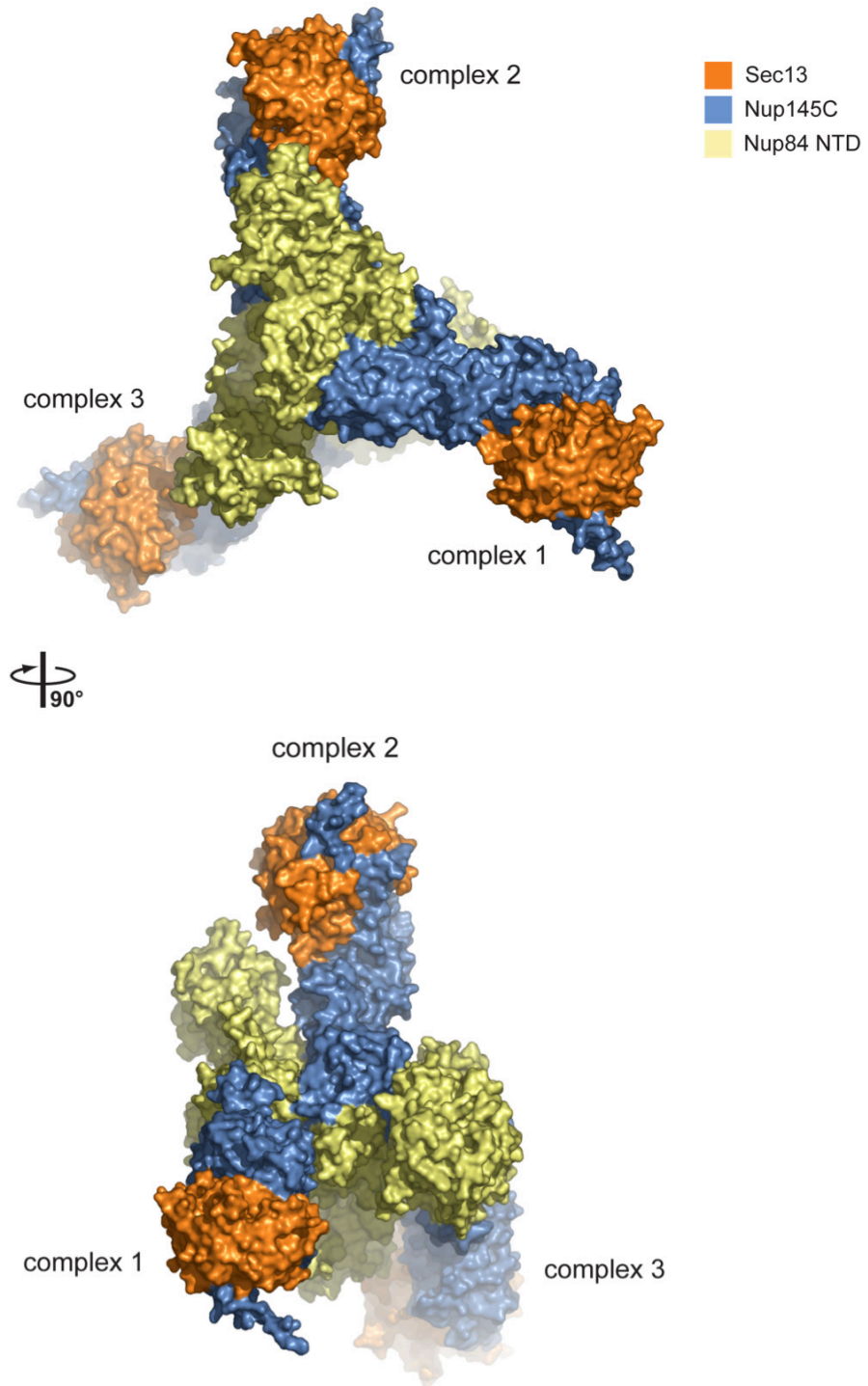


Figure 28: The asymmetric unit of the Sec13•Nup145•Nup84 NTD crystals.

Three copies of the Sec13•Nup145C•Nup84 NTD complex are arranged in a tail-to-tail fashion within the asymmetric unit of the crystals. A 90° rotation of the front view is shown on the right.

three complexes interact with each other in a tail-to-tail fashion and are related by a pseudo 3_2 -screw axis (Figure 28).

4.4. Model Building and Refinement

The previously determined structure of the Sec13•Nup145C hetero-dimer (PDB ID code 3BG1) (Hsia et al., 2007) was docked into the electron density and an initial model for Nup84 NTD was built *de-novo*. Iterative model building and refinement yielded a structure to a final resolution of 3.2 Å with an R_{cryst} of 23.4 % and an R_{free} of 27.3 %. Non-crystallographic symmetry (NCS) restraints were applied throughout the refinement. The refinement statistics are summarized in Table 1.

No electron density was observed for the 3 C-terminal residues of Nup145C, the 7 N-terminal residues, 4 C-terminal residues, and residues 158–169 of Sec13, and the 6 N-terminal residues, residues 368–377 and the 18 C-terminal residues of Nup84 NTD. These residues are presumed to be disordered and therefore have been omitted from the final model.

The stereochemical quality of the final model was assessed with the result that there are no residues in the disallowed region, only 1.6 % of residues in the generously allowed region, 79.1 % and 19.3 % of residues in the favored region and additionally allowed region of the Ramachandran plot (Figure 29).

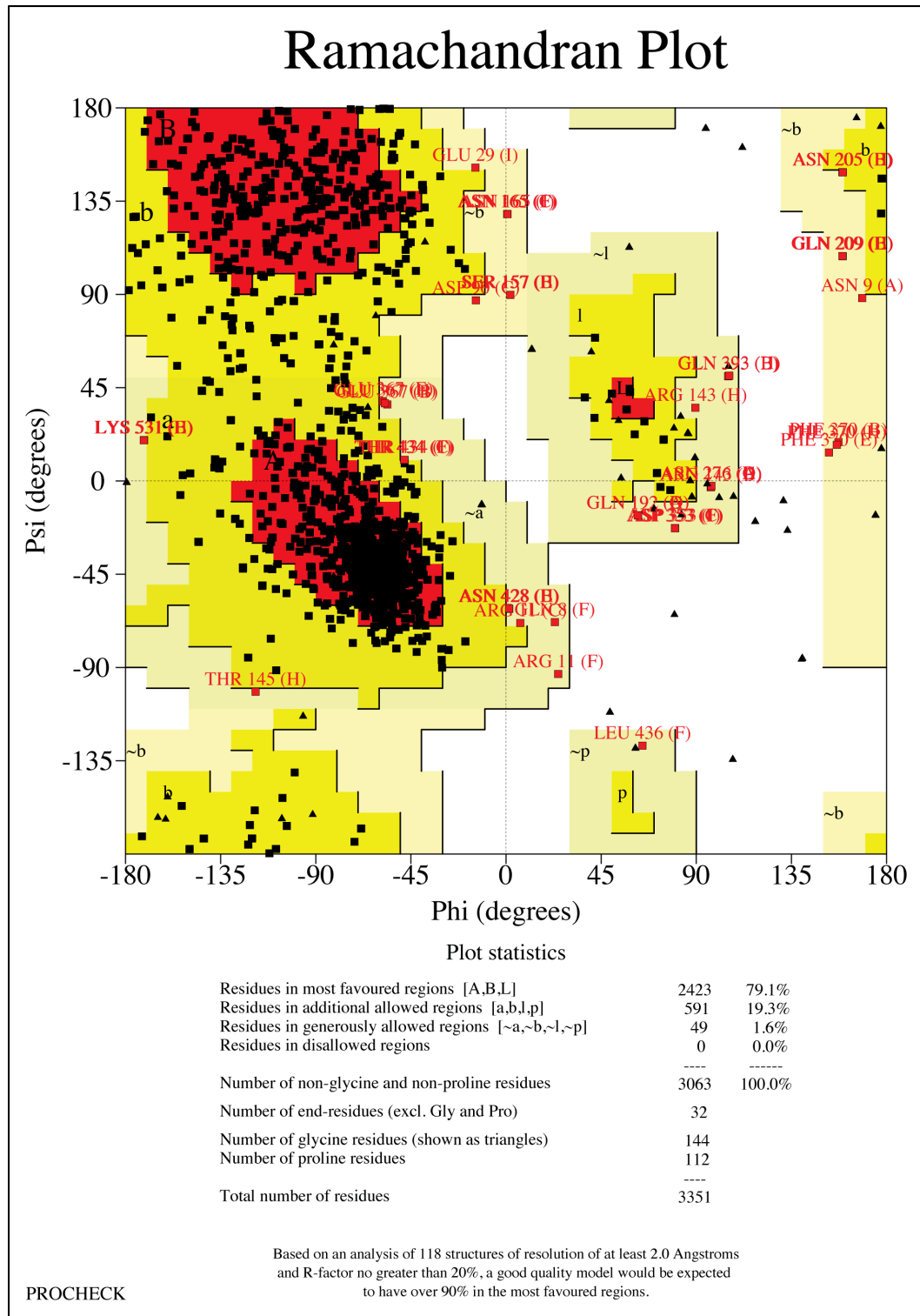


Figure 29: Ramachandran plot of the Sec13•Nup145C•Nup84 NTD structure
The protein backbone angles Phi and Psi of all residues are plotted to assess the stereochemical quality of the structure.

5. Crystal Structure of the Sec13•Nup145C•Nup84 NTD Complex

5.1. Architectural Overview

The hetero-trimeric Sec13•Nup145C•Nup84 NTD complex forms an elongated, Z-shaped assembly of approximately 175 Å length and approximately 50 Å width with the α -helical solenoid domain of Nup145C at its center (Figure 30). At one end of the complex, Nup145C invades the Sec13 β -propeller with its N-terminal

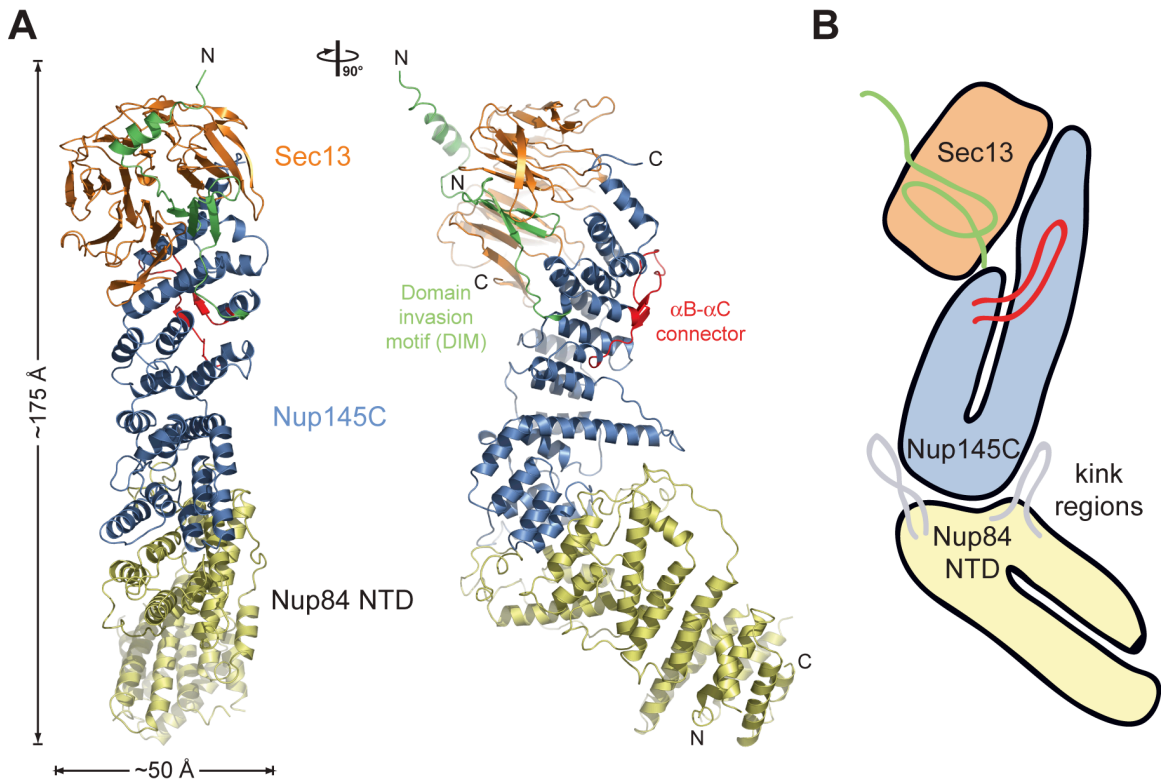


Figure 30: Structure of the *S. cerevisiae* Sec13•Nup145C•Nup84 NTD complex.

A) The structure of Sec13•Nup145C•Nup84 NTD in ribbon representation with Sec13 in orange, Nup145C in blue and Nup84 NTD in yellow. The domain invasion motif (DIM) (green) and the α B- α C connector (red) of Nup145C are indicated. A 90°-rotated view is shown on the right. (B) Schematic representation of the Sec13•Nup145C•Nup84 NTD hetero-trimer.

domain invasion motif (DIM), complementing the six propeller blades of Sec13 with an additional, seventh blade. The overall architecture of the yeast Sec13•Nup145C hetero-dimer is essentially identical to that of the chimeric complex formed by human Sec13 and yeast Nup145C (Hsia et al., 2007). At the other end of the complex, Nup84 NTD is attached to Nup145C. Similar to Nup145C, Nup84 NTD adopts an α -helical solenoid fold that is organized in a U-shaped manner. The α B- α C connector of Nup145C holds the two arms of the U-shape close together. In the Sec13•Nup145C•Nup84 NTD complex, the two solenoid domains of Nup84 and Nup145C interact with each other in a head-to-head orientation via their kink regions. (Figure 30).

5.2. The Nup84 NTD α -Helical Domain

The majority of Nup84 NTD α -helices is arranged in an antiparallel manner, with helices α A- α E forming the descending arm of the U, while helices α L- α Q represent the ascending arm (Figure 31). Interestingly, the compact U-shaped α -helical solenoid domain of Nup84 NTD resembles the topology of the α -helical

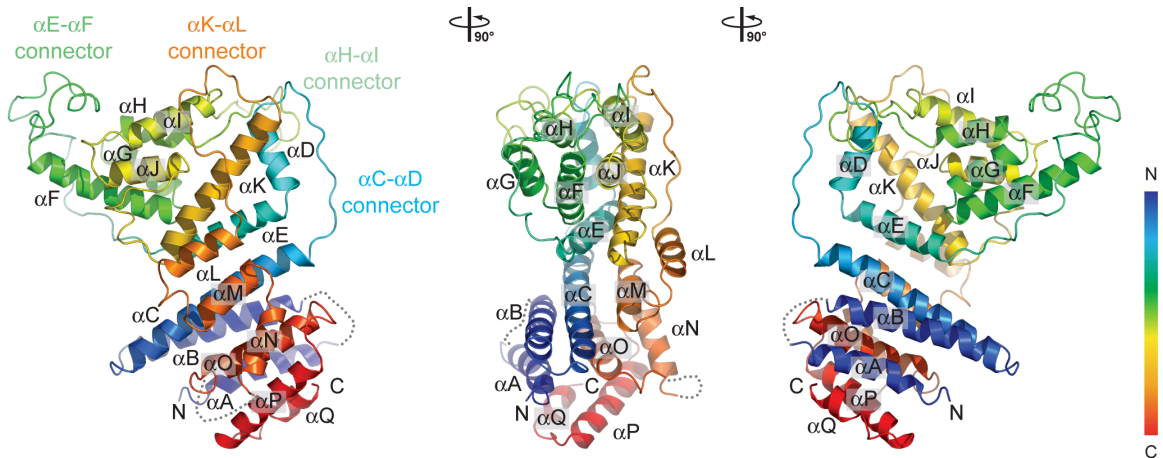


Figure 31: The Nup84 NTD α -helical domain

Ribbon representation of Nup84 NTD is shown in rainbow colors along the polypeptide chain from the N- to the C-terminus. The four loops that participate in the Nup145C•Nup84 NTD interaction are indicated.

solenoid domains of Nup145C and Nup85 (Figure 32) (Debler et al., 2008; Hsia et al., 2007). Nup85 is another nucleoporin of the heptameric Nup84 complex. In further analogy to Nup85 and Nup145C, the intervening helices α F- α K in the kink region of the U-shape form a distinct unit that is connected to the remaining part

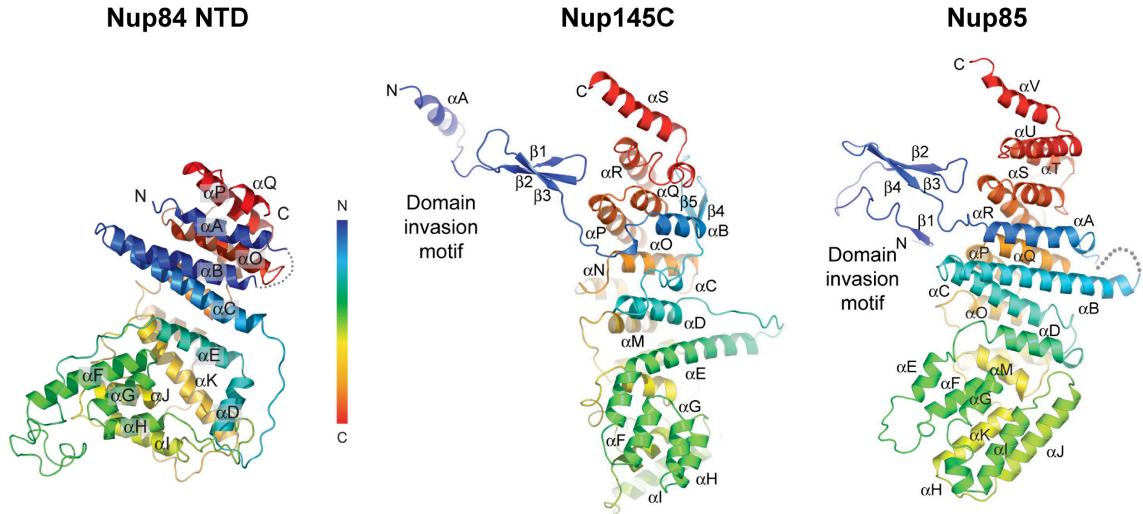


Figure 32: Similar topology of α -helical solenoids

The U-shaped α -helical solenoids of Nup84 NTD, Nup145C, and Nup85 share a similar topology. The ribbon representation is shown in rainbow colors along the polypeptide chain from the N- to the C-terminus

of Nup84 NTD via two long loops, α E- α F and α K- α L, respectively. Nup84 NTD features two other extended connectors, α C- α D and α H- α I. All four connectors are involved in a finger-like binding to Nup145C to various degrees (Figure 30, Figure 31).

5.3. Surface Properties of Nup84 NTD

The Nup84 NTD surface has a striking negative surface potential, similar to other members of the heptamer (Berke et al., 2004; Boehmer et al., 2008; Debler et al., 2008; Hsia et al., 2007) (Figure 33C). Two of the few conserved hydrophobic patches fall into the area that contacts Nup145C, and are located toward the periphery of the extended interface (Figure 33B and C and Figure 16). The

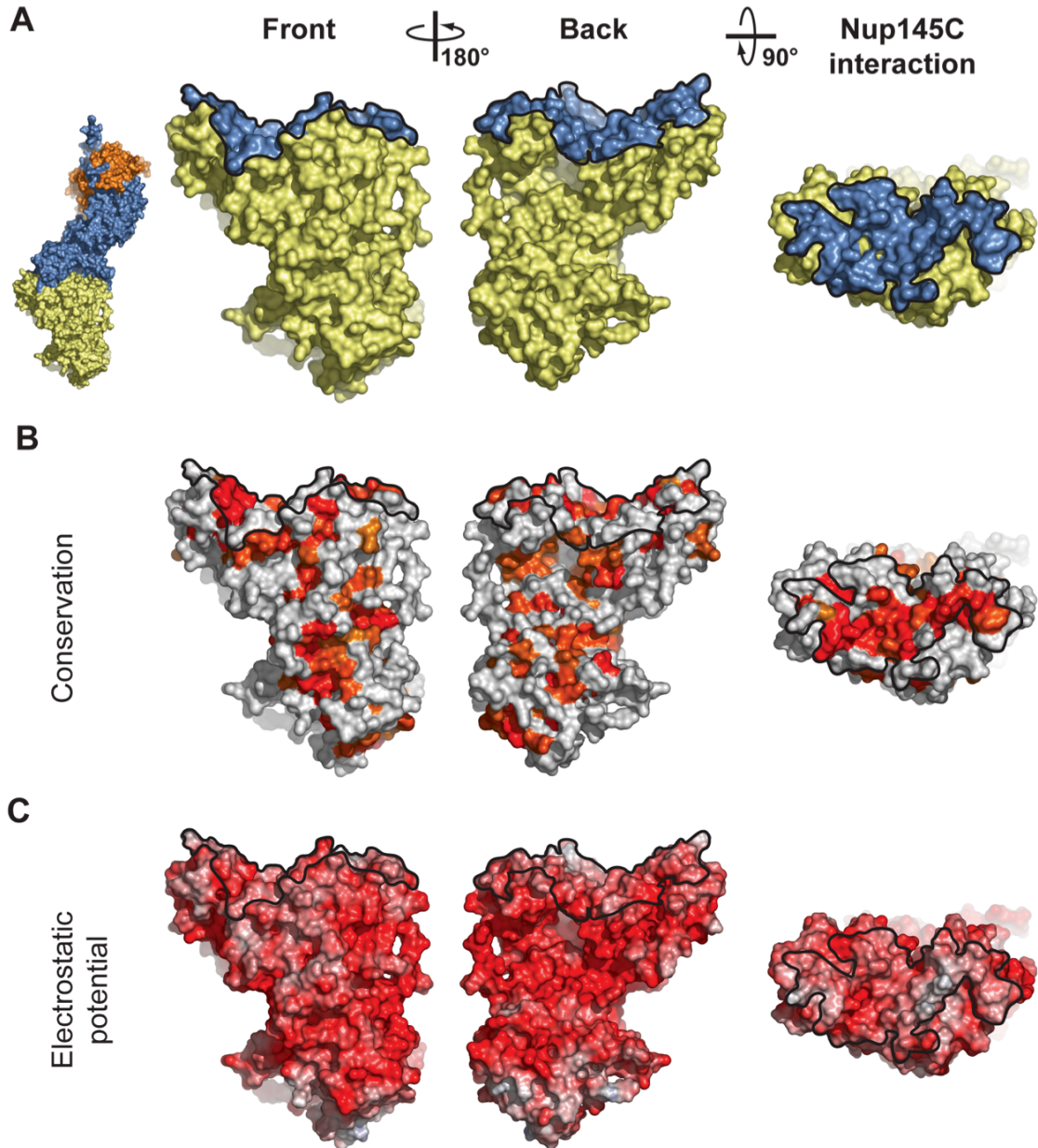


Figure 33: Surface properties of Nup84 NTD.

The surface orientations are identical in all columns. The middle and the right columns show a rotated view with respect to the left column. A black line encircles the Nup145C interaction surface. A) Surface rendition of Nup84 NTD with the Nup145C contact surface colored in blue, while the remaining surface is colored in yellow. As a reference, a surface rendition of the hetero-trimer is shown to the left, colored according to Figure 30. B) The surface representation is colored according to a multispecies sequence alignment, ranging from 60 % similarity (white) to 100 % identity (red) (Figure 16). C) The surface rendition colored according to the electrostatic potential, ranging from -10

$k_B T/e$ (red) to $+10 k_B T/e$ (blue). Note the two conserved hydrophobic patches located toward the periphery of the extended Nup145C-interacting surface.

Nup145C binding area of Nup84 NTD is the largest contiguous conserved region on the Nup84 NTD surface, consistent with its role in Nup145C binding (Figure 33B). Various smaller conserved patches are distributed over the entire Nup84 NTD surface.

5.4. The Nup145C•Nup84 NTD Interface

Nup84 NTD binds to Nup145C and protrudes at an angle of $\sim 40^\circ$ with respect to the long axis of the Sec13•Nup145C complex. The Nup84 NTD and the Sec13•Nup145C nucleoporin pair associate with each other via the kink regions of their U-shaped solenoid domains (Figure 30, Figure 34). The interaction is primarily mediated by a hydrophobic patch that is formed by helices αH and αI of Nup84. The two helices bind into a surface groove on Nup145C that is generated by helices αG , αH , αI , and αJ , burying approximately $1,400 \text{ \AA}^2$ of surface area. This core interface is augmented by four Nup84 NTD loops, with major contributions from the αE - αF and αH - αI and minor contributions from the αC - αD and αK - αL connectors, burying an additional $1,300 \text{ \AA}^2$ of surface area. While the αH - αI loop contacts the long bent helix αE of Nup145C, the αE - αF loop folds into a compact coil structure that contacts the side of the Nup145C kink region (Figure 34). In total, $2,700 \text{ \AA}^2$ of surface area are buried between Nup145C and Nup84 NTD.

Although the four surface loops contribute to the interface, they appear not to be sufficient for the association between the two proteins, since the alteration of the electrostatic character of two key Nup84 NTD residues (I206D and M210D), located in helix αH in the central hydrophobic interface, abolishes the interaction with Nup145C (Figure 16 and Figure 34) (Brohawn et al., 2008). Likewise, a variant of Nup145C in which three residues in helix αH are mutated (V320E,

S323E, and Y324A) fails to interact with Nup84 (Figure 15 and Figure 34) (Brohawn et al., 2008).

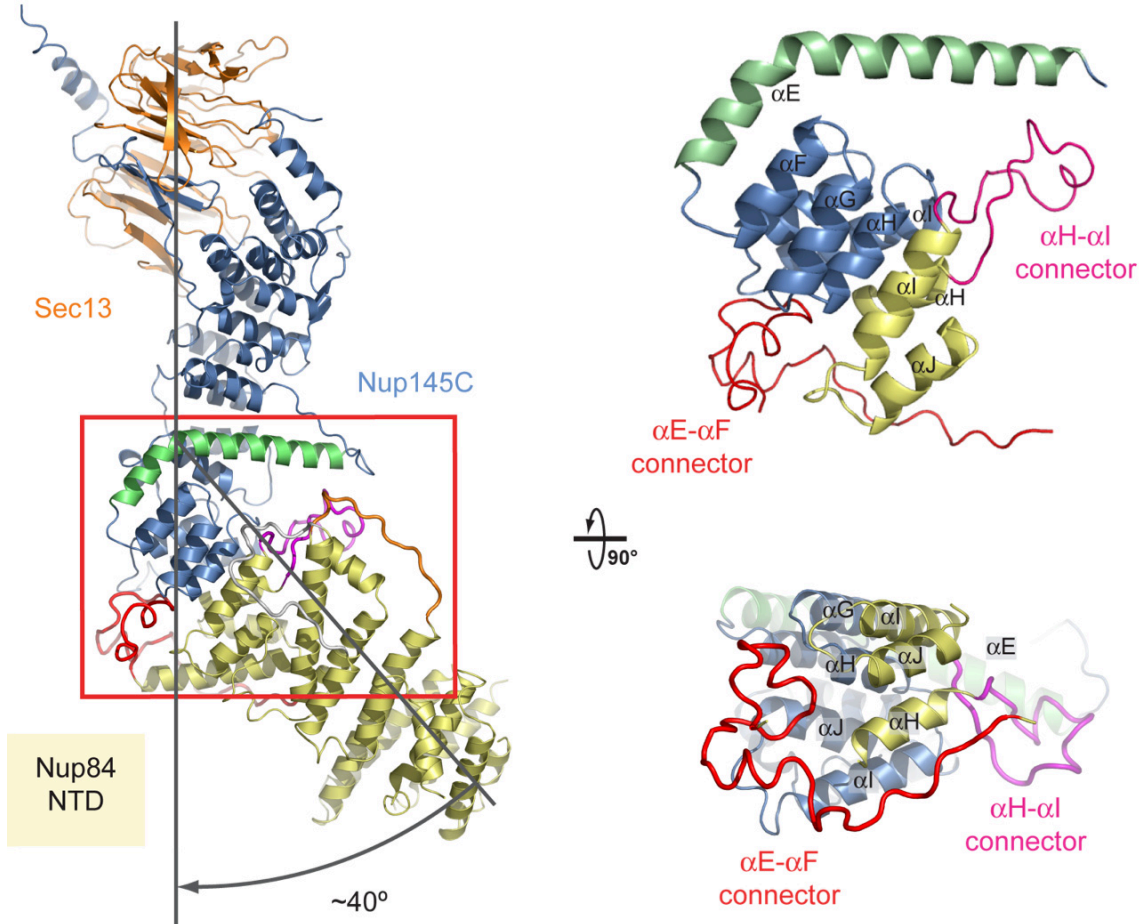


Figure 34: Interaction of Nup84 NTD with Nup145C.

The Sec13•Nup145C•Nup84 NTD hetero-trimer is shown in ribbon representation, colored according to Figure 30. The kink regions of the two solenoids interact in a head-to-head fashion. Nup84 NTD protrudes with an approximate 40° angle from the Nup145C U-shaped solenoid. The inset marks the Nup145C•Nup84 interface that is illustrated in detail in the middle. A rotation of 90° of the enlarged inset is shown on the right. For Nup145C, the α -helical solenoid subdomain (blue) and helix α E (green) are indicated. For Nup84, the interface helices (yellow), as well as the long α E- α F (red) and α H- α I (magenta) connectors that mediate the interaction with Nup145C are indicated.

6. Docking of the Crystal Structure into a Three-Dimensional Electron Microscopy Reconstruction of the Nup84 Complex

The newly available structure allowed for all components of the heptameric complex to be fitted into the three-dimensional EM envelope. Upon completion of the Sec13•Nup145C•Nup84 NTD complex structure, this structure together with the structure of Nup120 (Seo et al., 2009) were additionally fitted into the EM structure of the whole Nup84 complex (Figure 35). Nup120 can be docked into both conformers and fits well into the larger of the two upper arms, with the β -propeller domain at the end of the arm, and the α -helical domain directed toward the center of the Nup84 complex. The position of the β -propeller coincides with the doughnut-shaped density observed in some single negative-stain projection images (Kampmann and Blobel, 2009). While the overall Z-shape of the Sec13•Nup145C•Nup84 NTD hetero-trimer confirmed the approximate placement of the Sec13•Nup145C pair into the Nup84 complex, it only fits snugly into one of the two determined conformations of the Nup84 complex (Figure 35). The approximate 40° angle by which Nup84 NTD protrudes from Nup145C nicely follows one of the two hinges (hinge 1) in the stem of the Nup84 complex conformation 1.

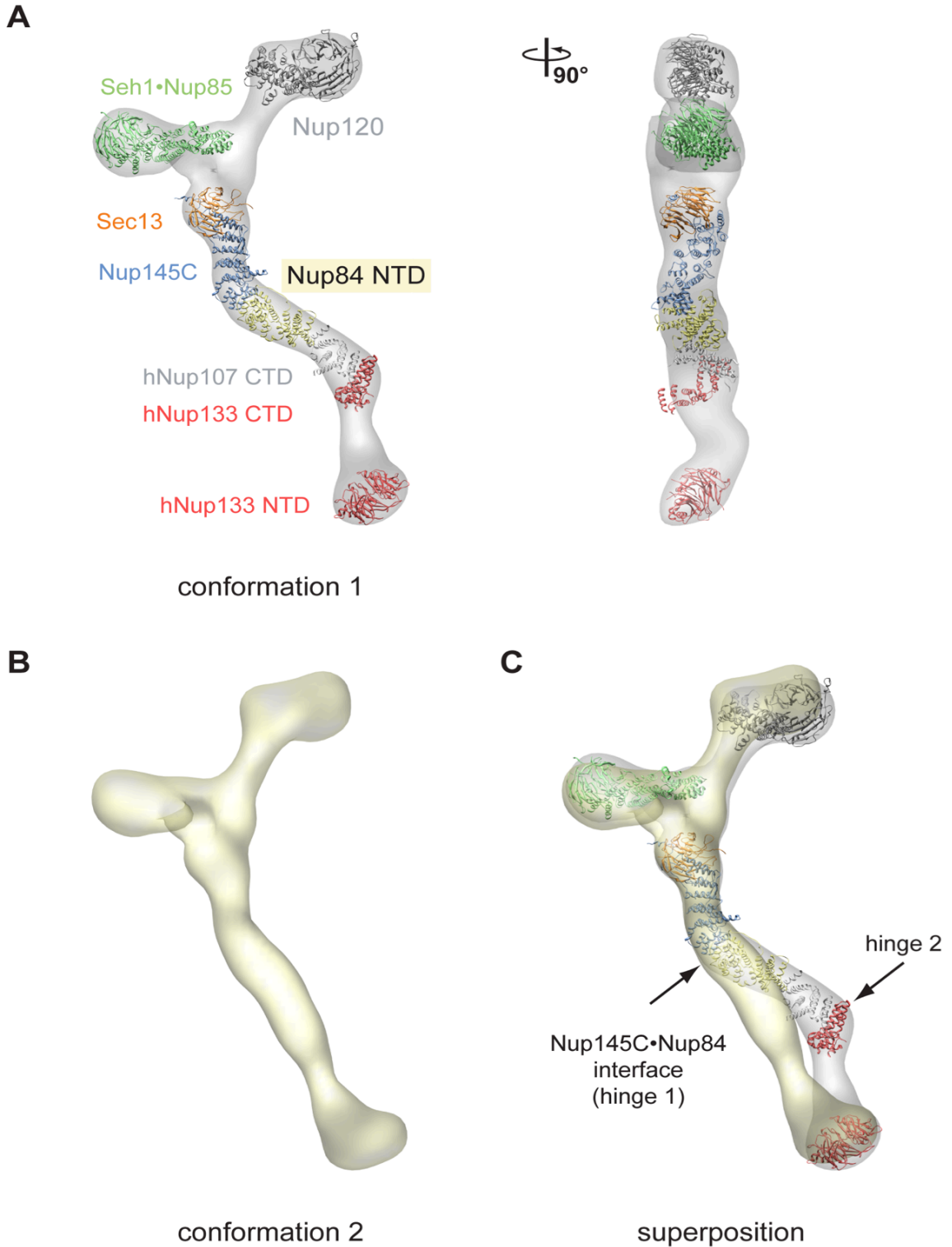


Figure 35: Protein arrangement within the heptameric Nup84 complex.

A) Docking of crystal structures into the EM envelope of the heptameric Nup84 complex. A 90°-rotated view is shown on the right. The approximate 40° angle by which Nup84 NTD protrudes from the Sec13•Nup145C nucleoporin pair nicely follows one of the two

Results

kink regions of the heptamer stem. B) EM envelope of the second reconstructed conformation of the Nup84 complex in which the two hinge regions are completely extended, forming an almost entirely straight stem. C) The superposition of the two determined Nup84 complex conformations. The kink region at the Nup145C•Nup84 interface is indicated and was used for the structural alignment, showing that this interface corresponds to a hinge in the stem of the Nup84 complex.

7. Structural Comparison of the Sec13•Nup145C•Nup84 NTD Complex to the hSec13•Nup145C Complex

The structure of Nup145C had been previously determined in a chimeric complex with human Sec13 (hSec13) (Hsia et al., 2007). This structure revealed the formation of a hetero-octamer by homo-dimerizations of Nup145C and hSec13. In this section, the structure of the trimeric Sec13•Nup145C•Nup84 NTD complex is compared to the structure of the chimeric hSec13•Nup145C complex.

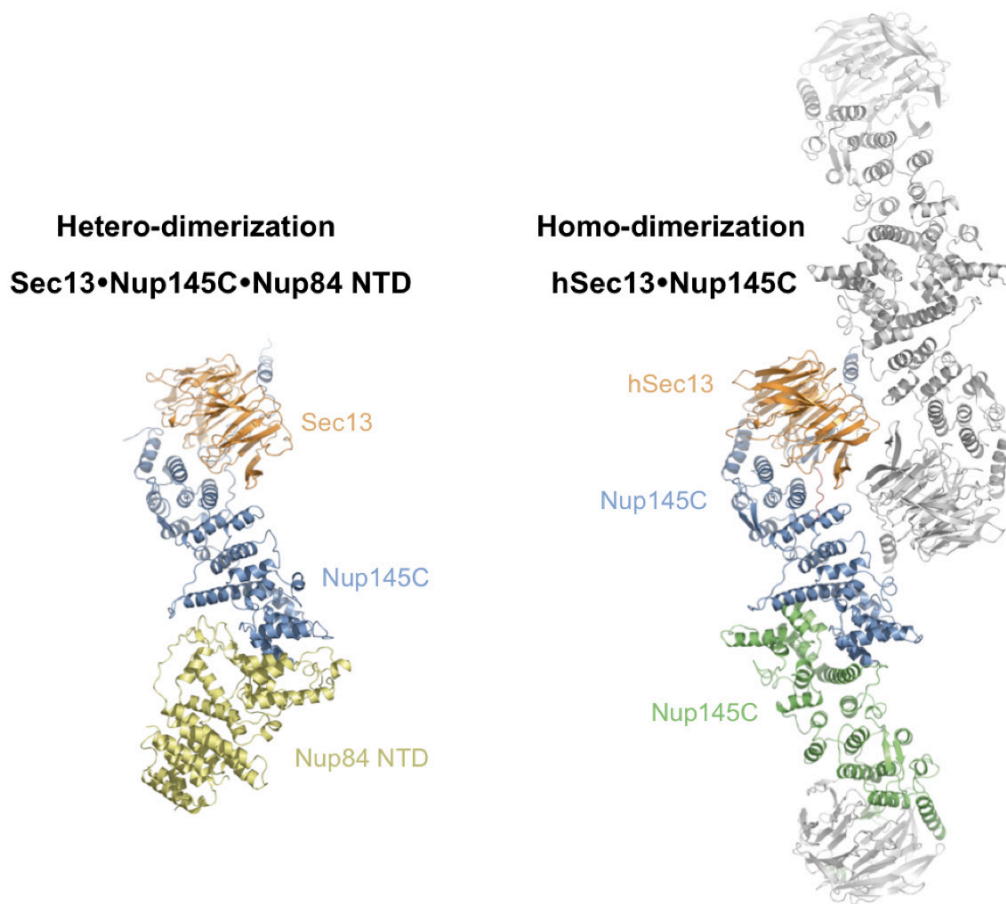


Figure 36: Structural comparison of Sec13•Nup145C•Nup84 NTD and hSec13•Nup145C.

The kink region of Nup145C can engage in a hetero-dimeric interaction with Nup84 NTD in the trimeric Sec13•Nup145C•Nup84 NTD complex or in homo-dimeric interaction by binding to another copy of Nup145C in the chimeric hSec13•Nup145C complex.

Interestingly, this comparison revealed the ability of Nup145C to hetero- or homo-dimerize by interacting with either Nup84 NTD or another copy of Nup145C (Figure 36). Furthermore only slight conformational changes between the two structures could be observed.

7.1. Hetero- and Homo-Dimerization of Nup145C

In absence of Nup84, the Sec13•Nup145C nucleoporin pair can oligomerize into a hetero-octameric bent pole (Figure 37A) (Hsia et al., 2007). This oligomerization is mediated by the homo-dimerization of Nup145C and Sec13, respectively. The homo-dimerization of Nup145C is mediated by a large conserved and hydrophobic surface located in the kink region of the Nup145C solenoid that buries approximately 2,700 Å² of surface area (Figure 37B). The Nup145C dimerization interface features a 2-fold rotational symmetry and is generated by the long bent helix α E and the small subdomain at the base of the U-shaped solenoid (helices α F– α J). Strikingly, Nup145C utilizes the same structural elements for Nup84 NTD binding so that the Nup84 binding site overlaps to a large extent with the Nup145C homo-dimerization region (Figure 37B). While the Nup145C•Nup145C interaction engages both helix α E and the subdomain, the Nup145C•Nup84 interaction primarily occurs via the subdomain. These findings suggest that the Nup145C homo-dimerization and the Nup145C•Nup84 hetero-dimerization are competing binding events.

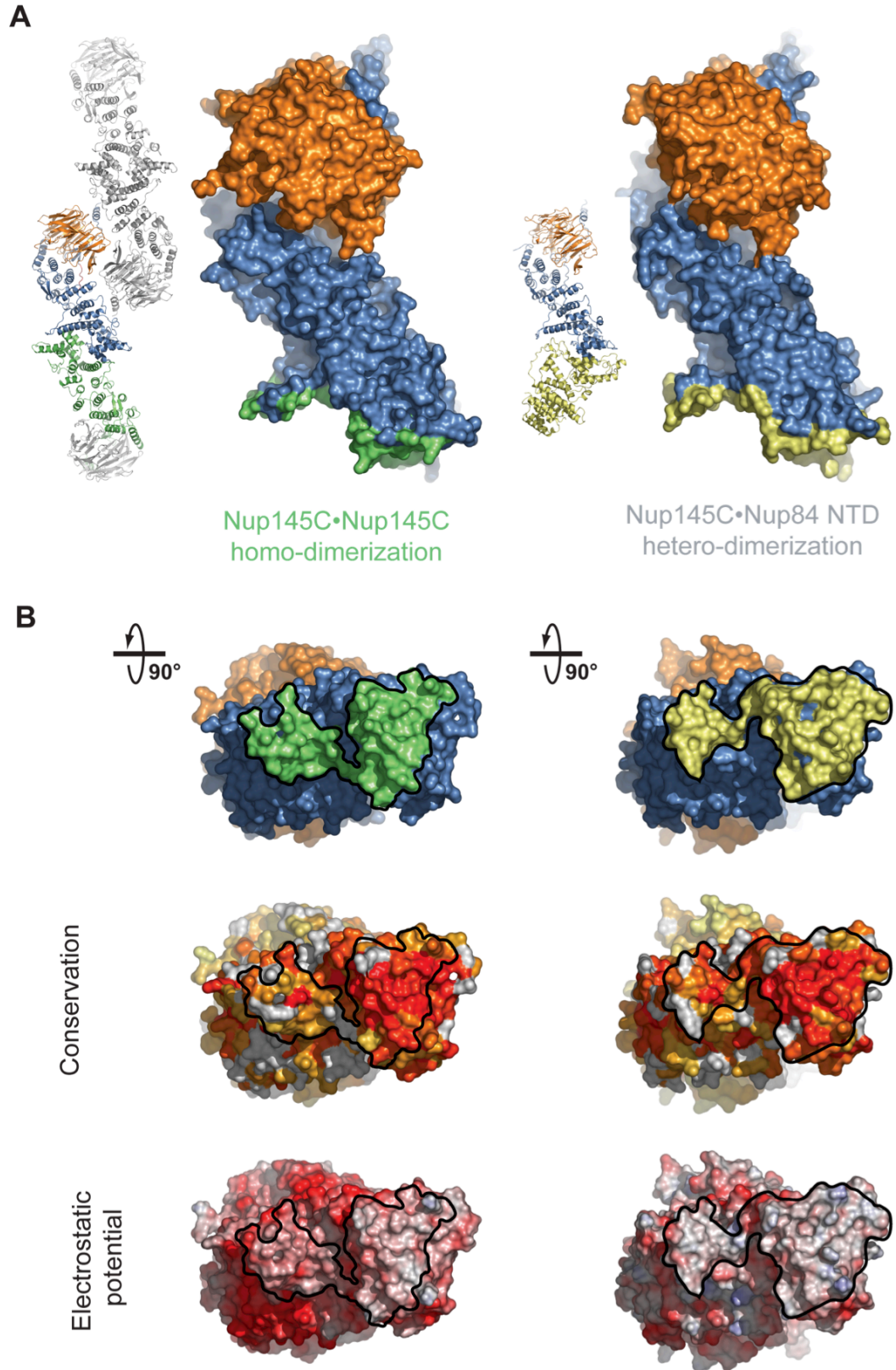


Figure 37: Homo- and hetero-dimerization of Nup145C

A) Surface rendition of the Sec13•Nup145C nucleoporin pair derived from the hSec13•Nup145C hetero-octamer structure (Nup145C•Nup145C homo-dimerization) (Hsia et al., 2007) and the Sec13•Nup145C•Nup84 NTD hetero-trimer structure (Nup145C•Nup84 NTD hetero-dimerization). The Nup145C homo-dimerization and hetero-dimerization surfaces are colored in green and yellow, respectively. The Sec13 and the remaining Nup145C surfaces are colored in orange and blue, respectively. B) 90°-rotated views of the Sec13•Nup145C pair colored according to panel A (top row). A multispecies sequence alignment, ranging from 60 % similarity (white) to 100 % identity (red) (middle row) (Hsia et al., 2007), and the electrostatic potential, from -10 kBT/e (red) to +10 kBT/e (blue) (bottom row) were mapped on the surface of Nup145C. The orientation of all surface representations is identical in each column. As a reference, black lines encircle the Nup145C homo-dimerization and hetero-dimerization surfaces, respectively.

7.2. Conformational Changes

Upon Nup84 binding, slight conformational changes occur in Nup145C (Figure 38). While Sec13 and the upper part of the U-shaped Nup145C solenoid form a rigid unit that is not perturbed by the binding of Nup84, the subdomain at the base of the solenoid undergoes a rigid body rotation by approximately 6° around the kink in the bent helix αE . This rotation translates into a lateral shift of the subdomain residues that participate in the interaction with Nup84 by approximately 2 Å. Overall, the two Sec13•Nup145C structures superimpose with a root-mean square deviation of approximately 1.5 Å over 646 C α atoms.

Results

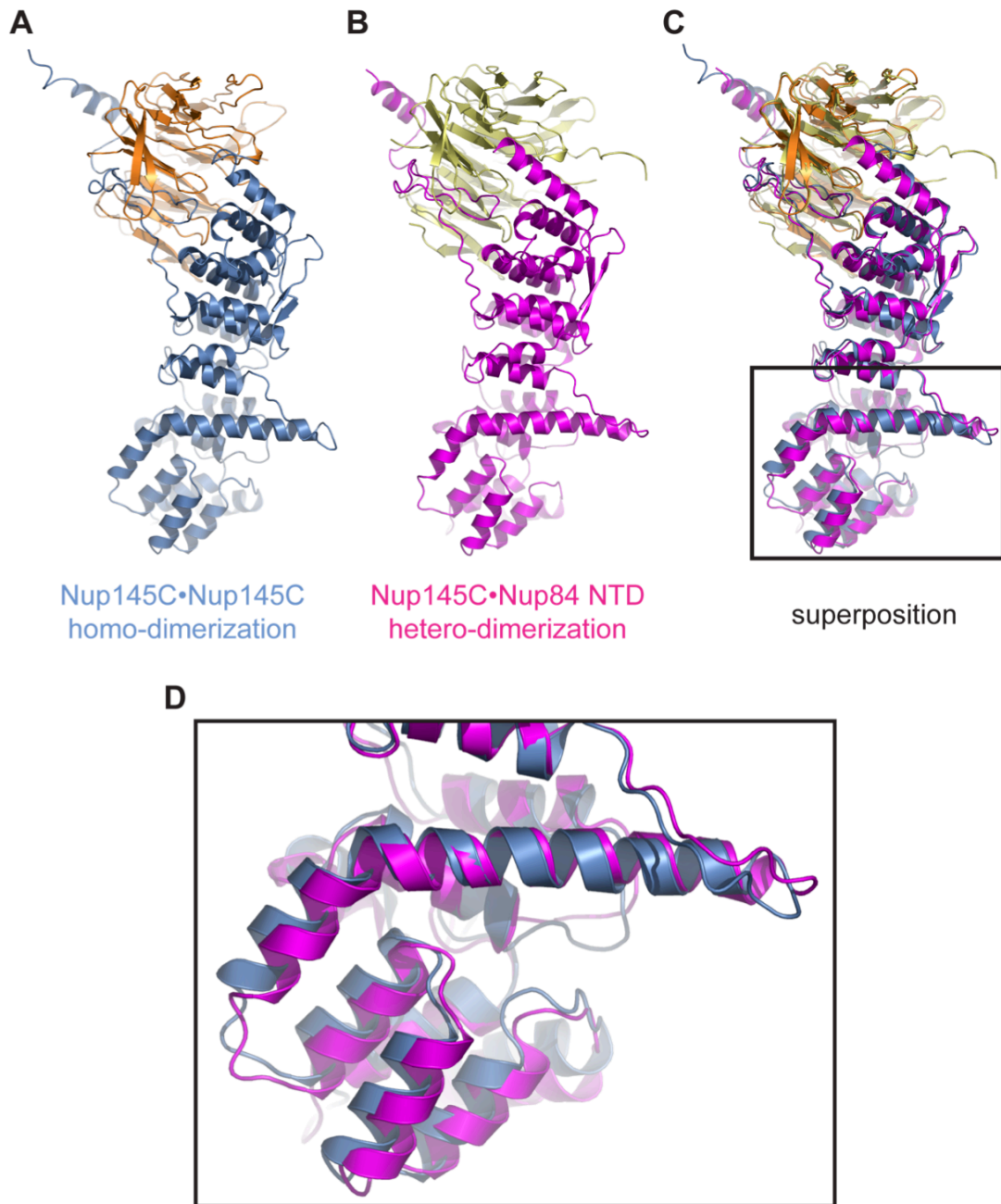


Figure 38: Structural comparison of Nup145C•Nup145C homo-dimers and Nup145C•Nup84 hetero-dimers.

A) The conformation of hSec13•Nup145C in the chimeric hetero-octamer and B) the conformation of Sec13•Nup145C in the Sec13•Nup145C•Nup84 NTD hetero-trimer. C) Superposition of the Sec13•Nup145C conformations in panels A and B. The structural alignment is based on Sec13. The upper arms of the Nup145C solenoid form a relatively rigid unit. D) The inset shows the solenoid subdomain (helices αF – αJ) and the characteristic bent helix αE that undergo conformational changes upon Nup84 NTD binding.

8. Biochemical Characterization of the Sec13•Nup145C•Nup84 NTD Complex

The Sec13•Nup145C nucleoporin complex exists in a dynamic equilibrium between hetero-tetramers and hetero-octamers in solution (Hsia et al., 2007). Moreover, hetero-tetramer and hetero-octamer formations are predominantly the result of Nup145C and Sec13 homo-dimerization, respectively (Hsia et al., 2007). Interestingly, during the preparative scale protein purification of Nup84 NTD a minor protein population was detected, which possibly could be attribute to an oligomeric species. To determine the oligomerization states of Nup84 NTD and the Sec13•Nup145C•Nup84 NTD complex in solution, analytical size-exclusion chromatography, analytical ultracentrifugation, and multiangle light scattering were performed. Both Nup84 NTD and the Sec13•Nup145C•Nup84 NTD complex elute from a gel filtration column as two peaks with apparent molecular weights of 80/190 kDa and 215/560 kDa, respectively (Figure 39A and B). The elution positions at molecular weights higher than calculated are likely due to the elongated shapes of the particles. In fact, size-exclusion chromatography connected in series with multiangle light scattering revealed that the major Nup84 NTD peak corresponds to a monomer (~50 kDa) that exists in equilibrium with a minor population of a dimeric state (~100 kDa) (Figure 39C). Similar results have been obtained for the Sec13•Nup145C•Nup84 NTD complex that exists in equilibrium between the heter-trimer (~126 kDa) and small amounts of its dimer (~249 kDa) (Figure 39D). Consistent with these results, analytical ultracentrifugation corroborated the Nup84 NTD monomer and the Sec13•Nup145C•Nup84 NTD hetero-trimer as the primary species in solution with molecular weights of ~57 kDa and ~134 kDa, respectively (Figure 39E). Due to the small fraction of the dimeric species in solution combined with the low protein concentration dictated by analytical ultracentrifugation, the dimeric species were only barely detectable by this technique. The results of the experiments on the oligomeric states are summarized in Table 2.

Results

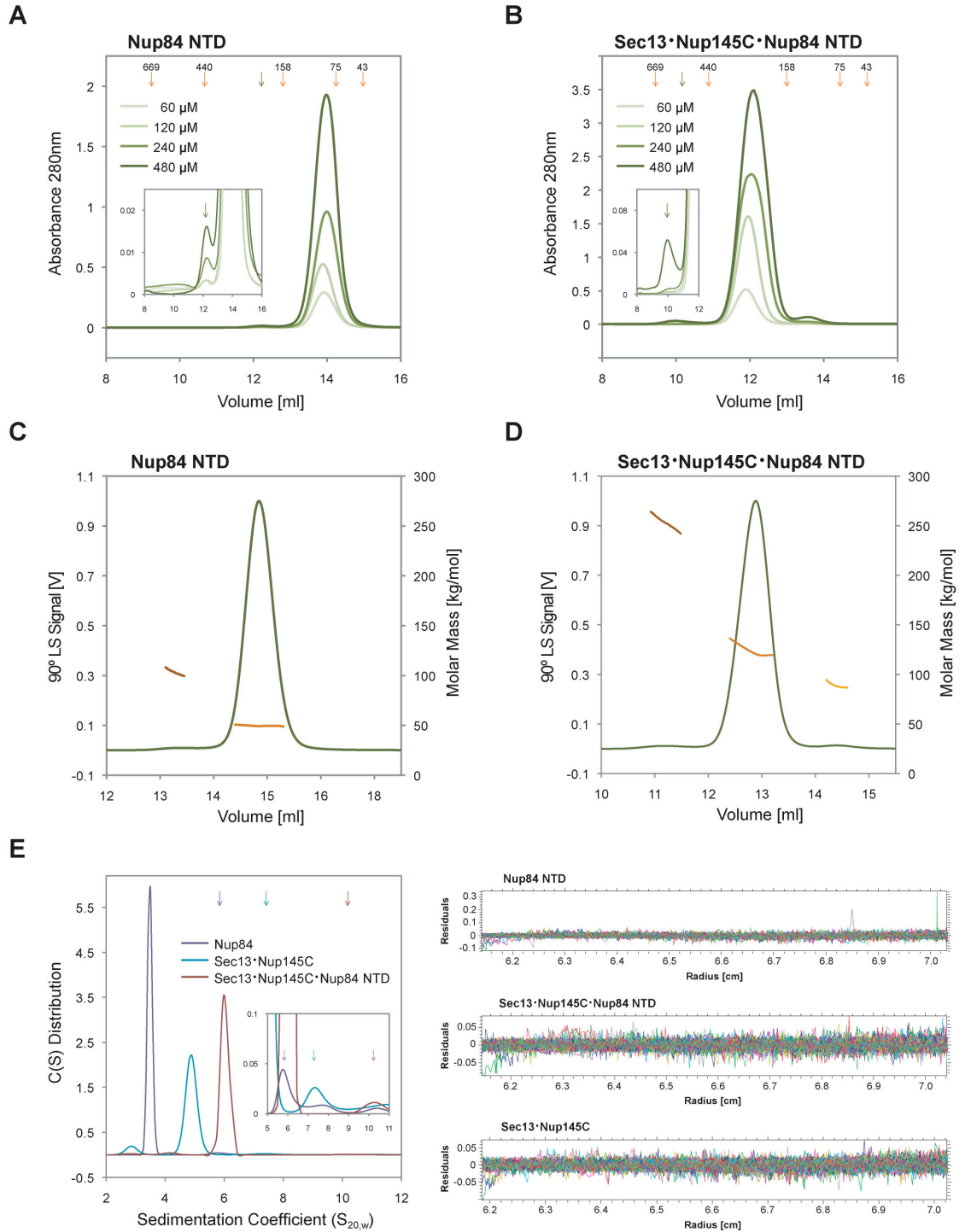


Figure 39: Dynamic behavior of Sec13•Nup145C•Nup84 NTD and Nup84 NTD in solution

Size-exclusion chromatography analysis of A) Nup84 NTD and B) the Sec13•Nup145C•Nup84 NTD complex. All proteins were injected at the indicated concentrations. The elution volumes of molecular weight standards (orange arrows) and

Results

the dimer peak positions (green arrows) are illustrated. The inset displays the magnifications of the dimer peaks. Determination of molecular masses by multiangle light scattering of C) Nup84 NTD and D) the Sec13•Nup145C•Nup84 NTD complex. The 90° light-scattering signal is plotted against the elution volume and is overlaid with the determined molecular masses for the selected peaks. The small peak eluting after the principal peak in B and D corresponds to excess Sec13•Nup145C. Compared to A and B, the peak positions in the light scattering experiments are shifted due to the larger delay volume. E) Sedimentation velocity analysis of the interaction between Sec13•Nup145C and Nup84 NTD. Sedimentation coefficient distributions of Nup84 NTD (purple), of the Sec13•Nup145C nucleoporin pair (blue), and the Sec13•Nup145C•Nup84 NTD complex (magenta). The sedimentation positions of the dimeric species are indicated by arrows in the same color scheme. The residuals of the fits for the three experiments are shown on the right. The molecular masses determined by the various techniques are summarized in Table 2.

Table 2: Biophysical analysis of the oligomerization

| Molecular Weight in kDa | | | | |
|--------------------------------|------------------------|------------------------|-------------------------|-------------------|
| | SEC^a | AUC^b | MALS^c | Calculated |
| Nup84 NTD | | | | |
| Monomer | 80 | 57±2 | 50±0 | 53.4 |
| Dimer | 190 | 120 | 100±3 | 106.8 |
| Concentrations | | | | |
| [μM] | 60-480 | 20 | 120-480 | |
| [mg/ml] | 3-25 | 1 | 6-25 | |
| Sec13•Nup145C•Nup84 NTD | | | | |
| Monomer | 215 | 134±5 | 126±2 | 137.7 |
| Dimer | 560 | 295 | 249±5 | 275.4 |
| Concentrations | | | | |
| [μM] | 60-480 | 6 | 120-480 | |
| [mg/ml] | 8-66 | 1 | 16-66 | |

^aSize-exclusion chromatography. Molecular weight standards have been used to determine the apparent molecular weights.

^bAnalytical ultracentrifugation. Accurate molar masses of the monomers determined by analytical ultracentrifugation are given with their standard deviation. Dimers were barely detectable at the analyzed concentrations.

^cMulti-angle light scattering. Reported errors are standard deviation and result from three independent experiments.

III. Discussion

X-ray crystallography of biological macromolecules has revolutionized our understanding of basic principles in biology. The first protein structure at atomic resolution determined was that of myoglobin 50 years ago (Kendrew et al., 1960). For the first time it was possible to explain the properties of a protein based on its atomic structure. Today, X-ray crystallography has become a broadly-used technique to determine crystal structures of macromolecules. However, the structure determination of large and complex macromolecular assemblies is still an extremely challenging endeavor.

Although the nuclear pore complex (NPC) was discovered more than half a century ago, our knowledge of NPC components in atomic detail has exploded only over the past few years. Numerous crystal structures of single nucleoporins and nucleoporin pairs have been reported. Components of the heptameric Nup84 complex, which is an essential subcomplex of the NPC, have been particularly well characterized by X-ray crystallography. The crystal structure of the heterotrimeric Sec13•Nup145C•Nup84 complex, presented in this thesis, represents the centerpiece of the Nup84 complex and adds tremendously to our structural knowledge and understanding of this key component of the NPC in atomic detail.

1. Structure Determination of the Sec13•Nup145C•Nup84 NTD Complex

Numerous crystallographic obstacles had to be overcome to arrive at the final structure: First, a myriad of conditions was screened for crystal growth and all parameters of the initial crystallization condition had to be varied to obtain crystals that diffracted to a resolution that allowed the visualization of all side chains - and thus the generation of an atomic model - with high confidence. To achieve this goal, the diffraction limit typically has to be higher than 3.5 Å resolution. Hundreds of crystals were screened for diffraction. Most of them reproducibly diffracted to 3.4 Å and only few of them diffracted to the final

resolution of 3.2 Å. The resolution of 3.2 Å combined with the large unit cell dimensions and the high molecular weight content within the asymmetric unit tremendously complicated the phasing of the structure. Non-isomorphism of well diffracting native and heavy atom derivatized protein crystals was a further complicating factor for phasing of the structure. We succeeded in phasing the structure by MIRAS of datasets acquired from native, heavy metal-derivatized, and seleno-L-methionine-labeled protein crystals. An initial experimental electron density map was obtained that could readily be interpreted in terms of the location of Sec13, Nup145C, and Nup84 NTD. Over the course of model building and refinement, the electron density map significantly improved and allowed the unambiguous sequence assignment of the complete crystallized Nup84 fragment. The structure was refined to an R_{work} and R_{free} of 23.4 and 27.3 %, respectively, which represents substantially lower – and therefore, better – R-factors than what are generally expected for structures of comparable resolution. The final structure shows excellent stereochemistry with all residues either in favored, allowed, or generously allowed regions of the Ramachandran plot. It is noteworthy that only a small fraction of all structures deposited in the protein data bank (PDB) are larger than 400 kDa.

2. Structural Analysis of the Sec13•Nup145C•Nup84 NTD Complex

The Sec13•Nup145C•Nup84 complex structure, for the first time, captured the association of three nucleoporins. In the hetero-trimeric complex, Sec13 and Nup145C closely resemble their structures in the previously determined chimeric hSec13•Nup145C complex and follow fold principles that seem evolutionarily conserved in the Nup84 complex and the COPII complex. Specifically, a six-bladed β -propeller, which is invaded by a seventh blade provided by a small domain preceding the U-shaped α -helical solenoid domain, was also observed in the crystal structures of Sec13•Nup145, Seh1•Nup85, and Sec13•Sec31 (Debler et al., 2008; Fath et al., 2007; Hsia et al., 2007). This fold principle has never

been described for other proteins and seems to be unique for proteins of membrane-coating complexes.

The structure of Nup84 NTD revealed an α -helical domain folding into a U-shape with a similar arrangement of α -helices to that found for Nup85 and Sec31 (Debler et al., 2008; Fath et al., 2007). This observation further strengthens the hypothesis of a common progenitor of the Nup84 complex and the COPII complex.

Nup84 NTD binding to the Sec13•Nup145C nucleoporin pair is achieved by the head-to-head interaction of the two kink regions of the U-shaped solenoids of Nup145C and Nup84 NTD. Interestingly, there are only two smaller hydrophobic patches in the Nup145C binding surface of Nup84 NTD, whereas in Nup145C, the entire binding surface is predominantly hydrophobic. The helices α G- α J of Nup145C form two ideal binding grooves for the hydrophobic helices α H and α I of Nup84 NTD. In combination with the four loops of Nup84 a strong binding affinity is achieved.

Analysis of the electrostatic potential revealed a striking negative surface charge for Nup84 NTD and a predominantly negative charge for Sec13•Nup145C. Notably, negative surface charges have also been reported for other members of the Nup84 complex such as Nup120 (Seo et al., 2009) and Seh1•Nup85 (Debler et al., 2008). Interestingly, the cytoplasmic domains of POM152 and POM34, two of the three integral pore membrane proteins, have isoelectric points higher than 10, which suggests a positive surface charge of these proteins. Hence, they would be prime candidates for connecting the Nup84 complexes to their observed location close to the pore membrane domain of the nuclear envelope. A position close to the membrane would be a prerequisite for the Nup84 complex to act as a membrane coating module within the NPC. Similarly, in the COPII complex, the membrane-coating proteins are not bound directly to the membrane but linked by the membrane bound protein Sar1•GTP (Stagg et al., 2007).

3. Docking of Crystal Structures into Low-Resolution EM-Reconstructions – A Paradigm for the Structural Investigation of the NPC

Two-dimensional negative-stain electron microscopy on the Nup84 complex assembled from recombinantly expressed proteins revealed an approximately 400-Å-long Y-shaped complex and established the relative position of its subunits (Lutzmann et al., 2002). The seven nucleoporins are approximately arranged in a linear fashion with Nup133 and Nup84 at the base, the Sec13•Nup145C pair in the center, followed by Nup120 and the Seh1•Nup85 pair at the upper arms of the Y-shape (Lutzmann et al., 2002). Optimization of the purification protocol yielded a pure Nup84 complex that allowed negative-stain three-dimensional EM (Kampmann and Blobel, 2009). This analysis identified two conformations of the Nup84 complex, which differ in two distinct hinge regions at which the Nup84 complex suggests great flexibility. In the first conformation, both hinge regions are kinked whereas they are completely extended in the second conformation. Both conformations allowed for the docking of the atomic structures of hNup133 NTD (Berke et al., 2004), hSec13•Nup145C (Hsia et al., 2007), and Seh1•Nup85 (Debler et al., 2008) into the EM structure. The crystal structure of hNup107 CTD•hNup133 CTD (Boehmer et al., 2008) fitted only one of the two Nup84 complex conformations (Kampmann and Blobel, 2009).

The crystal structure of Nup120 (Seo et al., 2009) and Sec13•Nup145C•Nup84 NTD were subsequently docked into the EM structure. Nup120 could be fitted into both conformations of the Nup84 complex, while Sec13•Nup145C•Nup84 NTD only fit into the kinked conformation. The structural characterization of the entire Nup84 complex is now almost completed by docking of these two large crystal structures into the EM structure of the entire subcomplex. Altogether, more than 425 kDa of protein mass could be docked into the Nup84 complex, which accounts to almost 75 % of the total mass of 575 kDa (Figure 40). However, structural information of nucleoporin portions that connect the two

upper arms to the stem of the Y-shape as well as sections in the base of the Nup84 complex are still missing. Specifically, structures depicting the connection of the Nup133 NTD with Nup133 CTD and Nup84 NTD with hNup107 CTD, the human Nup84 homolog, remain to be determined. Notably, the three docked crystal structures at the base of the Nup84 complex are of human origin and the discrepancy between species may cause an imperfect fit of the human structures to the EM structure of the yeast Nup84 complex. In particular, the fit of the hNup133 CTD crystal structure into the EM envelope is obviously not ideal. Hence, further studies to determine the atomic structures of the remaining yeast nucleoporin fragments would be valuable for a completion of the structural investigation of the yeast Nup84 complex. In general, the current resolution of ~30 Å allows only approximate fitting into the experimentally determined location within the Nup84 complex. Therefore, higher resolution of the EM structure would allow an improved fitting of the crystal structures with regard to position and orientation of the nucleoporins within the Nup84 complex.

It is important to be mentioned that although the Nup84 complex has been assumed to constitute a rigid bona fide building block of the NPC the exact structure of the Nup84 complex in the context of the NPC is presently unknown. In EM studies, the Nup84 complex has been observed repeatedly as a linearly arranged complex in form of a Y-shape. However, this observation was made for the Nup84 complex in isolation. The low concentrations of detergent in combination with high salt concentrations that were used to extract the Nup84 complex out of the NPC are not physiological and may have dramatically changed the structure and organization of the Nup84 complex. During the examination by EM the Nup84 complex was placed on a hydrophobic grid, which may also have altered the conformation. Therefore, it is not foreseeable if the observed structure of the Nup84 complex is physiologically relevant and if the two conformations represent different assembly states *in vivo*. It is conceivable that the conformation of the Nup84 complex is affected considerably by the additional nucleoporins in the assembled NPC. These neighboring nucleoporins may even alter the interactions between the Nup84 complex components and

Discussion

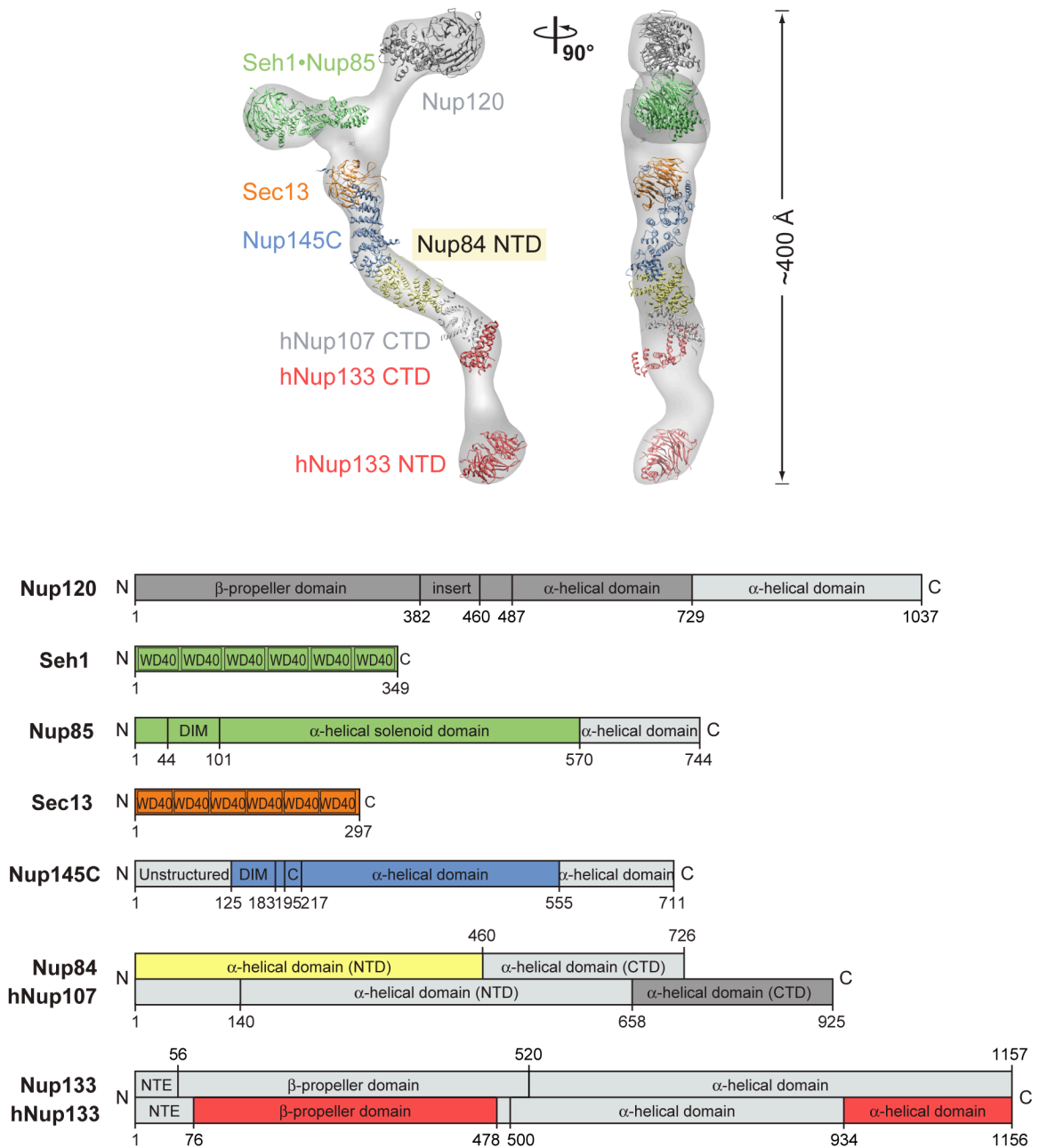


Figure 40: Structural investigation of the Nup84 complex

The upper panel illustrates all available crystal structures of Nup84 complex subunits docked into the EM structure of the entire yeast Nup84 complex. In the lower panel the domain structures of all subunits are depicted. The crystallized fragments are shaded in the same colors used for the representations of the crystal structures in the upper panel. Regions with boxes in light grey represent fragments for which no structural information is available. Note, hNup107 is the human homolog of Nup84 and so far, no structural information is known for the yeast Nup133.

lead to markedly different associations than those observed in the isolated Nup84 complex and its subunits.

However, at present the examination of the Nup84 complex structure constitutes a paradigm for the determination of the entire NPC by this piece-by-piece approach.

4. Flexibility of Nucleoporins, Nucleoporin Subcomplexes, and the NPC

According to the EM structure of the entire Nup84 complex, Nup84 NTD binds to Nup145C in a region where the Nup84 complex shows great flexibility implying that structural changes within the trimeric Sec13•Nup145C•Nup84 NTD complex may occur. The comparison with the second conformation, in which the stem of the Nup84 complex is almost completely straight, illustrates that an approximate 40° rotation of Nup84 in the Nup145C•Nup84 NTD interface region would be required to transform the kinked conformation into the extended conformation. (Figure 41A). In one scenario, the subdomain at the base of the Nup145C solenoid may rotate as a rigid body together with Nup84 NTD, leaving the core of their interface intact. The long bent helix αE of Nup145C could act as a spring to allow such a rigid body rotation (Figure 34). Slight conformational changes occurring in the base of the Nup145C domain have been observed upon binding of Nup84 NTD, which was visualized by superimposing the structures of hSec13•Nup145C and Sec13•Nup145C of the trimeric complex (Figure 38). Alternatively, the different conformations may be achieved by substantial structural changes or rearrangements at the Nup145C•Nup84 NTD interface. This seems reasonable as the interface is partially mediated by flexible loops of Nup84 NTD. However, the three independent Sec13•Nup145C•Nup84 NTD complexes in the asymmetric unit of the crystal do not provide any clues about the molecular basis of the flexibility within the trimeric complex. Therefore, the molecular basis of the flexibility awaits further elucidation. Importantly, it is not clear yet whether the observed Nup84 complex conformations exist *in vivo* and –

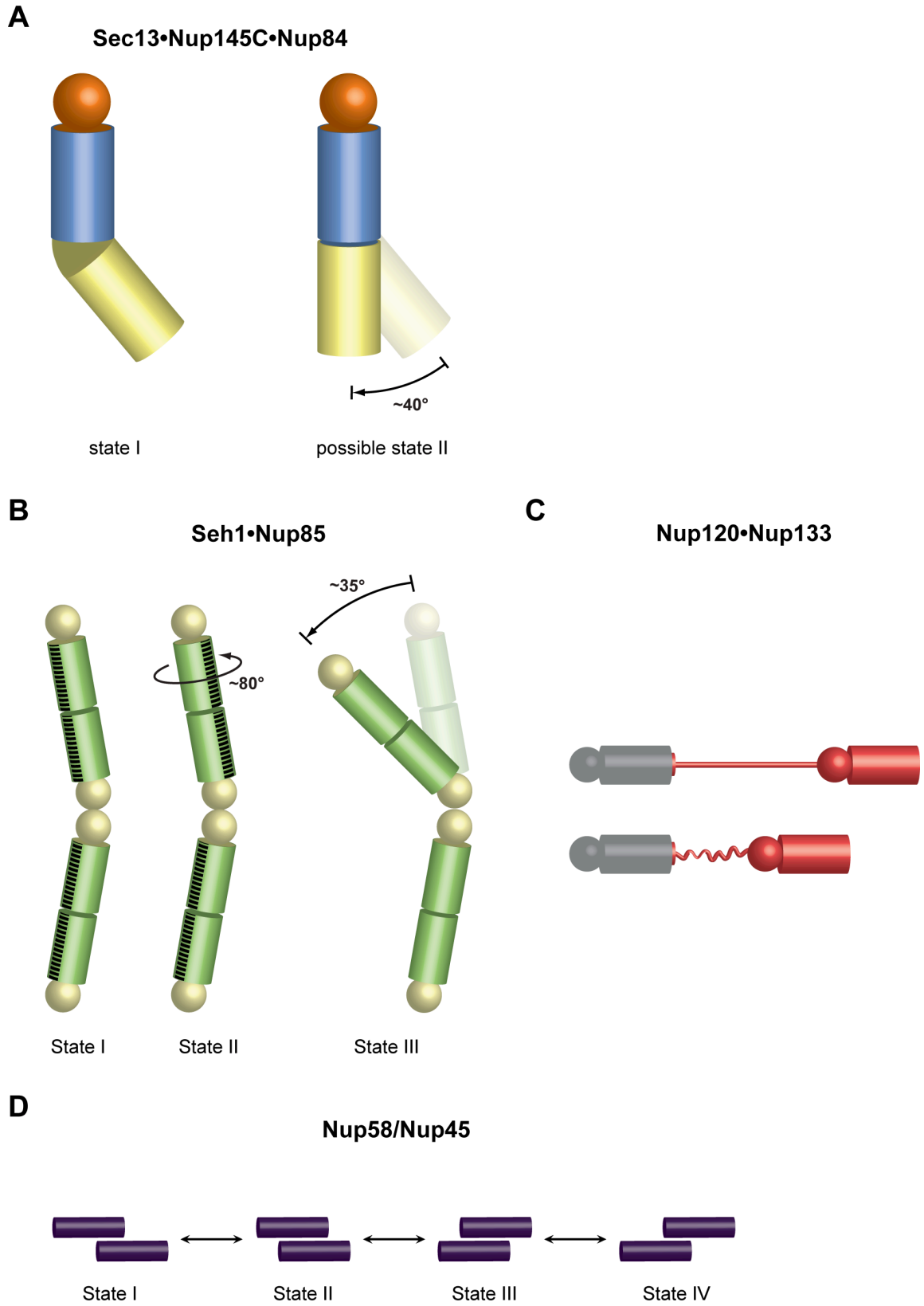


Figure 41: Flexible modules within the NPC

Spheres represent β -propeller domains, while cylinders represent α -helical solenoid domains. A) Sec13•Nup145C•Nup84 (orange, blue, and yellow, respectively) forms a subcomplex that follows a hinge observed in one conformation of the heptameric Nup84 complex as determined by EM (left). On the right, a possible second state is depicted that would correspond to the Nup84 complex conformation with a straight stem observed by EM (Kampmann and Blobel, 2009). B) Crystal structures of the Seh1•Nup85 hetero-octamer (yellow and green, respectively) in three different conformational states revealed a rotation and hinge motion (Debler et al., 2008). C) Nup133 binds to Nup120 via a short N-terminal segment at the end of an unstructured region (Seo et al., 2009). Contraction and expansion of the unstructured region may allow for the flexible tethering of Nup120 and Nup133. D) Four different states of Nup58/Nup45 tetramers have been crystallographically observed (Melčák et al., 2007). The sliding of two Nup58/Nup45 dimers (purple) alters the overall dimensions of the tetramer.

and if so – to what extent the presence of neighboring nucleoporins affect its conformation in the assembled NPC.

Intriguingly, numerous crystal structures of other nucleoporins and subcomplexes also offer insight into the flexibility of NPC components in atomic detail. This is particularly noteworthy, since, until recently, the dynamics of the NPC was only described on a phenomenological level, but mechanistic details remained elusive (Akey, 1995; Beck et al., 2007). Crystal structures of the hetero-octameric Seh1•Nup85 complex revealed three different conformational states, which are related by a simple hinge motion and a rotation, respectively (Figure 41B) (Debler et al., 2008). On the molecular level, these motions are accomplished by slight rearrangements of two neighboring Seh1 β -propellers at the center of the Seh1•Nup85 hetero-octamer. The observed movements provide examples of how individual parts of the NPC may rearrange to facilitate flexibility of the NPC. Furthermore, the biochemically detected interaction of Nup120 with Nup133 is mediated by a flexible, anchor-like element. Since Nup120 and Nup133 are located at opposite ends of the Nup84 complex (Figure 40), this interaction suggests a head-to-tail arrangement of Nup84 complexes to form a ring-like structure. As the attachment site for Nup120 resides at the N-terminal end of a 55-residue unstructured region in Nup133, this flexible segment may allow for a

varying diameter of an eight-membered ring of Nup84 complexes (Figure 41C) (Seo et al., 2009).

Another example for the flexibility of the NPC are the proposed and later observed structural changes of the central channel during nucleocytoplasmic transport (Akey, 1995; Beck et al., 2007). Circumferential sliding of helical elements in the rat nucleoporins Nup58 and Nup45 offers a plausible mechanism for the dilation of the central transport channel in response to cargo translocation (Figure 41E) (Melčák et al., 2007). Nup58 and Nup45 are two alternatively spliced variants of the same gene and the determined structure refers to a part that is common to both proteins (Nup58/Nup45). Two α -helical dimers, folded into hairpins, associate with each other via hydrophobic residues, whereas long hydrophilic residues mediate the interaction between two dimers to form a tetramer. Four different states of Nup58/Nup45 tetramers have been crystallographically observed. The sliding of two Nup58/Nup45 dimers alters the overall dimensions of the tetramer.

During the course of further structural investigations of nucleoporins and NPC subcomplexes, more molecular principles will become apparent that will then help to explain how the flexibility required for the various transport processes of the NPC is achieved.

5. The Sec13•Nup145C•Nup84 Complex in the Context of the Various NPC Models

Over the last years, various alternative approaches have been applied to arrive at three different models describing the structural organization of the NPC:

1) In a “computational model”, a diverse set of biophysical and proteomic data was used as input to obtain a crude blueprint of the entire NPC (Alber et al., 2007b). A general weakness of the computational model refers to a fixed stoichiometry to calculate the probability distribution of the proteins. Importantly, the stoichiometry was determined by semi-quantitative western-blot analysis

(Rout et al., 2000), which only yields approximate copy numbers of the single nucleoporins with relatively high standard deviations. An incorrect copy number for only one nucleoporin could therefore, result in very different distribution probabilities for all nucleoporins and hence, change this model dramatically.

Another critical point is the fact that the interactions within distinct NPC subcomplex are partially well characterized, but very little is known about interactions between different subcomplexes as well as possible oligomerizations of subcomplexes. Therefore it is not comprehensible how the NPC subunits were placed with such a detail into their location within this model

The crystal structure of Sec13•Nup145C•Nup84 NTD conflicts with the proposed arrangement of these proteins in the computational model, because the three proteins would be organized globularly and not linearly, as observed here and as observed in the EM structures (Kampmann and Blobel, 2009; Lutzmann et al., 2002) (Figure 12). In general, the Nup84 complex is depicted in an arrangement that differs from the experimentally observed structure of the Nup84 complex and so far established interactions. This model is, however, consistent with the organization of the Nup84 complex in horizontal rings, which was suggested by the interaction of Nup133 and Nup120 located at opposite ends of the Nup84 complex (Seo et al., 2009).

2) The “lattice model” is based on the homology between nucleoporins of the Nup84 complex and proteins of the COPII complex as well as the structural similarity of the Nup84 complex with the clathrin triskelion (Brohawn et al., 2008). However, the overall dimensions of the symmetric core would sum up to a diameter of only ~600 Å and a height of more than 800 Å if the scaffold is based solely on the oligomerization of eight vertical Nup84 complexes as depicted in the model. Therefore, it would strongly deviate from the dimensions for the yeast NPC observed by EM (1000 Å x 300 Å, respectively) (Figure 11). Furthermore, none of the protein-protein interactions that would connect the Nup84 complexes within one ring or the bridging interactions with proteins between the rings have been established.

However, in principle, the determined structure of the Sec13•Nup145C•Nup84 NTD complex concurs with the arrangement of the Nup84 complex proposed in the “lattice-model”. But due to the low support by other experimental data no further conclusions will be drawn based on this model.

3) In a third model, an architecture of the membrane-coating cylinder of the NPC was proposed that is composed of 32 Nup84 complexes, which form four stacked anti-parallel rings (Debler et al., 2008; Hsia et al., 2007; Seo et al., 2009). This model is based on the formation of hetero-octamers of the hSec13•Nup145C and Seh1•Nup85 complexes, which have been observed in different crystal structures. In detail, the oligomerization of the hSec13•Nup145C hetero-dimer is achieved by homotypic interactions between Nup145C α -helical solenoid domains and homotypic interactions between hSec13 β -propeller domains that ultimately form a hetero-octamer (Figure 6). The Seh1•Nup85 complex forms a similar hetero-octamer (Figure 8). Based on the oligomerizations of Sec13•Nup145C and Seh1•Nup85, a particular oligomeric arrangement of the entire Nup84 complex would result (Figure 7 and Figure 9) Importantly, hetero-octamer formation was also observed biochemically in solution for the chimeric hSec13•Nup145C and the yeast Sec13•Nup145 complex. The two different types of hetero-octameric rods (Sec13•Nup145C and Seh1•Nup85) would connect four adjacent Nup84 complexes. The model is strongly supported by homologies to COPII components and the organization of COPII cages, as well as by symmetry and size considerations derived from EM. Furthermore, the key interactions proposed in this model have been experimentally validated.

At first, the proposed fence-like coat for the nuclear pore membrane seems inconsistent with the Sec13•Nup145•Nup84 NTD structure, because the Nup84 NTD binding site of Nup145C overlaps to a large extent with the Nup145C homo-dimerization region that was identified in the hSec13•Nup145C crystal structure (Figure 6). Hence, the homo-dimerization (Nup145C•Nup145C interaction) and the hetero-dimerization (Nup145C•Nup84 NTD interaction) of Nup145C may not occur simultaneously in the assembled NPC. In the isolated system in solution,

the interaction between Nup84 NTD and Nup145C appears to be stronger than the homo-dimerization of Nup145C, because Nup84 successfully outcompetes the Nup145-homodimerization. Possibly, Nup84 also successfully competes for Nup145C in the assembled NPC with respect to another copy of Nup145C. However, in the cellular context different expression levels of the two proteins and the influence of neighboring proteins could favor the Nup145C homo-dimerization. Furthermore, the observed homotypic interactions Sec13•Sec13, Nup145•Nup145C, Seh1•Seh1, Nup85•Nup85 that are proposed to connect the Nup84 complexes, may not be required to occur at all times to secure a stable coat. Single interactions may be broken transiently without losing structural integrity of the membrane coat.

The fact, that both Nup145C homo-dimerization and hetero-dimerization have been observed crystallographically and biochemically suggest that they may be physiologically relevant interactions. Nup145C may promiscuously interact with both Nup145C and Nup84 *in vivo*. Clearly, further structural studies combined with *in vivo* data are required to resolve these ambiguities. Notably, the binding promiscuity of Nup145C is a complicating factor for *in vivo* analyses, in which the common binding surface is mutated, as it cannot be discerned which of the possible interactions is responsible for the resulting phenotypes.

6. Implications for Promiscuous Binding of Nup145C

The crystal structure of Sec13•Nup145C•Nup84 NTD revealed that Nup145C can engage in two different protein interactions. Possibly, both the homo-dimerization and the hetero-dimerization of Nup145C are physiologically relevant and Nup145C promiscuously interacts with Nup145C and Nup84 NTD *in vivo*. Therefore, it is interesting to contemplate possible implications for the co-existence of both interactions:

1) The Nup145C homo-dimerization in the Sec13•Nup145C hetero-octamer may represent a higher-order structure of the Nup84 complex in a so far unobserved conformation. Accordingly, the Nup84 complex conformation, which has been

observed by EM, and corresponds with the hetero-dimerization of Nup145C, may form a different higher-order structure. The transformation from one assembly state to another could result in substantial structural changes within the NPC. Notably, large structural rearrangements may be necessary during the import of integral membrane proteins to the inner nuclear membrane because the transport complex probably needs to slice through the symmetric core of the NPC during translocation (Figure 2) (King et al., 2006). The NPC could act as a “supramolecular switch” to facilitate transport processes that require considerable rearrangements of the scaffold. The promiscuous binding of Nup145C may contribute to the molecular basis for that.

2) Alternatively, a hetero-octameric Sec13•Nup145C complex could form a pole-like structure within the NPC that is independent from the Nup84 complex. A co-existence of Sec13•Nup145C in 2 independent subcomplexes could be necessary to accommodate the complex curvature of the pore membrane, which is partially convex and concave, compared to the solely convex curvature of membrane vesicles. Somewhat isolated Sec13•Nup145C poles could follow the convex curvature of the pore membrane domain. Additional Nup84 complexes would not even have to be directly connected to the poles and could arrange in rings to stabilize the concave curvature.

3) Possibly, the Nup84 complex does not exist as a heptameric subcomplex within the NPC at all. In such a scenario, the heptameric Nup84 complex could function as a nucleoporin storage complex or it may be required for the assembly of the NPC and/or occur after the disassembly of the NPC during mitosis in higher eukaryotes. Nup84 may bind to the Nup145C homo-dimerization region in a chaperone-like fashion and prevent the oligomerization of the heptamer in the cytoplasm. During the assembly, the protein arrangement may be altered by adjacent nucleoporins. Alternatively, the Nup145C•Nup84 interaction could be required for capping of the proposed coat for the nuclear pore membrane at the peripheral rings (Debler et al., 2008; Hsia et al., 2007; Seo et al., 2009).

Although these implications for the promiscuous binding of Nup145C are speculative, promiscuity has been observed for other nucleoporins and may be a common principle of NPC components. For example, promiscuous binding has been demonstrated to occur in Sec13 (Fath et al., 2007; Hsia et al., 2007). Sec13 is a common component of the NPC and the COPII complex and promiscuously interacts with both Nup145C and Sec31 in the NPC and the COPII, respectively, forming related hetero-octameric complexes (Figure 6 and Figure 10). Furthermore, Sec13 has been demonstrated to replace Seh1 and to interact with Nup85 (Debler et al., 2008). In this case promiscuity may provide redundant interactions in the NPC. Consistently, a deletion mutant of Seh1 in *S. cerevisiae* is viable (Siniosoglou et al., 1996). Nsp1, a protein of the central channel, provides another example for promiscuity within the NPC. It engages into two distinct nucleoporin subcomplexes, the Nsp1•Nup57•Nup49•Nic96 complex and the Nsp1•Nup82•Nup159 complex. A 66-residue fragment of Nsp1 mediates the direct competitive binding of Nup82 and Nup57 (Bailer et al., 2001). Therefore promiscuous binding of nucleoporins may be important for various functional and structural aspects of the NPC.

7. Homotypic Interactions

Intriguingly, it was found that Nup84 NTD and Sec13•Nup145C•Nup84 NTD, like Sec13•Nup145C, exist in a dynamic equilibrium between monomers and oligomers in solution. These homotypic interactions are weak, and yet biochemically detectable. In the evolutionarily related COPII complex, weak interactions between stable Sec13•Sec31 dimers are the basis for the formation of a higher-order structure (Fath et al., 2007). In solution, the human Sec13•Sec31 dimers assemble into closed cages, which were observed by EM. Crystal structures of the yeast Sec13•Sec31 complex could be docked into the EM structure with high confidence. Although the hetero-octameric species of the yeast Sec13•Sec31 complex was not detectable in solution, it forms the basic unit of the outer COPII cage based on the structure fitting. It is not clear if the

weak homotypic interactions observed for Nup84 NTD, Sec13•Nup145C, and Sec13•Nup145C•Nup84 NTD have the same physiological relevance. In principle, the association between these isolated subunits could be enhanced in the cellular context. In particular, the recruitment of the subunits to the NPC may lead to a high local concentration and, thus, promote their assembly. Furthermore, weak interactions within the NPC may be necessary for a rapid dissociation of subunits. At the same time, weak interactions may prevent the premature assembly at inappropriate subcellular locations.

However, it is uncertain if all of these homotypic interactions occur in the cellular context and, if so, when and in which functional background they occur.

IV. Conclusion and Future Directions

Although the NPC was discovered more than half a century ago, our knowledge of NPC components in atomic detail has extended only over the past few years. Recent structural, biochemical, and *in vivo* studies of NPC components, in particular the membrane-coating, heptameric Nup84 complex, have shed light onto the NPC architecture as well as onto its dynamic nature. Furthermore, striking similarities were revealed between the components of the NPC and of coat protein complexes in the endocytic and secretory pathways, supporting their common evolutionary origin in a progenitor protocoatomer.

In an effort to advance our understanding of the NPC, the first atomic structure of a trimeric nucleoporin complex was determined. The crystal structure of the Sec13•Nup145C•Nup84 NTD complex adds tremendously to our structural knowledge of this key component of the NPC in atomic detail. The docking of this trimeric subcomplex together with other subunits into an EM structure of the entire Nup84 complex now provides a nearly complete atomic picture of the Nup84 complex. This piece-by-piece approach should now be extended to the entire NPC. Furthermore, the structural investigation of the Sec13•Nup145C•Nup84 NTD complex offers a molecular basis for the suggested flexibility of the Nup84 complex. Beyond the flexibility within the Nup84 complex, the structure suggests the existence of alternate assembly states of the Nup84 complex subunits. Possibly, these principles are not limited to the Nup84 complex and may extend to other NPC components. It remains to be investigated if different assembly states occur *in vivo* and in what functional context they would appear.

Despite the tremendous recent progress of the structural investigation of NPC components, the molecular architecture of the NPC core remains enigmatic. Due to the high complexity, large dimensions, and the dynamic character, the detailed architectural organization of the NPC core cannot be directly obtained at present by established structural methods such as EM. In the future, the key challenge will be to bridge the resolution gap between high-resolution crystal structures and

low-resolution EM structures of the entire NPC. This will be inevitable to allow the direct docking of the determined crystal structures of NPC components. An *in vitro* assay to assemble a minimal NPC core would possibly provide a specimen for its experimental structure determination by EM to a higher resolution than available at present.

Furthermore, the exact stoichiometry of nucleoporins within the NPC needs to be determined to prevent incorrect crystal structure fitting into EM structures and flawed computational modeling. Several methods have become very quantitative and may be appropriate to determine a more accurate stoichiometry. For example, quantitative mass spectrometry in combination with quantitative immunofluorescence microscopy could be a suitable approach.

To further support the challenging endeavor to determine a high-resolution structure of the NPC, more structural studies of NPC subcomplexes combining X-ray crystallography with EM will be required. The structural analysis of the Nup84 complex has demonstrated that NPC components may engage in different assembly states. It is of great importance to crystallographically capture as many assembly states of nucleoporins and nucleoporin complexes as possible. Ultimately, a combination of the structural snapshots will guide us to a movie that portrays in detail the interconversion of various NPC states.

It becomes clear that only a highly interdisciplinary approach that will also depend on substantial technical advances of the applied methods, can be successful to expand our understanding of the dynamic structure and function of this fundamental transport organelle in four dimensions.

V. Material and Methods

1. Protein Sequence Analyses

To analyze the domain structure of Nup84, secondary structure predictions were performed using the HNN, DPM, MLRC, PHD, and PREDATOR algorithms of the NPS@ Web server (Combet et al., 2000).

Sequence alignments were generated using ClustalX (Barton, 1993; Jeanmougin et al., 1998) and were subsequently colored with Alscript (Barton, 1993) using the Blosum62 weighting algorithm.

2. Molecular Cloning

DNA fragments of *S. cerevisiae* Nup145C, comprising residues 125–555, and full-length *S. cerevisiae* Sec13 were amplified by PCR and cloned into the bicistronic pETDuet-1 expression vector (Novagen) using *Bam*HI/*Not*I and *Nde*I/*Xho*I restriction sites, respectively. The resulting Sec13•Nup145C heterodimer contains untagged Sec13 and a Nup145C fusion protein with an uncleavable N-terminal hexahistidine tag (MGSSHHHHHSQDP), as described (Hsia et al., 2007).

A DNA fragment comprising residues 1–460 of *S. cerevisiae* Nup84 was amplified by PCR and cloned into a pET28a vector (Novagen), modified to contain a PreScission protease cleavable N-terminal hexahistidine tag (Hoelz et al., 2003) using *Nhe*I/*Not*I restriction sites. Protease cleavage of Nup84 NTD leaves a six-residue N-terminal overhang (GPHMAS).

Additional methionines were incorporated into Sec13 to obtain seleno-L-methionine-labeled crystals with increased phasing power. L11, L17, I46, I81, L115, and L222 were mutated to methionine residues by QuikChange Mutagenesis (Stratagene). The selection of mutated residues is partly based on previously designed mutations by (Fath et al., 2007)

3. Protein Expression

The Sec13•Nup145C complex and Nup84 NTD were expressed separately in *E. coli* BL21-CodonPlus (DE3)–RIL cells (Stratagene) after transformation of the according expression construct.

When the cells grown at 37 °C in LB medium reached an OD₆₀₀ of 0.6 – 0.8, the temperature was decreased to 18 °C and the protein expression was induced by the addition of 0.5 mM IPTG. Protein expression was carried out for 16 h.

Seleno-L-methionine-labeled proteins were produced with a methionine pathway inhibition protocol (Doublet, 1997), in which cells were grown at 37 °C in M9 minimal medium (40 mM K₂HPO₄, 20 mM KH₂PO₄, 20 mM NH₄Cl, and 10 mM NaCl) supplemented with 1 mM MgSO₄, 65 µM CaCl₂, 30 µM FeSO₄•7H₂O, 20 mM glucose and 0.5 mg/l thiamine. At an OD₆₀₀ of 0.5, large amounts of the hydrophobic amino acids L-lysine, L-phenylalanine, L-threonine (100 mg/l) and L-isoleucine, L-leucine, L-valine (50 mg/l) were added to inhibit the methionine synthesis pathway and to enforce the incorporation of seleno-L-methionine (50 mg/l) into proteins. 30 min later, protein expression was induced by the addition of 0.5 mM IPTG. Expression of seleno-L-methionine labeled protein was carried out for 16 h at 18 °C.

Cells were harvested by centrifugation for 15 min at 3000 x g, 4 °C, and resuspended in a buffer containing 20 mM Tris-HCl, pH 8.0, 500 mM NaCl, 5 mM β-mercaptoethanol, 0.5 mM PMSF, 2 µM bovine lung aprotinin, and Complete EDTA-free protease inhibitor mixture (Roche). The cells were lysed with a cell disrupter (Avestin), and the lysate was cleared by centrifugation at 35,000 x g and 4 °C for 90 min.

4. Protein Purification

Protein fractions of all purification steps were generally analyzed by SDS-PAGE followed by Coomassie Brilliant Blue staining.

For the purification of Nup84 NTD, the lysate was loaded onto a Ni-NTA agarose column (Qiagen) in an affinity chromatography step and eluted via an imidazole gradient (10–1,000 mM). Protein-containing fractions were pooled and desalted on a HiPrep 26/20 desalting column (GE Healthcare) using a buffer containing 20 mM Tris-HCl, pH 8.0, 100 mM NaCl, and 5 mM β -mercaptoethanol. The protein was then subjected to cleavage with PreScission protease (GE Healthcare) for 12 - 16 h, and rerun over a Ni-NTA column to remove uncleaved hexa-histidine-tagged Nup84 NTD. The flow-through containing the cleaved Nup84 NTD was desalted on a HiPrep 26/20 desalting column (GE Healthcare) using a buffer containing 20 mM Tris-HCl, pH 8.0, 100 mM NaCl, and 5 mM DTT and then loaded onto a MonoQ 5/50 GL column (GE Healthcare) for an anion exchange chromatography step. Elution was achieved via a NaCl gradient (100–600 mM). Fractions containing Nup84 NTD were pooled and concentrated before further purification by size-exclusion chromatography using a 16/60 HiLoad Superdex 200 column (GE Healthcare) and a buffer containing 20 mM Tris-HCl, pH 8.0, 100 mM NaCl, and 5 mM DTT. Fractions containing the pure protein were pooled and concentrated to 40 mg/ml by ultrafiltration. The purified protein was used for crystallization experiments, biochemical experiments, or frozen in liquid nitrogen, and stored at -80 °C.

For the purification of Sec13•Nup145C, affinity chromatography was performed using a Ni-NTA agarose column, which was loaded with the lysate and eluted via an imidazole gradient (10–1,000 mM). Protein-containing fractions were pooled and run over a HiPrep 26/20 desalting column using a buffer containing 20 mM Tris-HCl pH 8.0, 100 mM NaCl, and 5 mM DTT. The protein was further purified by anion exchange chromatography using a MonoQ 5/50 GL column that was eluted via a NaCl gradient (100–600 mM). Size exclusion chromatography was performed with a 16/60 HiLoad Superdex 200 column to finally purify and polish the protein. Fractions containing the pure protein were pooled and concentrated to 40 mg/ml by ultrafiltration. The purified protein was used for crystallization experiments, biochemical experiments, or frozen in liquid nitrogen, and stored at -80 °C.

A schematic representation of the purification protocol for Nup84 NTD and the Sec13•Nup145C complex is illustrated in Figure 42.

The hetero-trimeric Sec13•Nup145C•Nup84 NTD complex was formed by incubation of equimolar amounts (150 μ M) of the Sec13•Nup145C complex and Nup84 NTD for 1 h at 4 °C. The hetero-trimer was further purified by size exclusion chromatography on a 16/60 HiLoad Superdex 200 column in a buffer containing 20 mM Tris-HCl, pH 8.0, 100 mM NaCl, and 5 mM DTT. Fractions containing the hetero-trimer were pooled and concentrated to 40mg/mL by ultrafiltration before diluting to appropriate concentrations for crystallization and biochemical experiments.

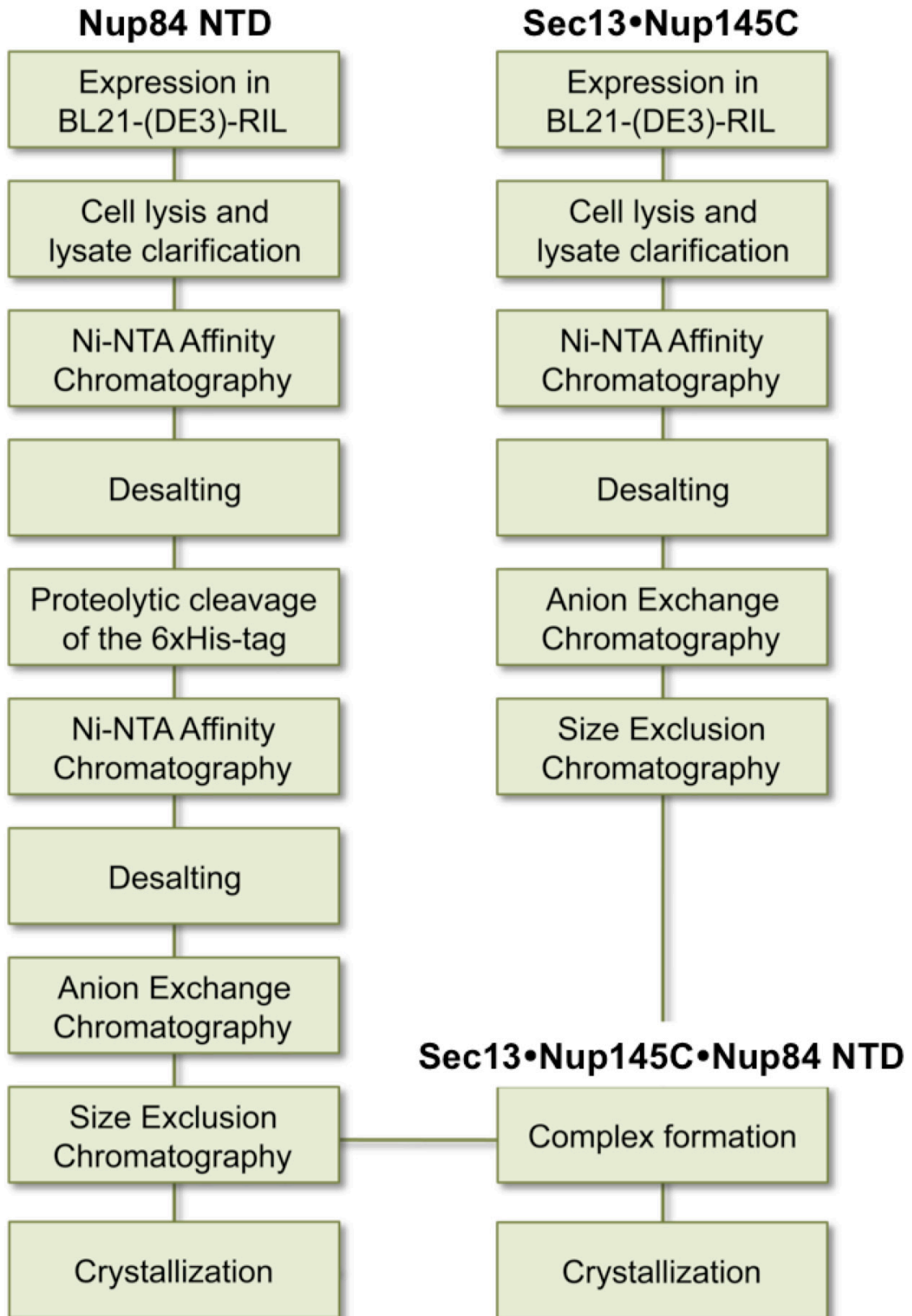


Figure 42: Flow chart of the protein purification procedure

5. Biochemical Analyses of the Sec13•Nup145C•Nup84 NTD Complex

5.1. Analytical Size Exclusion Chromatography

Purified proteins were analyzed on a Superdex 200 10/300 GL column (GE Healthcare) equilibrated with a buffer containing 20 mM Tris-HCl, pH 8.0, 100 mM NaCl, and 5 mM DTT. 50 μ l of protein solutions were injected onto the column at concentrations of 60–480 μ M, and peak fractions were analyzed by SDS-PAGE. The elution volumes of molecular weight standards have been used to determine apparent molecular weights.

5.2. Isothermal Titration Calorimetry

ITC measurements were performed in collaboration with Shaun Bevers at the Biophysics Core Facility at the University of Colorado Denver. Experiments were performed with thoroughly degassed proteins at 25 °C in a buffer containing 20 mM Tris-HCl, pH 8.0, 100 mM NaCl and 1 mM TCEP using a MicroCal VP-ITC calorimeter (Northhamton, MA). Every 180 s, 10 μ L of 200 μ M Nup84 NTD were injected into 1.7 mL of 10 μ M Sec13•Nup145C. The heat generated due to dilution was subtracted for baseline correction. Baseline-corrected data were analyzed with MicroCal ORIGIN Version 7.0 software. All experiments were performed at least twice.

5.3. Analytical Ultracentrifugation

Analytical Ultracentrifugation experiments were done in collaboration with Leslie Eisele at the Wadsworth Center Biochemistry Core Facility. Sedimentation velocity experiments were performed at 20 °C in a Beckman Optima XL-I analytical ultracentrifuge at a rotor speed of 50,000 rpm. Double-sector cells were loaded with 400 μ L protein sample with concentrations of 1.0 mg/mL for Nup84 NTD, 0.7 mg/mL for Sec13•Nup145C, and 0.8 mg/mL for

Sec13•Nup145C•Nup84 NTD in a buffer containing 20 mM Tris, pH 8.0, 100 mM NaCl, and 2.5 mM DTT and 410 μ L reference buffer, respectively. Data were recorded with absorbance detection at wavelength 280 nm. The partial specific volume and the solvent density were calculated using the SEDNTERP program (Philo). The SEDFIT analysis program was used to analyze the absorbance profiles and to calculate the sedimentation coefficient distribution $c(s)$, which was then transformed into a molar mass distribution $c(M)$ (Schuck, 2000).

5.4. Multi-Angle Light Scattering

Purified proteins were characterized by multiangle light scattering (MALS) following size-exclusion chromatography (Wyatt, 1997). Protein at various concentrations (120–480 μ M) was injected onto a Superdex 200 10/300 GL size-exclusion chromatography column (GE Healthcare) equilibrated in buffer containing 20 mM Tris-HCl, pH 8.0, 100 mM NaCl, and 5 mM DTT. The chromatography system was connected in series with an 18-angle light scattering detector (DAWN HELEOS) and refractive index detector (OptilabrEX) (Wyatt Technology). Data were collected every 1 s at a flow rate of 0.25 ml/min at ambient temperature. Data analysis was carried out using the program ASTRA, yielding the molar mass and mass distribution (polydispersity) of the sample.

6. Protein Crystallization

Commercially available crystallization screens were used to find suitable crystallization conditions. Performing grid screens around the original crystallization conditions and variation of temperature and protein concentration further optimized crystal growth. Optimized crystals of the Sec13•Nup145C•Nup84 NTD complex (5 – 20 mg/mL) were grown at 20.5 °C in hanging drops containing 1 μ L protein and 1 μ L reservoir solution consisting of 100 mM MES, pH 5.6, 1.5–3.5 % wt/vol PEG 20 000, and 1–6 % vol/vol methanol or glycerol. Crystals were cryo-protected by stepwise transfer in 100mM MES, pH 5.6, 5.3 % PEG 20 000, 1–6 % (vol/vol) methanol, and 23 %

(vol/vol) glycerol (increased in 5 % steps), and flash frozen in liquid nitrogen-cooled liquid propane.

Incorporation of heavy metal derivatives was achieved by soaking of crystals in saturated solutions of various heavy metal compounds for 30 min up to several days.

X-ray diffraction data were acquired at the Advanced Photon Source (APS), the Advanced Light Source (ALS) and the National Synchrotron Light Source (NSLS). X-ray intensities were processed using HKL2000 (Otwinowski and Minor, 1997) The CCP4 program package (The CCP4 suite: programs for protein crystallography, 1994) was used for subsequent calculations.

7. Structure Determination and Refinement

Initial phases were determined using a $[\text{Ta}_6\text{Br}_{12}]^{2+}$ cluster derivative and SAD measurements (Hoelz et al., 2003; Murakami et al., 2002; Stavropoulos et al., 2006). These phases were used to locate and validate the heavy atom sites of potassium osmate (K_2OsO_4)-derivatized and SeMet labeled protein crystals. Combined phasing using isomorphous K_2OsO_4 and seleno-L-methionine SAD and native datasets was carried out in SHARP (de La Fortelle and Bricogne, 1997), followed by density modification in DM (The CCP4 suite: programs for protein crystallography, 1994), with solvent flattening and histogram matching. These phases allowed definition of the non-crystallographic symmetry (NCS) operators and the generation of NCS averaged maps.

The Sec13•Nup145C hetero-dimer (PDB ID code 3BG1) (Hsia et al., 2007) was docked into the electron density and an initial model for Nup84 NTD was built using O (Jones et al., 1991). The structure was refined to 3.2 Å resolution in CNS (Brünger et al., 1998). NCS restraints were applied throughout the refinement. The stereochemical quality of the final model was assessed with PROCHECK (Laskowski et al., 1993) and MOLPROBITY (Davis et al., 2007). Building and refinement of the model was done with help of Drs. Erik Debler and Kuo-Chiang Hsia.

Figures of the crystal structure were generated using PyMOL (DeLano, 2002) and Chimera (Pettersen et al., 2004; Sanner et al., 1996). The molecular surfaces were calculated using MSMS (Sanner et al., 1996), and the electrostatic potential was calculated using APBS (Baker et al., 2001).

8. Docking of Crystal Structures into the EM Structure

Docking of the crystal structures was performed by Dr. Martin Kampmann. Nucleoporin crystal structures were docked into a negative-stain EM reconstruction envelope of the *S. cerevisiae* Nup84 complex (Kampmann and Blobel, 2009) using algorithms from the Situs (Chacon and Wriggers, 2002) and Chimera (Pettersen et al., 2004) packages. The following crystal structures were used for rigid-body docking: Nup85•Seh1 (PDB ID code 3F3F) (Debler et al., 2008), Nup133 N-terminal domain (PDB ID code 1XKS) (Berke et al., 2004), Nup107•Nup133 C-terminal domains (Nup107 is the human homolog of yeast Nup84) (PDB ID code 3CQC) (Boehmer et al., 2008), Nup120 (PDB ID code 3F7F) (Seo et al., 2009), and Sec13•Nup145C•Nup84 NTD (PDB ID code 3IKO).

Zusammenfassung

In eukaryotischen Zellen ist der Zellkern durch die Kernhülle vom Cytoplasma getrennt. Jeglicher molekularer Austausch zwischen beiden Kompartimenten wird deshalb selektiv von Kernporenkomplexen (NPCs) vermittelt. NPCs sind Proteinkomplexe, die in Perforationen der Kernhülle eingebettet sind. Ein NPC wird von 30 verschiedenen Proteinen aufgebaut, wobei jedes einzelne Protein in mehreren Kopien vorliegt. Zusammen ergibt sich ein Molekulargewicht von circa 60 MDa pro NPC in Hefezellen. Die Zusammensetzung des NPCs wurde bereits gut charakterisiert, allerdings sind die genaue Anordnung der Proteine im NPC sowie die molekularen Mechanismen des Transportvorganges noch immer ungeklärt.

Kristallstrukturen einzelner Proteine und kleinerer Proteinkomplexe des NPCs haben wertvolle Informationen über die Bauweise und dynamische Beschaffenheit des NPCs geliefert. Bisher am besten charakterisiert wurde die Struktur des heptameren Nup84 Komplexes, eines essentiellen Bausteins des NPCs, mittels Röntgenstrukturanalysen und elektronenmikroskopischer (EM) Studien. Um unseren derzeitigen Wissensstand bezüglich des Aufbaus des NPCs zu erweitern, wurde die Kristallstruktur des trimeren Sec13•Nup145C•Nup84 NTD Komplexes bestimmt. Dieser stellt das Kernstück des Nup84 Komplexes dar. Die drei Proteine sind Z-förmig angeordnet, wobei Nup84 und das Sec13•Nup145C Proteinpaar Kopf an Kopf aneinander binden. Diese Kristallstruktur konnte, ebenso wie die Strukturen weiterer Proteine des Nup84 Komplexes, in eine EM-Struktur gedockt werden. Dadurch entstand ein nahezu vollständiges atomares Bild vom gesamten Nup84 Komplex. Eine vergleichende Analyse mit einer zuvor bestimmten Struktur von hSec13•Nup145C lässt auf ein promiskuitives Bindevverhalten von Nup145C schließen. Auch die biochemische und biophysikalische Untersuchung des Sec13•Nup145C•Nup84 NTD Komplexes deutet darauf hin, dass diese Proteine in verschiedenen Bindungszuständen vorliegen können. Es ist von großer Bedeutung, diese Bindungszustände in der Zukunft mittels interdisziplinärer Studien in den zellulären Zusammenhang einzuordnen.

List of Abbreviations

| | |
|----------------|--|
| Å | Angstroem |
| ACE1 | Ancestral Coatomer Element 1 |
| ALS | Advanced Light Source |
| APS | Advanced Photon Source |
| AUC | Analytical ultracentrifugation |
| COP | Coat protein complex |
| CTD | C-terminal domain |
| DIM | Domain invasion motif |
| DNA | Deoxyribonucleic acid |
| DTT | Dithiothreitol |
| EM | Electron microscopy |
| ER | Endoplasmic reticulum |
| FG | Phenylalanine-glycine |
| g | Relative centrifugal force |
| GDP | Guanosine-5'-diphosphate |
| GEF | Guanine nucleotide exchange factor |
| GTP | Guanosine-5'-triphosphate |
| h | Human |
| INM | Inner nuclear membrane |
| IPTG | Isopropyl β -D-1-thiogalactopyranoside |
| Kap | Karyopherin |
| kcal | Kilocalorie |
| K _d | Dissociation constant |
| kDa | Kilodalton |
| LB | Luria Bertani |
| MALS | Multi-angle light scattering |
| MDa | Megadalton |
| MES | 2-(N-morpholino)ethanesulfonic acid |
| MIRAS | Multiple isomorphous replacement with anomalous signal |

List of Abbreviation

| | |
|----------------------|---|
| mM | Milimolar |
| mRNA | Messenger ribonucleic acid |
| mRNP | Messenger ribonucleoprotein particles |
| NCS | Non-crystallographic symmetry |
| NEBD | Nuclear envelope breakdown |
| NES | Nuclear export sequence |
| Ni-NTA | Nickel-nitrilotriacetic acid |
| NLS | Nuclear localization sequence |
| nM | Nanomolar |
| nm | Nanometer |
| NPC | Nuclear pore complex |
| NSLS | National Synchrotron Light Source |
| NTD | N-terminal domain |
| Nup | Nucleoporin |
| OMN | Outer nuclear membrane |
| PDB | Protein Database |
| PEG | Polyethylene glycol |
| PMSF | Phenylmethanesulfonyl fluoride |
| POM | Pore membrane domain |
| rmsd | Root mean square deviation |
| RNA | Ribonucleic acid |
| S | Svedberg |
| <i>S. cerevisiae</i> | <i>Saccharomyces cerevisiae</i> |
| SAD | Single anomalous dispersion |
| SDS-PAGE | Sodium dodecyl sulfate polyacrylamide gel electrophoresis |
| SEC | Size exclusion chromatography |
| TCEP | Tris(2-carboxyethyl)phosphine |
| Tris | Tris(hydroxymethyl)aminomethane |
| UV | Ultraviolet |
| w/v | Weight per volume |
| ΔH | Enthalpy |

List of Abbreviation

ΔTS

Entropy

μM

Micromolar

List of Figures

| | |
|---|----|
| Figure 1: Nuclei with Nuclear Pore Complexes | 11 |
| Figure 2: Transport functions of the NPC | 13 |
| Figure 3: Schematic model and composition of the yeast NPC | 17 |
| Figure 4: A structural model for the Nup84 complex | 23 |
| Figure 5: Three-dimensional EM-reconstruction of the Nup84 complex | 24 |
| Figure 6: Crystal structure of the hSec13•Nup145C complex | 27 |
| Figure 7: Model for the coating cylinder of the NPC | 28 |
| Figure 8: Crystal structure of the Seh1•Nup85 complex | 29 |
| Figure 9: Refined model for the coating cylinder of the NPC | 30 |
| Figure 10: Structure of the outer shell of the COPII complex | 32 |
| Figure 11: Lattice model for the Nup84 complex | 33 |
| Figure 12: Computational model for the Nup84 complex within the NPC | 34 |
| Figure 13: Domain structures of Sec13, Nup145C, and Nup84. | 37 |
| Figure 14: Multispecies sequence alignment of Sec13 | 38 |
| Figure 15: Multispecies sequence alignment of Nup145C | 39 |
| Figure 16: Multispecies sequence alignment of Nup84 | 40 |
| Figure 17: Purification of Nup84 NTD part I | 43 |
| Figure 18: Purification of Nup84 NTD part II | 44 |
| Figure 19: Purification of the Sec13•Nup145C complex | 47 |
| Figure 20: Complex formation of Sec13•Nup145C•Nup84 NTD | 49 |
| Figure 21: Isothermal titration calorimetry analysis of the trimeric Sec13•Nup145C•Nup84 NTD complex | 50 |
| Figure 22: Crystals of Nup84 NTD | 52 |

List of Figures

| | |
|---|-----|
| Figure 23: Initial crystals of the Sec13•Nup145C•Nup84 NTD complex | 53 |
| Figure 24: Optimization of crystal growth | 54 |
| Figure 25: Diffraction pattern of native crystals | 55 |
| Figure 26: Anomalous difference Fourier maps | 59 |
| Figure 27: Experimental electron density map | 60 |
| Figure 28: The asymmetric unit of the Sec13•Nup145•Nup84 NTD crystals. | 61 |
| Figure 29: Ramachandran plot of the Sec13•Nup145C•Nup84 NTD structure | 63 |
| Figure 30: Structure of the <i>S. cerevisiae</i> Sec13•Nup145C•Nup84 NTD complex. | 64 |
| Figure 31: The Nup84 NTD α -helical domain | 65 |
| Figure 32: Similar topology of α -helical solenoids | 66 |
| Figure 33: Surface properties of Nup84 NTD. | 67 |
| Figure 34: Interaction of Nup84 NTD with Nup145C. | 69 |
| Figure 35: Protein arrangement within the heptameric Nup84 complex. | 71 |
| Figure 36: Structural comparison of Sec13•Nup145C•Nup84 NTD and hSec13•Nup145C. | 73 |
| Figure 37: Homo- and hetero-dimerization of Nup145C | 75 |
| Figure 38: Structural comparison of Nup145C•Nup145C homo-dimers and Nup145•Nup84 hetero-dimers. | 77 |
| Figure 39: Dynamic behavior of Sec13•Nup145C•Nup84 NTD and Nup84 NTD in solution | 79 |
| Figure 40: Structural investigation of the Nup84 complex | 86 |
| Figure 41: Flexible modules within the NPC | 88 |
| Figure 42: Flow chart of the protein purification procedure | 103 |

List of Tables

| | | |
|----------|---|----|
| Table 1: | Data collection and refinement statistics | 57 |
| Table 2: | Biophysical analysis of the oligomerization | 80 |

Bibliography

Akey, C.W. (1990). Visualization of transport-related configurations of the nuclear pore transporter. *Biophys J* 58, 341-355.

Akey, C.W. (1995). Structural plasticity of the nuclear pore complex. *J Mol Biol* 248, 273-293.

Akey, C.W., and Radermacher, M. (1993). Architecture of the *Xenopus* nuclear pore complex revealed by three-dimensional cryo-electron microscopy. *J Cell Biol* 122, 1-19.

Alber, F., Dokudovskaya, S., Veenhoff, L.M., Zhang, W., Kipper, J., Devos, D., Suprapto, A., Karni-Schmidt, O., Williams, R., Chait, B.T., *et al.* (2007a). Determining the architectures of macromolecular assemblies. *Nature* 450, 683-694.

Alber, F., Dokudovskaya, S., Veenhoff, L.M., Zhang, W., Kipper, J., Devos, D., Suprapto, A., Karni-Schmidt, O., Williams, R., Chait, B.T., *et al.* (2007b). The molecular architecture of the nuclear pore complex. *Nature* 450, 695-701.

Allen, N.P., Huang, L., Burlingame, A., and Rexach, M. (2001). Proteomic analysis of nucleoporin interacting proteins. *J Biol Chem* 276, 29268-29274.

Bailer, S.M., Balduf, C., and Hurt, E. (2001). The Nsp1p carboxy-terminal domain is organized into functionally distinct coiled-coil regions required for assembly of nucleoporin subcomplexes and nucleocytoplasmic transport. *Mol Cell Biol* 21, 7944-7955.

Baker, N.A., Sept, D., Joseph, S., Holst, M.J., and McCammon, J.A. (2001). Electrostatics of nanosystems: application to microtubules and the ribosome. *Proc Natl Acad Sci U S A* 98, 10037-10041.

Barton, G.J. (1993). ALSCRIPT: a tool to format multiple sequence alignments. *Protein Eng* 6, 37-40.

Bibliography

Beck, M., Forster, F., Ecke, M., Plitzko, J.M., Melchior, F., Gerisch, G., Baumeister, W., and Medalia, O. (2004). Nuclear pore complex structure and dynamics revealed by cryoelectron tomography. *Science* *306*, 1387-1390.

Beck, M., Lucic, V., Forster, F., Baumeister, W., and Medalia, O. (2007). Snapshots of nuclear pore complexes in action captured by cryo-electron tomography. *Nature* *449*, 611-615.

Belgareh, N., Rabut, G., Bai, S.W., van Overbeek, M., Beaudouin, J., Daigle, N., Zatssepina, O.V., Pasteau, F., Labas, V., Fromont-Racine, M., *et al.* (2001). An evolutionarily conserved NPC subcomplex, which redistributes in part to kinetochores in mammalian cells. *J Cell Biol* *154*, 1147-1160.

Berke, I.C., Boehmer, T., Blobel, G., and Schwartz, T.U. (2004). Structural and functional analysis of Nup133 domains reveals modular building blocks of the nuclear pore complex. *J Cell Biol* *167*, 591-597.

Blobel, G. (1980). Intracellular protein topogenesis. *Proc Natl Acad Sci U S A* *77*, 1496-1500.

Blobel, G. (1985). Gene gating: a hypothesis. *Proc Natl Acad Sci U S A* *82*, 8527-8529.

Bodoor, K., Shaikh, S., Enarson, P., Chowdhury, S., Salina, D., Raharjo, W.H., and Burke, B. (1999). Function and assembly of nuclear pore complex proteins. *Biochem Cell Biol* *77*, 321-329.

Boehmer, T., Enninga, J., Dales, S., Blobel, G., and Zhong, H. (2003). Depletion of a single nucleoporin, Nup107, prevents the assembly of a subset of nucleoporins into the nuclear pore complex. *Proc Natl Acad Sci U S A* *100*, 981-985.

Boehmer, T., Jeudy, S., Berke, I.C., and Schwartz, T.U. (2008). Structural and functional studies of Nup107/Nup133 interaction and its implications for the architecture of the nuclear pore complex. *Mol Cell* *30*, 721-731.

- Brohawn, S.G., Leksa, N.C., Spear, E.D., Rajashankar, K.R., and Schwartz, T.U. (2008). Structural evidence for common ancestry of the nuclear pore complex and vesicle coats. *Science* 322, 1369-1373.
- Brünger, A.T., Adams, P.D., Clore, G.M., DeLano, W.L., Gros, P., Grosse-Kunstleve, R.W., Jiang, J.S., Kuszewski, J., Nilges, M., Pannu, N.S., *et al.* (1998). Crystallography & NMR system: A new software suite for macromolecular structure determination. *Acta Crystallogr D Biol Crystallogr* 54, 905-921.
- Burke, B., and Stewart, C.L. (2006). The laminopathies: the functional architecture of the nucleus and its contribution to disease. *Annu Rev Genomics Hum Genet* 7, 369-405.
- Chacon, P., and Wriggers, W. (2002). Multi-resolution contour-based fitting of macromolecular structures. *J Mol Biol* 317, 375-384.
- Chial, H.J., Rout, M.P., Giddings, T.H., and Winey, M. (1998). *Saccharomyces cerevisiae* Ndc1p is a shared component of nuclear pore complexes and spindle pole bodies. *J Cell Biol* 143, 1789-1800.
- Chook, Y.M., and Blobel, G. (2001). Karyopherins and nuclear import. *Curr Opin Struct Biol* 11, 703-715.
- Combet, C., Blanchet, C., Geourjon, C., and Deleage, G. (2000). NPS@: network protein sequence analysis. *Trends Biochem Sci* 25, 147-150.
- Cook, A., Bono, F., Jinek, M., and Conti, E. (2007). Structural biology of nucleocytoplasmic transport. *Annu Rev Biochem* 76, 647-671.
- Davis, I.W., Leaver-Fay, A., Chen, V.B., Block, J.N., Kapral, G.J., Wang, X., Murray, L.W., Arendall, W.B., 3rd, Snoeyink, J., Richardson, J.S., *et al.* (2007). MolProbity: all-atom contacts and structure validation for proteins and nucleic acids. *Nucleic Acids Res* 35, W375-383.

de La Fortelle, E., and Bricogne, G. (1997). Maximum-Likelihood Heavy-Atom Parameter Refinement for Multiple Isomorphous Replacement and Multiwavelength Anomalous Diffraction Methods. In *Methods in Enzymology*, J.N. Abelson, M.I. Simon, J. Carter, C.W. , and R.M. Sweet, eds. (Academic Press), pp. 307-326.

Debler, E.W., Ma, Y., Seo, H.S., Hsia, K.C., Noriega, T.R., Blobel, G., and Hoelz, A. (2008). A fence-like coat for the nuclear pore membrane. *Mol Cell* 32, 815-826.

DeLano, W.L. (2002). The PyMOL Molecular Graphics System. <http://www.pymol.org>.

Devos, D., Dokudovskaya, S., Alber, F., Williams, R., Chait, B.T., Sali, A., and Rout, M.P. (2004). Components of coated vesicles and nuclear pore complexes share a common molecular architecture. *PLoS Biol* 2, e380.

Doublet, S. (1997). Preparation of selenomethionyl proteins for phase determination. *Methods Enzymol* 276, 523-530.

Drin, G., Casella, J.F., Gautier, R., Boehmer, T., Schwartz, T.U., and Antonny, B. (2007). A general amphipathic alpha-helical motif for sensing membrane curvature. *Nat Struct Mol Biol* 14, 138-146.

Fahrenkrog, B., Hurt, E.C., Aebi, U., and Pante, N. (1998). Molecular architecture of the yeast nuclear pore complex: localization of Nsp1p subcomplexes. *J Cell Biol* 143, 577-588.

Fath, S., Mancias, J.D., Bi, X., and Goldberg, J. (2007). Structure and organization of coat proteins in the COPII cage. *Cell* 129, 1325-1336.

Feldherr, C.M. (1962). The nuclear annuli as pathways for nucleocytoplasmic exchanges. *J Cell Biol* 14, 65-72.

Bibliography

- Floer, M., and Blobel, G. (1996). The nuclear transport factor karyopherin beta binds stoichiometrically to Ran-GTP and inhibits the Ran GTPase activating protein. *J Biol Chem* 271, 5313-5316.
- Frey, S., and Gorlich, D. (2007). A saturated FG-repeat hydrogel can reproduce the permeability properties of nuclear pore complexes. *Cell* 130, 512-523.
- Gall, J.G. (1967). Octagonal nuclear pores. *J Cell Biol* 32, 391-399.
- Galy, V., Olivo-Marin, J.C., Scherthan, H., Doye, V., Rascalou, N., and Nehrbass, U. (2000). Nuclear pore complexes in the organization of silent telomeric chromatin. *Nature* 403, 108-112.
- Handa, N., Kukimoto-Niino, M., Akasaka, R., Kishishita, S., Murayama, K., Terada, T., Inoue, M., Kigawa, T., Kose, S., Imamoto, N., *et al.* (2006). The crystal structure of mouse Nup35 reveals atypical RNP motifs and novel homodimerization of the RRM domain. *J Mol Biol* 363, 114-124.
- Harel, A., Orjalo, A.V., Vincent, T., Lachish-Zalait, A., Vasu, S., Shah, S., Zimmerman, E., Elbaum, M., and Forbes, D.J. (2003). Removal of a single pore subcomplex results in vertebrate nuclei devoid of nuclear pores. *Mol Cell* 11, 853-864.
- Hinshaw, J.E., Carragher, B.O., and Milligan, R.A. (1992). Architecture and design of the nuclear pore complex. *Cell* 69, 1133-1141.
- Hinshaw, J.E., and Milligan, R.A. (2003). Nuclear pore complexes exceeding eightfold rotational symmetry. *J Struct Biol* 141, 259-268.
- Hodel, A.E., Hodel, M.R., Griffis, E.R., Hennig, K.A., Ratner, G.A., Xu, S., and Powers, M.A. (2002). The three-dimensional structure of the autoproteolytic, nuclear pore-targeting domain of the human nucleoporin Nup98. *Mol Cell* 10, 347-358.

Bibliography

- Hoelz, A., Nairn, A.C., and Kuriyan, J. (2003). Crystal structure of a tetradecameric assembly of the association domain of Ca²⁺/calmodulin-dependent kinase II. *Mol Cell* *11*, 1241-1251.
- Hsia, K.C., Stavropoulos, P., Blobel, G., and Hoelz, A. (2007). Architecture of a coat for the nuclear pore membrane. *Cell* *131*, 1313-1326.
- Hurwitz, M.E., Strambio-de-Castillia, C., and Blobel, G. (1998). Two yeast nuclear pore complex proteins involved in mRNA export form a cytoplasmically oriented subcomplex. *Proc Natl Acad Sci U S A* *95*, 11241-11245.
- Jarnik, M., and Aebi, U. (1991). Toward a more complete 3-D structure of the nuclear pore complex. *J Struct Biol* *107*, 291-308.
- Jeanmougin, F., Thompson, J.D., Gouy, M., Higgins, D.G., and Gibson, T.J. (1998). Multiple sequence alignment with Clustal X. *Trends Biochem Sci* *23*, 403-405.
- Jeady, S., and Schwartz, T.U. (2007). Crystal structure of nucleoporin Nic96 reveals a novel, intricate helical domain architecture. *J Biol Chem* *282*, 34904-34912.
- Jones, T.A., Zou, J.Y., Cowan, S.W., and Kjeldgaard, M. (1991). Improved methods for building protein models in electron density maps and the location of errors in these models. *Acta Crystallogr A* *47 (Pt 2)*, 110-119.
- Kaiser, C.A., and Schekman, R. (1990). Distinct sets of SEC genes govern transport vesicle formation and fusion early in the secretory pathway. *Cell* *61*, 723-733.
- Kampmann, M., and Blobel, G. (2009). Three-dimensional structure and flexibility of a membrane-coating module of the nuclear pore complex. *Nat Struct Mol Biol* *16*, 782-788.

Bibliography

Kantardjieff, K.A., and Rupp, B. (2003). Matthews coefficient probabilities: Improved estimates for unit cell contents of proteins, DNA, and protein-nucleic acid complex crystals. *Protein Sci* 12, 1865-1871.

Kendrew, J.C., Dickerson, R.E., Strandberg, B.E., Hart, R.G., Davies, D.R., Phillips, D.C., and Shore, V.C. (1960). Structure of myoglobin: A three-dimensional Fourier synthesis at 2 Å resolution. *Nature* 185, 422-427.

Khadaroo, B., Teixeira, M.T., Luciano, P., Eckert-Boulet, N., Germann, S.M., Simon, M.N., Gallina, I., Abdallah, P., Gilson, E., Geli, V., *et al.* (2009). The DNA damage response at eroded telomeres and tethering to the nuclear pore complex. *Nat Cell Biol* 11, 980-987.

King, M.C., Lusk, C.P., and Blobel, G. (2006). Karyopherin-mediated import of integral inner nuclear membrane proteins. *Nature* 442, 1003-1007.

Kirchhausen, T. (2000). Three ways to make a vesicle. *Nat Rev Mol Cell Biol* 1, 187-198.

Kiseleva, E., Allen, T.D., Rutherford, S., Bucci, M., Wentz, S.R., and Goldberg, M.W. (2004). Yeast nuclear pore complexes have a cytoplasmic ring and internal filaments. *J Struct Biol* 145, 272-288.

Kiseleva, E., Goldberg, M.W., Allen, T.D., and Akey, C.W. (1998). Active nuclear pore complexes in *Chironomus*: visualization of transporter configurations related to mRNP export. *J Cell Sci* 111 (Pt 2), 223-236.

Knäblein, J., Neufeind, T., Schneider, F., Bergner, A., Messerschmidt, A., Lowe, J., Steipe, B., and Huber, R. (1997). Ta6Br(2+)₁₂, a tool for phase determination of large biological assemblies by X-ray crystallography. *J Mol Biol* 270, 1-7.

Kraemer, D.M., Strambio-de-Castillia, C., Blobel, G., and Rout, M.P. (1995). The essential yeast nucleoporin NUP159 is located on the cytoplasmic side of the nuclear pore complex and serves in karyopherin-mediated binding of transport substrate. *J Biol Chem* 270, 19017-19021.

Bibliography

Laskowski, R.A., MacArthur, M.W., Moss, D.S., and Thornton, J.M. (1993). PROCHECK: a program to check the stereochemical quality of protein structures. *Journal of Applied Crystallography* 26, 283-291.

Leksa, N.C., Brohawn, S.G., and Schwartz, T.U. (2009). The structure of the scaffold nucleoporin Nup120 reveals a new and unexpected domain architecture. *Structure* 17, 1082-1091.

Liodice, I., Alves, A., Rabut, G., Van Overbeek, M., Ellenberg, J., Sibarita, J.B., and Doye, V. (2004). The entire Nup107-160 complex, including three new members, is targeted as one entity to kinetochores in mitosis. *Mol Biol Cell* 15, 3333-3344.

Lutzmann, M., Kunze, R., Buerer, A., Aebi, U., and Hurt, E. (2002). Modular self-assembly of a Y-shaped multiprotein complex from seven nucleoporins. *EMBO J* 21, 387-397.

Matthews, B.W. (1968). Solvent content of protein crystals. *J Mol Biol* 33, 491-497.

Melčák, I., Hoelz, A., and Blobel, G. (2007). Structure of Nup58/45 suggests flexible nuclear pore diameter by intermolecular sliding. *Science* 315, 1729-1732.

Moroianu, J., Blobel, G., and Radu, A. (1996). Nuclear protein import: Ran-GTP dissociates the karyopherin alphabeta heterodimer by displacing alpha from an overlapping binding site on beta. *Proc Natl Acad Sci U S A* 93, 7059-7062.

Murakami, K.S., Masuda, S., and Darst, S.A. (2002). Structural basis of transcription initiation: RNA polymerase holoenzyme at 4 Å resolution. *Science* 296, 1280-1284.

Murray, S., and Kiseleva, E. (2008). A protocol for isolation and visualization of yeast nuclei by scanning electron microscopy. *Methods Cell Biol* 88, 367-387.

Bibliography

Nagai, S., Dubrana, K., Tsai-Pflugfelder, M., Davidson, M.B., Roberts, T.M., Brown, G.W., Varela, E., Hediger, F., Gasser, S.M., and Krogan, N.J. (2008). Functional targeting of DNA damage to a nuclear pore-associated SUMO-dependent ubiquitin ligase. *Science* 322, 597-602.

Napetschnig, J., Blobel, G., and Hoelz, A. (2007). Crystal structure of the N-terminal domain of the human protooncogene Nup214/CAN. *Proc Natl Acad Sci U S A* 104, 1783-1788.

Napetschnig, J., Kassube, S.A., Debler, E.W., Wong, R.W., Blobel, G., and Hoelz, A. (2009). Structural and functional analysis of the interaction between the nucleoporin Nup214 and the DEAD-box helicase Ddx19. *Proc Natl Acad Sci U S A* 106, 3089-3094.

Nehrbass, U., and Blobel, G. (1996). Role of the nuclear transport factor p10 in nuclear import. *Science* 272, 120-122.

Otwinowski, Z., and Minor, W. (1997). Processing of X-ray Diffraction Data Collected in Oscillation Mode. In *Methods in Enzymology*, J.N. Abelson, M.I. Simon, J. Carter, C.W. , and R.M. Sweet, eds. (Academic Press), pp. 307-326.

Paine, P.L., Moore, L.C., and Horowitz, S.B. (1975). Nuclear envelope permeability. *Nature* 254, 109-114.

Pante, N., and Kann, M. (2002). Nuclear pore complex is able to transport macromolecules with diameters of about 39 nm. *Mol Biol Cell* 13, 425-434.

Partridge, J.R., and Schwartz, T.U. (2009). Crystallographic and biochemical analysis of the Ran-binding zinc finger domain. *J Mol Biol* 391, 375-389.

Patel, S.S., Belmont, B.J., Sante, J.M., and Rexach, M.F. (2007). Natively unfolded nucleoporins gate protein diffusion across the nuclear pore complex. *Cell* 129, 83-96.

PDB Protein Data Bank. <http://www.pdb.org>.

Bibliography

- Peters, R. (1984). Nucleo-cytoplasmic flux and intracellular mobility in single hepatocytes measured by fluorescence microphotolysis. *EMBO J* 3, 1831-1836.
- Pettersen, E.F., Goddard, T.D., Huang, C.C., Couch, G.S., Greenblatt, D.M., Meng, E.C., and Ferrin, T.E. (2004). UCSF Chimera--a visualization system for exploratory research and analysis. *J Comput Chem* 25, 1605-1612.
- Philo, J. <http://www.jphilo.mailway.com/>.
- Reverter, D., and Lima, C.D. (2005). Insights into E3 ligase activity revealed by a SUMO-RanGAP1-Ubc9-Nup358 complex. *Nature* 435, 687-692.
- Ribbeck, K., and Gorlich, D. (2002). The permeability barrier of nuclear pore complexes appears to operate via hydrophobic exclusion. *EMBO J* 21, 2664-2671.
- Ribbeck, K., Lipowsky, G., Kent, H.M., Stewart, M., and Gorlich, D. (1998). NTF2 mediates nuclear import of Ran. *EMBO J* 17, 6587-6598.
- Rout, M.P., Aitchison, J.D., Magnasco, M.O., and Chait, B.T. (2003). Virtual gating and nuclear transport: the hole picture. *Trends Cell Biol* 13, 622-628.
- Rout, M.P., Aitchison, J.D., Suprapto, A., Hjertaas, K., Zhao, Y., and Chait, B.T. (2000). The yeast nuclear pore complex: composition, architecture, and transport mechanism. *J Cell Biol* 148, 635-651.
- Sagan, L. (1967). On the origin of mitosing cells. *J Theor Biol* 14, 255-274.
- Salama, N.R., Yeung, T., and Schekman, R.W. (1993). The Sec13p complex and reconstitution of vesicle budding from the ER with purified cytosolic proteins. *EMBO J* 12, 4073-4082.
- Sanner, M.F., Olson, A.J., and Spehner, J.C. (1996). Reduced surface: an efficient way to compute molecular surfaces. *Biopolymers* 38, 305-320.

Bibliography

- Saxena, K., Gaitatzes, C., Walsh, M.T., Eck, M., Neer, E.J., and Smith, T.F. (1996). Analysis of the physical properties and molecular modeling of Sec13: A WD repeat protein involved in vesicular traffic. *Biochemistry* 35, 15215-15221.
- Schrader, N., Koerner, C., Koessmeier, K., Bangert, J.A., Wittinghofer, A., Stoll, R., and Vetter, I.R. (2008a). The crystal structure of the Ran-Nup153ZnF2 complex: a general Ran docking site at the nuclear pore complex. *Structure* 16, 1116-1125.
- Schrader, N., Stelzer, P., Flemming, D., Kunze, R., Hurt, E., and Vetter, I.R. (2008b). Structural basis of the nic96 subcomplex organization in the nuclear pore channel. *Mol Cell* 29, 46-55.
- Schuck, P. (2000). Size-distribution analysis of macromolecules by sedimentation velocity ultracentrifugation and lamm equation modeling. *Biophys J* 78, 1606-1619.
- Seo, H.S., Ma, Y., Debler, E.W., Wacker, D., Kutik, S., Blobel, G., and Hoelz, A. (2009). Structural and functional analysis of Nup120 suggests ring formation of the Nup84 complex. *Proc Natl Acad Sci U S A* 106, 14281-14286.
- Siniosoglou, S., Lutzmann, M., Santos-Rosa, H., Leonard, K., Mueller, S., Aebi, U., and Hurt, E. (2000). Structure and assembly of the Nup84p complex. *J Cell Biol* 149, 41-54.
- Siniosoglou, S., Wimmer, C., Rieger, M., Doye, V., Tekotte, H., Weise, C., Emig, S., Segref, A., and Hurt, E.C. (1996). A novel complex of nucleoporins, which includes Sec13p and a Sec13p homolog, is essential for normal nuclear pores. *Cell* 84, 265-275.
- Stagg, S.M., Gurkan, C., Fowler, D.M., LaPointe, P., Foss, T.R., Potter, C.S., Carragher, B., and Balch, W.E. (2006). Structure of the Sec13/31 COPII coat cage. *Nature* 439, 234-238.

Bibliography

Stagg, S.M., LaPointe, P., and Balch, W.E. (2007). Structural design of cage and coat scaffolds that direct membrane traffic. *Curr Opin Struct Biol* *17*, 221-228.

Stagg, S.M., LaPointe, P., Razvi, A., Gurkan, C., Potter, C.S., Carragher, B., and Balch, W.E. (2008). Structural basis for cargo regulation of COPII coat assembly. *Cell* *134*, 474-484.

Stavropoulos, P., Blobel, G., and Hoelz, A. (2006). Crystal structure and mechanism of human lysine-specific demethylase-1. *Nat Struct Mol Biol* *13*, 626-632.

Sun, Y., and Guo, H.C. (2008). Structural constraints on autoprocessing of the human nucleoporin Nup98. *Protein Sci* *17*, 494-505.

Teixeira, M.T., Siniosoglou, S., Podtelejnikov, S., Benichou, J.C., Mann, M., Dujon, B., Hurt, E., and Fabre, E. (1997). Two functionally distinct domains generated by in vivo cleavage of Nup145p: a novel biogenesis pathway for nucleoporins. *EMBO J* *16*, 5086-5097.

The CCP4 suite: programs for protein crystallography. (1994). *Acta Crystallogr D Biol Crystallogr* *50*, 760-763.

Towbin, B.D., Meister, P., and Gasser, S.M. (2009). The nuclear envelope--a scaffold for silencing? *Curr Opin Genet Dev* *19*, 180-186.

Vasu, S., Shah, S., Orjalo, A., Park, M., Fischer, W.H., and Forbes, D.J. (2001). Novel vertebrate nucleoporins Nup133 and Nup160 play a role in mRNA export. *J Cell Biol* *155*, 339-354.

Vasu, S.K., and Forbes, D.J. (2001). Nuclear pores and nuclear assembly. *Curr Opin Cell Biol* *13*, 363-375.

Vetter, I.R., Nowak, C., Nishimoto, T., Kuhlmann, J., and Wittinghofer, A. (1999). Structure of a Ran-binding domain complexed with Ran bound to a GTP analogue: implications for nuclear transport. *Nature* *398*, 39-46.

Bibliography

Vlcek, S., and Foisner, R. (2007). Lamins and lamin-associated proteins in aging and disease. *Curr Opin Cell Biol* 19, 298-304.

von Moeller, H., Basquin, C., and Conti, E. (2009). The mRNA export protein DBP5 binds RNA and the cytoplasmic nucleoporin NUP214 in a mutually exclusive manner. *Nat Struct Mol Biol* 16, 247-254.

Watson, M.L. (1954). Pores in the mammalian nuclear membrane. *Biochim Biophys Acta* 15, 475-479.

Weirich, C.S., Erzberger, J.P., Berger, J.M., and Weis, K. (2004). The N-terminal domain of Nup159 forms a beta-propeller that functions in mRNA export by tethering the helicase Dbp5 to the nuclear pore. *Mol Cell* 16, 749-760.

Whittle, J.R., and Schwartz, T.U. (2009). Architectural nucleoporins Nup157/170 and Nup133 are structurally related and descend from a second ancestral element. *J Biol Chem* 284, 28442-28452.

Wozniak, R.W., Blobel, G., and Rout, M.P. (1994). POM152 is an integral protein of the pore membrane domain of the yeast nuclear envelope. *J Cell Biol* 125, 31-42.

Wyatt, P.J. (1997). Multiangle Light Scattering: The Basic Tool for Macromolecular Characterization. *Instrumentation Science & Technology* 25, 1 - 18.

Yang, Q., Rout, M.P., and Akey, C.W. (1998). Three-dimensional architecture of the isolated yeast nuclear pore complex: functional and evolutionary implications. *Mol Cell* 1, 223-234.